

ANALYSIS OF TWO-PHASE FLOW THROUGH AN ELECTRIC SUBMERSIBLE
PUMP USING COMPUTATIONAL FLUID DYNAMICS

A Thesis

by

TANVI MILIND KATKE

Submitted to the Office of Graduate and Professional Studies of
Texas A&M University
in partial fulfillment of the requirements for the degree of

MASTER OF SCIENCE

Chair of Committee,	Adolfo Delgado-Marquez
Co-Chair of Committee,	Michael Pate
Committee Member,	Karen Vierow Kirkland
Head of Department,	Andreas A. Polycarpou

May 2020

Major Subject: Mechanical Engineering

Copyright 2020 Tanvi Milind Katke

ABSTRACT

Electrical submersible pumps (ESP) are widely used in the oil and gas industry as a method of artificial lift. They typically consist of multiple centrifugal pump stages that convert kinetic energy to hydraulic pressure head. ESPs frequently handle multi-phase flow including traces of gas which degrade their performance. Hence, it is essential to understand how two-phase flow affects the pump performance in order to design and size ESPs.

The purpose of this project is to study two-phase flow inside an ESP with air and water as the two fluids using ANSYS Fluent. The pump is simulated at two speeds, namely 3600 rpm and 6000 rpm for fixed bubble sizes at different gas flow rates. The parameters monitored are pressure head, water velocity and air volume fraction distribution inside the pump. They are compared with results from population balance model that simulates the breakup and coalescence of bubbles. At low air volume fractions and high turbulence, bubbles of large size are not likely to exist in a flow and a fixed bubble size simulation gives good results for such a case, as is also verified from previous experimental studies. The data from this project establishes a baseline for future analyses and improves the understanding of effects of bubble sizes for multi-phase flow through an ESP.

DEDICATION

To my parents

ACKNOWLEDGEMENTS

I would like to thank my committee chair, Dr. Delgado, for his diligent support, guidance and encouragement. I am thankful to my committee members, Dr. Pate and Dr. Kirkland, for their timely help. I am especially grateful to Dr. Abhay Patil for giving me this opportunity and for guiding me throughout the course of this research.

I also thank all the students and staff at the Turbomachinery Lab from whom I learnt a lot. Thanks also go to all my professors and staff at the department of Mechanical Engineering for making my time at Texas A&M University a splendid learning experience. I also appreciate the resources provided by the University Writing Center for completing my thesis.

I am immensely grateful to my parents, Milind and Smita, my brother, Tejas, grandmother, Mangala, sister-in-law, Mayuri, and nephew, Tanish, for their unwavering encouragement, love and enthusiasm throughout the course of my graduate education. Finally, thanks also go to all my friends, near and far.

Since this most likely marks the conclusion of my formal education, I extend my deepest gratitude to each and every teacher I have had at any time during the last two decades. This work is a culmination of everything that I have learnt from them, in some or the other way.

CONTRIBUTORS AND FUNDING SOURCES

Contributors

This work was supervised by a thesis committee consisting of Professor Adolfo Delgado-Marquez and Professor Michael Pate of the Department of Mechanical Engineering and Professor Karen Vierow Kirkland of the Department of Nuclear Engineering. Additional support was provided by Dr. Abhay Patil of the Texas A&M Turbomachinery Laboratory.

Part of the analyses used for comparison in Section 4 and the simulation model used in this analysis, were provided by Dr. Abhay Patil.

All other work conducted for the thesis was completed by the student independently.

Funding Sources

Graduate study was supported by fellowships and an assistantship from the Department of Mechanical Engineering.

NOMENCLATURE

A_i	Interfacial area
C_D	Drag coefficient
C_{w1}	-0.01 a non-dimensional coefficient
C_{w2}	0.05 a non-dimensional coefficient
C_{wl}	Wall lubrication coefficient
d_b	Bubble diameter
d_p	Diameter of bubbles of phase p
Eo	Eotvos number
f	Drag function
$\vec{F}_{lift,q}$	Lift force
$\vec{F}_{td,q}$	Turbulent dispersion force
$\vec{F}_{vm,q}$	Virtual mass force
$\vec{F}_{wl,q}$	Wall lubrication force
\vec{F}_q	External body force
\vec{g}	Acceleration due to gravity
G_b	Generation of turbulence kinetic energy due to buoyancy
G_k	Generation of turbulence kinetic energy due to mean velocity gradients
h_{pq}	Interphase enthalpy
h_q	Specific enthalpy of q phase
K_{pq}	Interphase momentum exchange coefficient
\dot{m}_{pq}	Mass transfer from p th phase to q th phase
\vec{n}_w	Unit normal pointing away from the wall

\vec{q}_q	Heat flux
PBM	Population balance model
p	Pressure shared by all phases
Q_{pq}	Intensity of heat exchange between p^{th} and q^{th} phases
Re	Relative Reynold's number
\vec{R}_{pq}	Interaction force between phases
S_k	User-defined source term
S_q	Source term
S_ε	User-defined source term
\vec{v}_{pq}	Interphase velocity
\vec{v}_q	Velocity of phase q
$ \vec{v}_q - \vec{v}_p $	Phase relative velocity component tangential to wall surface
V_q	Volume of phase q
y_w	Distance to the nearest wall
Y_M	Contribution of the fluctuating dilatation in compressible turbulence to the overall dissipation rate

Greek Symbols:

α_p	Volume fraction of secondary phase
α_q	Volume fraction of phase q
λ_q	Bulk viscosity of phase q
μ_q	Shear viscosity of phase q
μ_q	Viscosity of phase q
$\mu_{t,m}$	Turbulent viscosity of mixture

Π_{k_m}	Source terms used to model the turbulent interaction between dispersed and continuous phase
ρ_q	Density of primary (continuous) phase
ρ_q	Physical density of phase q
σ	Surface tension coefficient
σ_k	Turbulent Prandtl number for k
σ_ε	Turbulent Prandtl number for ε
τ_p	Particulate relaxation time
$\overline{\overline{\tau}}_q$	Stress-strain tensor for q th phase
$\overline{\overline{\Omega}}_{ij}$	Mean rate-of-rotation tensor

TABLE OF CONTENTS

	Page
ABSTRACT	ii
DEDICATION	iii
ACKNOWLEDGEMENTS	iv
CONTRIBUTORS AND FUNDING SOURCES.....	v
NOMENCLATURE.....	vi
TABLE OF CONTENTS	ix
LIST OF FIGURES.....	xi
LIST OF TABLES	xix
1. INTRODUCTION.....	1
1.1. Pump head degradation due to two-phase flow	2
1.2. Bubble size and distribution in centrifugal pumps.....	3
1.3. CFD modelling of two-phase flow.....	7
1.4. Empirical and analytical models for predicting bubble size	8
2. ESP STAGE FLOW DOMAIN AND SIMULATION CASES	10
3. NUMERICAL MODEL.....	12
3.1. Conservation Equations.....	15
3.2. Phase Interactions.....	17
3.2.1. Interfacial area concentration	17
3.2.2. Fluid-fluid exchange coefficient	18
3.2.3. Wall lubrication force.....	18
3.3. Turbulence Modeling	19
3.4. Boundary conditions	20
3.5. Solution	21
4. RESULTS.....	22
4.1. Dimensionless pressure head	22
4.2. Effect of bubble size.....	26
4.3. Effect of rotational speed	30

4.4. Comparison with population balance model	33
5. RECOMMENDATIONS AND FUTURE WORK.....	39
6. CONCLUSIONS	40
REFERENCES	42
APPENDIX A PRESSURE HEAD DEGRADATION AS A FUNCTION OF GVF AND BUBBLE SIZE	45
APPENDIX B AIR VOLUME FRACTION DISTRIBUTION AT 3600 RPM.....	48
APPENDIX C AIR VOLUME FRACTION DISTRIBUTION AT 6000 RPM.....	58
APPENDIX D WATER VELOCITY DISTRIBUTION	66

LIST OF FIGURES

	Page
Figure 1 CAD model of electric submersible pump stage flow domain used for analysis	10
Figure 2 Meshed model of single stage of ESP	13
Figure 3 Side view of mesh on impeller vanes and hub as viewed from mass inlet end .	14
Figure 4 Side view of mesh on diffuser vanes and hub as viewed from pressure outlet end.....	15
Figure 5 Dimensionless pressure head with increasing GVF for pump running at 3600 rpm for three cases of bubble sizes - 63.5 μm (2.5 mils), 76.2 μm (3 mils) and 101.6 μm (4 mils).....	23
Figure 6 Dimensionless pressure head with increasing GVF for pump running at 6000 rpm with for three cases of bubble sizes - 63.5 μm (2.5 mils), 76.2 μm (3 mils) and 101.6 μm (4 mils).....	25
Figure 7 Iso-surface on impeller blades for GVF=60% for pump running at 3600 rpm with inlet GVF 35% and bubble sizes (a) 63.5 μm (2.5 mils) (b) 76.2 μm (3 mils) and (c) 101.6 μm (4 mils).....	26
Figure 8 Iso-surface on impeller blades for GVF=60% for pump running at 6000 rpm with inlet GVF 35% and bubble sizes (a) 63.5 μm (2.5 mils) (b) 76.2 μm (3 mils) and (c) 101.6 μm (4 mils).....	27
Figure 9 Air volume fraction along blade to blade surface for pump running at 3600 rpm with inlet GVF 35% and bubble sizes (a) 63.5 μm (2.5 mils) (b) 76.2 μm (3 mils) and (c) 101.6 μm (4 mils)	28
Figure 10 Air volume fraction along blade to blade surface for pump running at 6000 rpm with inlet GVF 35% and bubble sizes (a) 63.5 μm (2.5 mils) (b) 76.2 μm (3 mils) and (c) 101.6 μm (4 mils)	28
Figure 11 Water velocity along blade to blade surface for pump running at 3600 rpm with inlet GVF 35% and bubble sizes (a) 63.5 μm (2.5 mils) (b) 76.2 μm (3 mils) and (c) 101.6 μm (4 mils).....	29
Figure 12 Water velocity along blade to blade surface for pump running at 6000 rpm with inlet GVF 35% and bubble sizes (a) 63.5 μm (2.5 mils) (b) 76.2 μm (3 mils) and (c) 101.6 μm (4 mils).....	29

Figure 13 Pressure distribution along blade to blade surface for pump with inlet GVF 25% and bubble size 3 mils for running speeds (a) 3600 rpm and (b) 6000 rpm.....	30
Figure 14 Air volume fraction distribution along blade to blade surface for pump with inlet GVF 25% and bubble size 3 mils for running speeds (a) 3600 rpm and (b) 6000 rpm	31
Figure 15 Water velocity distribution along blade to blade surface for pump with inlet GVF 25% and bubble size 3 mils for running speeds (a) 3600 rpm and (b) 6000 rpm.....	32
Figure 16 Comparison of dimensionless pressure head for pump running at 3600 rpm and 13% GVF for constant bubble size models and population balance model	34
Figure 17 Air volume fraction distribution along blade to blade surface for pump running at 3600 rpm with inlet GVF 13% and (a) constant bubble size 3mils (b) constant bubble size 4 mils (c) population balance model.....	35
Figure 18 Air volume fraction distribution along impeller vanes for pump running at 3600 rpm with inlet GVF 13% and (a) constant bubble size 3mils (b) constant bubble size 4 mils (c) population balance model	35
Figure 19 Iso-surface on impeller blades for GVF=60% for pump running at 3600 rpm with inlet GVF 13% and (a) constant bubble size 3mils (b) constant bubble size 4 mils (c) population balance model.....	36
Figure 20 Water velocity distribution along impeller vanes for pump running at 3600 rpm with inlet GVF 13% and (a) constant bubble size 3mils (b) constant bubble size 4 mils (c) population balance model.....	37
Figure B1 Air volume fraction along blade to blade surface for pump running at 3600 rpm with inlet GVF 13% and bubble sizes (a) 63.5 μm (2.5 mils) (b) 76.2 μm (3 mils) and (c) 101.6 μm (4 mils)	49
Figure B2 Air volume fraction along blade to blade surface for pump running at 3600 rpm with inlet GVF 19% and bubble sizes (a) 63.5 μm (2.5 mils) (b) 76.2 μm (3 mils) and (c) 101.6 μm (4 mils)	49
Figure B3 Air volume fraction along blade to blade surface for pump running at 3600 rpm with inlet GVF 24% and bubble sizes (a) 63.5 μm (2.5 mils) (b) 76.2 μm (3 mils) and (c) 101.6 μm (4 mils)	50

Figure B4 Air volume fraction along blade to blade surface for pump running at 3600 rpm with inlet GVF 29% and bubble sizes (a) 63.5 μm (2.5 mils) (b) 76.2 μm (3 mils) and (c) 101.6 μm (4 mils)	50
Figure B5 Air volume fraction along blade to blade surface for pump running at 3600 rpm with inlet GVF 35% and bubble sizes (a) 63.5 μm (2.5 mils) (b) 76.2 μm (3 mils) and (c) 101.6 μm (4 mils)	51
Figure B6 Air volume fraction along blade to blade surface for pump running at 3600 rpm with inlet GVF 40% and bubble sizes (a) 63.5 μm (2.5 mils) (b) 76.2 μm (3 mils) and (c) 101.6 μm (4 mils)	51
Figure B7 Air volume fraction along impeller vanes for pump running at 3600 rpm with inlet GVF 13% and bubble sizes (a) 63.5 μm (2.5 mils) (b) 76.2 μm (3 mils) and (c) 101.6 μm (4 mils)	51
Figure B8 Air volume fraction along blade to blade surface for pump running at 3600 rpm with inlet GVF 19% and bubble sizes (a) 63.5 μm (2.5 mils) (b) 76.2 μm (3 mils) and (c) 101.6 μm (4 mils)	52
Figure B9 Air volume fraction along blade to blade surface for pump running at 3600 rpm with inlet GVF 24% and bubble sizes (a) 63.5 μm (2.5 mils) (b) 76.2 μm (3 mils) and (c) 101.6 μm (4 mils)	52
Figure B10 Air volume fraction along blade to blade surface for pump running at 3600 rpm with inlet GVF 29% and bubble sizes (a) 63.5 μm (2.5 mils) (b) 76.2 μm (3 mils) and (c) 101.6 μm (4 mils)	52
Figure B11 Air volume fraction along blade to blade surface for pump running at 3600 rpm with inlet GVF 35% and bubble sizes (a) 63.5 μm (2.5 mils) (b) 76.2 μm (3 mils) and (c) 101.6 μm (4 mils)	53
Figure B12 Air volume fraction along blade to blade surface for pump running at 3600 rpm with inlet GVF 40% and bubble sizes (a) 63.5 μm (2.5 mils) (b) 76.2 μm (3 mils) and (c) 101.6 μm (4 mils)	53
Figure B13 Iso-surface on impeller blades for GVF=60% for pump running at 3600 rpm with inlet GVF 13% and bubble sizes (a) 63.5 μm (2.5 mils) (b) 76.2 μm (3 mils) and (c) 101.6 μm (4 mils)	54
Figure B14 Iso-surface on impeller blades for GVF=60% for pump running at 3600 rpm with inlet GVF 19% and bubble sizes (a) 63.5 μm (2.5 mils) (b) 76.2 μm (3 mils) and (c) 101.6 μm (4 mils)	54

Figure B15 Iso-surface on impeller blades for GVF=60% for pump running at 3600 rpm with inlet GVF 24% and bubble sizes (a) 63.5 μm (2.5 mils) (b) 76.2 μm (3 mils) and (c) 101.6 μm (4 mils)	54
Figure B16 Iso-surface on impeller blades for GVF=60% for pump running at 3600 rpm with inlet GVF 29% and bubble sizes (a) 63.5 μm (2.5 mils) (b) 76.2 μm (3 mils) and (c) 101.6 μm (4 mils)	54
Figure B17 Iso-surface on impeller blades for GVF=60% for pump running at 3600 rpm with inlet GVF 35% and bubble sizes (a) 63.5 μm (2.5 mils) (b) 76.2 μm (3 mils) and (c) 101.6 μm (4 mils)	55
Figure B18 Iso-surface on impeller blades for GVF=60% for pump running at 3600 rpm with inlet GVF 40% and bubble sizes (a) 63.5 μm (2.5 mils) (b) 76.2 μm (3 mils) and (c) 101.6 μm (4 mils)	55
Figure B19 Air volume fraction along meridional surface for pump running at 3600 rpm with inlet GVF 13% and bubble sizes (a) 63.5 μm (2.5 mils) (b) 76.2 μm (3 mils) and (c) 101.6 μm (4 mils)	55
Figure B20 Air volume fraction along meridional surface for pump running at 3600 rpm with inlet GVF 19% and bubble sizes (a) 63.5 μm (2.5 mils) (b) 76.2 μm (3 mils) and (c) 101.6 μm (4 mils)	56
Figure B21 Air volume fraction along meridional surface for pump running at 3600 rpm with inlet GVF 24% and bubble sizes (a) 63.5 μm (2.5 mils) (b) 76.2 μm (3 mils) and (c) 101.6 μm (4 mils)	56
Figure B22 Air volume fraction along meridional surface for pump running at 3600 rpm with inlet GVF 29% and bubble sizes (a) 63.5 μm (2.5 mils) (b) 76.2 μm (3 mils) and (c) 101.6 μm (4 mils)	56
Figure B23 Air volume fraction along meridional surface for pump running at 3600 rpm with inlet GVF 35% and bubble sizes (a) 63.5 μm (2.5 mils) (b) 76.2 μm (3 mils) and (c) 101.6 μm (4 mils)	57
Figure B24 Air volume fraction along meridional surface for pump running at 3600 rpm with inlet GVF 40% and bubble sizes (a) 63.5 μm (2.5 mils) (b) 76.2 μm (3 mils) and (c) 101.6 μm (4 mils)	57
Figure C1 Air volume fraction along blade to blade surface for pump running at 6000 rpm with inlet GVF 13% and bubble sizes (a) 63.5 μm (2.5 mils) (b) 76.2 μm (3 mils) and (c) 101.6 μm (4 mils)	59

Figure C2 Air volume fraction along blade to blade surface for pump running at 6000 rpm with inlet GVF 18% and bubble sizes (a) 63.5 μm (2.5 mils) (b) 76.2 μm (3 mils) and (c) 101.6 μm (4 mils)	59
Figure C3 Air volume fraction along blade to blade surface for pump running at 6000 rpm with inlet GVF 25% and bubble sizes (a) 63.5 μm (2.5 mils) (b) 76.2 μm (3 mils) and (c) 101.6 μm (4 mils)	59
Figure C4 Air volume fraction along blade to blade surface for pump running at 6000 rpm with inlet GVF 30% and bubble sizes (a) 63.5 μm (2.5 mils) (b) 76.2 μm (3 mils) and (c) 101.6 μm (4 mils)	60
Figure C5 Air volume fraction along blade to blade surface for pump running at 6000 rpm with inlet GVF 35% and bubble sizes (a) 63.5 μm (2.5 mils) (b) 76.2 μm (3 mils) and (c) 101.6 μm (4 mils)	60
Figure C6 Air volume fraction along impeller vanes for pump running at 6000 rpm with inlet GVF 13% and bubble sizes (a) 63.5 μm (2.5 mils) (b) 76.2 μm (3 mils) and (c) 101.6 μm (4 mils)	61
Figure C7 Air volume fraction along impeller vanes for pump running at 6000 rpm with inlet GVF 13% and bubble sizes (a) 63.5 μm (2.5 mils) (b) 76.2 μm (3 mils) and (c) 101.6 μm (4 mils)	61
Figure C8 Air volume fraction along impeller vanes for pump running at 6000 rpm with inlet GVF 13% and bubble sizes (a) 63.5 μm (2.5 mils) (b) 76.2 μm (3 mils) and (c) 101.6 μm (4 mils)	61
Figure C9 Air volume fraction along impeller vanes for pump running at 6000 rpm with inlet GVF 13% and bubble sizes (a) 63.5 μm (2.5 mils) (b) 76.2 μm (3 mils) and (c) 101.6 μm (4 mils)	62
Figure C10 Air volume fraction along impeller vanes for pump running at 6000 rpm with inlet GVF 13% and bubble sizes (a) 63.5 μm (2.5 mils) (b) 76.2 μm (3 mils) and (c) 101.6 μm (4 mils)	62
Figure C11 Iso-surface on impeller blades for GVF=60% for pump running at 6000 rpm with inlet GVF 13% and bubble sizes (a) 63.5 μm (2.5 mils) (b) 76.2 μm (3 mils) and (c) 101.6 μm (4 mils)	63
Figure C12 Iso-surface on impeller blades for GVF=60% for pump running at 6000 rpm with inlet GVF 18% and bubble sizes (a) 63.5 μm (2.5 mils) (b) 76.2 μm (3 mils) and (c) 101.6 μm (4 mils)	63

Figure C13 Iso-surface on impeller blades for GVF=60% for pump running at 6000 rpm with inlet GVF 25% and bubble sizes (a) 63.5 μm (2.5 mils) (b) 76.2 μm (3 mils) and (c) 101.6 μm (4 mils)	63
Figure C14 Iso-surface on impeller blades for GVF=60% for pump running at 6000 rpm with inlet GVF 30% and bubble sizes (a) 63.5 μm (2.5 mils) (b) 76.2 μm (3 mils) and (c) 101.6 μm (4 mils)	63
Figure C15 Iso-surface on impeller blades for GVF=60% for pump running at 6000 rpm with inlet GVF 35% and bubble sizes (a) 63.5 μm (2.5 mils) (b) 76.2 μm (3 mils) and (c) 101.6 μm (4 mils)	64
Figure C16 Air volume fraction along meridional surface for pump running at 6000 rpm with inlet GVF 13% and bubble sizes (a) 63.5 μm (2.5 mils) (b) 76.2 μm (3 mils) and (c) 101.6 μm (4 mils)	64
Figure C17 Air volume fraction along meridional surface for pump running at 6000 rpm with inlet GVF 18% and bubble sizes (a) 63.5 μm (2.5 mils) (b) 76.2 μm (3 mils) and (c) 101.6 μm (4 mils)	64
Figure C18 Air volume fraction along meridional surface for pump running at 6000 rpm with inlet GVF 25% and bubble sizes (a) 63.5 μm (2.5 mils) (b) 76.2 μm (3 mils) and (c) 101.6 μm (4 mils)	65
Figure C19 Air volume fraction along meridional surface for pump running at 6000 rpm with inlet GVF 30% and bubble sizes (a) 63.5 μm (2.5 mils) (b) 76.2 μm (3 mils) and (c) 101.6 μm (4 mils)	65
Figure C20 Air volume fraction along meridional surface for pump running at 6000 rpm with inlet GVF 35% and bubble sizes (a) 63.5 μm (2.5 mils) (b) 76.2 μm (3 mils) and (c) 101.6 μm (4 mils)	65
Figure D1 Water velocity along blade to blade surface for pump running at 3600 rpm with inlet GVF 13% and bubble sizes (a) 63.5 μm (2.5 mils) (b) 76.2 μm (3 mils) and (c) 101.6 μm (4 mils)	66
Figure D2 Water velocity along blade to blade surface for pump running at 3600 rpm with inlet GVF 19% and bubble sizes (a) 63.5 μm (2.5 mils) (b) 76.2 μm (3 mils) and (c) 101.6 μm (4 mils)	66
Figure D3 Water velocity along blade to blade surface for pump running at 3600 rpm with inlet GVF 24% and bubble sizes (a) 63.5 μm (2.5 mils) (b) 76.2 μm (3 mils) and (c) 101.6 μm (4 mils)	67

Figure D4 Water velocity along blade to blade surface for pump running at 3600 rpm with inlet GVF 29% and bubble sizes (a) 63.5 μm (2.5 mils) (b) 76.2 μm (3 mils) and (c) 101.6 μm (4 mils)	67
Figure D5 Water velocity along blade to blade surface for pump running at 3600 rpm with inlet GVF 35% and bubble sizes (a) 63.5 μm (2.5 mils) (b) 76.2 μm (3 mils) and (c) 101.6 μm (4 mils)	68
Figure D6 Water velocity along blade to blade surface for pump running at 3600 rpm with inlet GVF 40% and bubble sizes (a) 63.5 μm (2.5 mils) (b) 76.2 μm (3 mils) and (c) 101.6 μm (4 mils)	68
Figure D7 Water velocity along meridional surface for pump running at 3600 rpm with inlet GVF 13% and bubble sizes (a) 63.5 μm (2.5 mils) (b) 76.2 μm (3 mils) and (c) 101.6 μm (4 mils)	68
Figure D8 Water velocity along meridional surface for pump running at 3600 rpm with inlet GVF 19% and bubble sizes (a) 63.5 μm (2.5 mils) (b) 76.2 μm (3 mils) and (c) 101.6 μm (4 mils)	69
Figure D9 Water velocity along meridional surface for pump running at 3600 rpm with inlet GVF 24% and bubble sizes (a) 63.5 μm (2.5 mils) (b) 76.2 μm (3 mils) and (c) 101.6 μm (4 mils)	69
Figure D10 Water velocity along meridional surface for pump running at 3600 rpm with inlet GVF 29% and bubble sizes (a) 63.5 μm (2.5 mils) (b) 76.2 μm (3 mils) and (c) 101.6 μm (4 mils)	69
Figure D11 Water velocity along meridional surface for pump running at 3600 rpm with inlet GVF 35% and bubble sizes (a) 63.5 μm (2.5 mils) (b) 76.2 μm (3 mils) and (c) 101.6 μm (4 mils)	70
Figure D12 Water velocity along meridional surface for pump running at 3600 rpm with inlet GVF 40% and bubble sizes (a) 63.5 μm (2.5 mils) (b) 76.2 μm (3 mils) and (c) 101.6 μm (4 mils)	70
Figure D13 Water velocity along blade to blade surface for pump running at 6000 rpm with inlet GVF 13% and bubble sizes (a) 63.5 μm (2.5 mils) (b) 76.2 μm (3 mils) and (c) 101.6 μm (4 mils)	71
Figure D14 Water velocity along blade to blade surface for pump running at 6000 rpm with inlet GVF 18% and bubble sizes (a) 63.5 μm (2.5 mils) (b) 76.2 μm (3 mils) and (c) 101.6 μm (4 mils)	71

Figure D15 Water velocity along blade to blade surface for pump running at 6000 rpm with inlet GVF 25% and bubble sizes (a) 63.5 μm (2.5 mils) (b) 76.2 μm (3 mils) and (c) 101.6 μm (4 mils)	71
Figure D16 Water velocity along blade to blade surface for pump running at 6000 rpm with inlet GVF 30% and bubble sizes (a) 63.5 μm (2.5 mils) (b) 76.2 μm (3 mils) and (c) 101.6 μm (4 mils)	72
Figure D17 Water velocity along blade to blade surface for pump running at 6000 rpm with inlet GVF 35% and bubble sizes (a) 63.5 μm (2.5 mils) (b) 76.2 μm (3 mils) and (c) 101.6 μm (4 mils)	72
Figure D18 Water velocity along meridional surface for pump running at 6000 rpm with inlet GVF 13% and bubble sizes (a) 63.5 μm (2.5 mils) (b) 76.2 μm (3 mils) and (c) 101.6 μm (4 mils)	73
Figure D19 Water velocity along meridional surface for pump running at 6000 rpm with inlet GVF 18% and bubble sizes (a) 63.5 μm (2.5 mils) (b) 76.2 μm (3 mils) and (c) 101.6 μm (4 mils)	73
Figure D20 Water velocity along meridional surface for pump running at 6000 rpm with inlet GVF 25% and bubble sizes (a) 63.5 μm (2.5 mils) (b) 76.2 μm (3 mils) and (c) 101.6 μm (4 mils)	73
Figure D21 Water velocity along meridional surface for pump running at 6000 rpm with inlet GVF 30% and bubble sizes (a) 63.5 μm (2.5 mils) (b) 76.2 μm (3 mils) and (c) 101.6 μm (4 mils)	74
Figure D22 Water velocity along meridional surface for pump running at 6000 rpm with inlet GVF 35% and bubble sizes (a) 63.5 μm (2.5 mils) (b) 76.2 μm (3 mils) and (c) 101.6 μm (4 mils)	74

LIST OF TABLES

	Page
Table 1 Simulation cases.....	11
Table 2 Boundary conditions imposed on ESP CFD model	20
Table 3 Dimensionless pressure head with increasing air flow rates for pump running at 3600 rpm	22
Table 5 Dimensionless pressure head with increasing air flow rates for pump running at 6000 rpm	24
Table A1 Pressure head values at increasing GVF for pump running at 3600 rpm.....	45
Table A2 Pressure head values at increasing GVF for pump running at 6000 rpm.....	46
Table B1 Calculation of air mass flow rates from GVF for pump speed 3600 rpm	48
Table C1 Calculation of air mass flow rates from GVF for pump speed 6000 rpm	58

1. INTRODUCTION

Electric submersible pumps (ESP) are downhole equipment used to create artificial lift during oil and gas extraction. An ESP consists of a series of centrifugal pump stages driven by an electric motor. Upon rotation, the impeller imparts kinetic energy to the fluid through centrifugal action. The diffuser converts this kinetic energy into pressure. The fluid then flows through the next stage and the process continues.

Frequently, traces of gas are encountered in oil wells. When such a mixture of oil and gas flows through an ESP, the pressure head generated by the pump reduces, thus affecting the production capacity of the oil well. The extent of pump performance degradation depends on parameters such as the amount of gas entering the ESP, fluid properties, pump speed and geometry. Hence, it is important to study two-phase flow through an ESP to be able to better predict its performance under gassy conditions.

Patil [1] studied the effect of rotational speed on an ESP hydraulic performance for single-phase flow through a two-stage pump by using Computational Fluid Dynamics (CFD). The simulation results of single-phase flow through the pump were validated from experimental data. This project aims to understand the performance of this pump under two-phase flow conditions with water and air as the two fluids. It evaluates the pump parameters of a single stage of the ESP at increasing air volumes and increasing rotational speeds, by extending the same model for two-phase flow.

Gas flow through the pump can be evaluated by two methods, using a fixed-sized bubble model or Population Balance Model (PBM). In the fixed-size bubble model, the

gas is injected in the form of bubbles whose size remains constant throughout the flow. The Population Balance Model (PBM) emulates breakup and coalescence of bubbles, where the bubbles change diameters based on a list of discrete values. Fixed-size air bubbles are used in this study, and the results are compared with one case of PBM. The conditions for applicability of both these models are then investigated. A brief review of the literature related to modeling and experimental characterization of multiphase flow in pumps follows.

1.1. Pump head degradation due to two-phase flow

Through experimental observations of single phase and two-phase flow through a 7-stage GOULDS centrifugal pump, Izturiz [2] observed that pump head deterioration depends on GVF at the suction, gas distribution and size, pressure gradient through pump, suction pressure, rotational velocity and impeller geometry. A reduction in pressure head was seen in two-phase flow, as compared to a single-phase flow through the same setup. Two-phase flow also showed other effects such as regions of instability and pressure pulsations.

Number of blades on the impeller also affects the pump performance under two-phase flow. Murakami [3] found that, with enough blades (seven in the experiments), the pump performance degrades continuously as the amount of air admitted increases. However, an improvement in the pump performance was observed with lesser number of blades (three in the experiments). This was attributed to an improvement of the flow pattern in the impeller.

Noghrehkar and Furuya [4, 5] noted the physical mechanism leading to two-phase pump head degradation when the gas phase is non-condensable. Void fraction increases along the flow channel because the flow changes from bubbly regime to churn turbulent flow. This reduces the interfacial drag, thus increasing the gas and liquid velocity. In two-phase flow, the liquid phase accelerates to a greater extent in the impeller as compared to a single-phase flow. This in turn leads to severe degradation of pump head at the outlet. In effect, the pump head reduces with increasing air volume flowing through the pump [6-8]

1.2. Bubble size and distribution in centrifugal pumps

Pump performance depends on the size and distribution of gas phase. Air bubbles follow the same path through the pump as the liquid phase, provided they are small and buoyancy effects are negligible. The motion of a single bubble is described as [3]

$$M \frac{dV}{dt} = -\frac{1}{2} \rho A C_d (\bar{V} - \bar{W}) |\bar{V} - \bar{W}| - v \nabla p + (\rho v - M) g \sin \delta - \rho v C_v \left(\frac{d\bar{V}}{dt} - \frac{d\bar{W}}{dt} \right) \quad (1)$$

where the first term on the right-hand side represents the drag force, the second term the force due to pressure gradient, the third one the buoyancy due to gravitation and the last term the inertia force. Integrating this equation gives the position and velocity of the bubbles at all times.

Izturiz [2] used a flow loop with pharmaceutical needles having a diameter of 0.7 mm to inject bubbles in water flowing to the inlet of an ESP. It was observed that the bubble diameter decreased as the flow passed through successive stages. This is attributed to higher pressure at successive stages which gives rise to compressibility effect, thus reducing the bubble size.

Zhu [7, 8] varied bubble sizes in CFD simulations to match experimental results. The bubble sizes used in the simulations were 0.06, 0.125, and 0.19 mm for 5.54, 12.4, and 17.8% GVFs, respectively. Simulation results with constant bubble size showed a deviation from experimental data at higher GVFs. Hence, it was concluded that using constant bubble size is valid only for low GVFs.

Air bubbles flowing through an ESP might not necessarily be spherical in shape, but rather ellipsoidal. Minemura [9] captured the air flow through a centrifugal pump and calculated equivalent spherical diameter of bubbles from the minor and major axes. The air volume fraction at the inlet was small, 0.011-0.013 GVF, which resulted in an average bubble size of 0.5 mm and did not show an appreciable change over the circumference. A greater uniformity was seen in the bubble sizes as the pump speed increased from 600 rpm to 900 rpm. In an axial flow pump, the average bubble diameter at 1380 rpm reduced to 0.25 mm.

There is a slight increase in bubble size in the radial direction. For an axial flow pump rotating at 1380 rpm with 0.015 air volume fraction, it was observed that the bubbles are larger (0.38 mm) and varied in size at a section just before the impeller inlet. Within the impeller, the size of bubbles reduced and became nearly uniform (0.25 mm). Further down, the bubble size increased again, and the uniformity was lost. This was due to coalescence of bubbles. An increase in pump speed breaks down the bubbles and reduces their size [9].

Visualization of distribution of phases inside a pump can be accomplished experimentally or by CFD. Amoresano [6] used an experimental apparatus with a

transparent casing to observe gas phase within a centrifugal pump. A higher concentration of bubbles is observed near the high-pressure areas near the impeller blades. Murakami [3] also observed that at the impeller inlet, bubbles move faster than the fluid (water). Inside the impeller, there is an adverse pressure gradient and it causes the air bubbles to move slower than the surrounding water. Coalescence and accumulation of bubbles takes place where the pressure gradient changes sign.

It is also seen that the bubble size decreases with increasing rotational speed. At higher speeds, the air bubbles break down into smaller ones by the impeller blades [10]. The turbulent kinetic energy is smaller at low rotational speeds and this leads to coalescence and accumulation of bubbles. Moreover, pressure surging can occur at low rotational speeds and low GVFs. Hence, the two-phase performance of an ESP improves as the shaft speed increases [7].

Different flow patterns inside an ESP impeller were observed by varying water and air flow rates by Verde [11]. When the gas flow rate was low, a bubble flow pattern was seen with small bubbles having a spherical shape and larger ones having an irregular shape. The bubble size decreased with increase in rotation speed due to the increase in drag forces and turbulent intensity. With an increase in the gas fraction, the flow changed to an agglomerated bubble flow. Here, bubbles coalesced and drained slower than the liquid phase. With a further increase in gas fraction, gas pockets formed, which resulted from increased coalescence of bubbles, and remained stationary. Small bubbles broke from this structure and formed a recirculation region in a turbulence wake region downstream of the stationary bubble. Formation of gas pockets resulted in surging since

kinetic energy was not transferred efficiently to the liquid phase. Even greater gas fractions resulted in separation of the gas and liquid phases in the impeller, which resulted in near zero head.

Cubas [12] analyzed twelve different flow structures with decreasing liquid flow rate in a vertically mounted pump. Air was injected in the form of bubbles having sizes 0.5 to 4 mm depending on gas and liquid velocities. The air mass flow rate was kept at 0.63 kg/h and the liquid flow rates were reduced, thus increasing the GVF. It was observed that for single-phase flow, with continuous decrease of liquid flow rate, the static head increased. However, in case of two-phase flow, there was an abrupt head loss. The gas flow pattern changed from bubble flow to agglomerated bubble to gas pocket to annular flow. Severe pump head degradation was seen toward annular flow. With increased rotating speed, there was increased turbulence which reduced the bubble size. Bubble diameters having the highest size frequency were noted for the three speeds – 4 mm for 300 and 400 rpm and 2 mm for 500 rpm.

Two-phase flow in nuclear reactor cooling pump was visualized by using a high-speed video camera by Poullikas [13]. It was seen that gas bubbles accumulate in low pressure areas. At low gas fractions, greater concentration was seen near the eye of the impeller. As the amount of gas increased, gas accumulation increased along the passage length, width and height. If the percentage of gas was too high, it blocked the passage by accumulating between the back plate and the shroud. A pressure field was generated between impeller plates and shroud, due to rotating flow. Since gas and liquid have different densities, they separate under this pressure difference at high gas fractions.

1.3. CFD modelling of two-phase flow

CFD employs various approaches for modelling turbulence and multiphase flow. Four types of interphase interactions play an important role in multiphase flow in a pump: drag, added mass force, lift, and turbulent dispersion force. The virtual mass coefficient does not affect the two-phase flow model [4]. Drag force plays a dominant role in interfacial momentum transfer as compared to lift force [7, 8]. Magnitude of turbulent dispersion force is small as compared to the other forces and can be neglected [14].

In the impeller, there is a break-up of bubbles due to the high speed whereas in the diffuser, bubbles coalesce due to the low speed. With increased GVF, there is an increase in the break-up and coalescence of bubbles, and more gas accumulates near the hub. As a result, the flow pattern transforms to segregated flow and gas pocket flow, thus affecting the pump performance [14]. Constant bubble size results agreed well with experimental data at $\text{GVF} < 10\%$ [8].

Turbulence in a centrifugal pump is typically modelled using the $k-\varepsilon$ turbulence model. It is computationally efficient and reliable and takes less time to converge than other models. Eulerian-Eulerian multiphase model provides an effective means of modelling two phase flow, if the inlet bubble size is known. Volume of Fluid (VOF) model can be used when the bubble size it is not known [15]. The typical boundary conditions are mass flow and GVF at the impeller inlet, rotating impeller walls and stationary diffuser walls, pressure outlet and no-slip at walls. CFD simulations frequently use smooth wall conditions. This leads to an over-prediction of pressure head as compared to experimental results [7, 8].

The population balance model is a solution to a partial differential equation that represents the balance on the number of particles of a specific state. This accounts for breakage and coalescence. With high turbulence flows, large bubbles are less likely to exist. It is possible to model flow separation and slug flow with the population balance model. Water velocity increases since its flow path narrows down due to large gas volumes, thus reducing the resulting pressure [16]. This explains the resulting reduction in total pressure head at outlet in case of two-phase flow.

1.4. Empirical and analytical models for predicting bubble size

Although a generalized bubble size model for a centrifugal pump is not available, there are some empirical and semi-empirical models available. Murakami and Minemura [10, 17, 18] proposed the following equation for Sauter-mean diameter by photographing bubble size dispersion with a transparent casing. It is applicable for $GVF < 8\%$ and pump speeds between 1000 and 1500 rpm.

$$d_m = 21.82 \left(\frac{N}{6.862} \right)^{-\frac{3}{4}} (0.618 + 4.273\lambda) \quad (2)$$

Estevam [19] proposed the following equation for maximum bubble diameter based on an analogy to gas-liquid two-phase pipe flow

$$d_{max} = 1.17 \left(\frac{\sigma}{\rho_l} \right)^{\frac{3}{5}} \left(\frac{2f_{\beta,\omega}}{D_H} \right)^{-\frac{2}{5}} \quad (3)$$

Barrios [20] found a relation between bubble size, rotation speed and liquid properties from visual experimental data inside an ESP, and critical Weber number.

$$d_{b_surg} = 0.0348N^{0.8809}\lambda^{\frac{1}{4}}\left(\frac{\sigma}{\rho_l}\right)^{\frac{3}{5}}\frac{1}{(N^3r_1^2)^{\frac{2}{5}}} \quad (4)$$

Gamboa [21] found an alternative relation for maximum stable bubble size by incorporating gas density

$$d_{max} = 14.27\left(\frac{\sigma}{\rho_l}\right)^{\frac{3}{5}}\left(\frac{(\Omega D)^4}{\nu}\right)^{-\frac{2}{5}}\left(\frac{\rho_l}{\rho_g}\right)^{\frac{1}{5}}(1 + 191.7\lambda^{0.2}) \quad (5)$$

Zhu and Zhang [7, 18] performed CFD simulations of pump pressure increment under gassy flows. Based on their results, they estimated the bubble size as follows

$$d_{32} = 6.034\lambda\left(\frac{\sigma}{\rho_l}\right)^{\frac{3}{5}}\left(\frac{\Delta P q}{\rho_c V}\right)^{-\frac{2}{5}}\left(\frac{\rho_c}{\rho_d}\right)^{\frac{1}{5}} \quad (6)$$

The further sections describe implementation of CFD method for fixed bubble size simulations through an ESP.

2. ESP STAGE FLOW DOMAIN AND SIMULATION CASES

CFD analysis is performed on a single stage of an ESP. A standard mixed-flow impeller pump having size 4” and specific speed 2858 rpm is used to analyze two-phase flow through it. This is representative of a typical ESP used in conventional onshore oil wells. The pump consists of an impeller with 5 blades and a diffuser with 7 blades. The pump parts considered in the analysis are vanes, hub and shroud of both the impeller and diffuser. The figure below shows a simplified CAD model of the pump stage flow domain used for analysis.

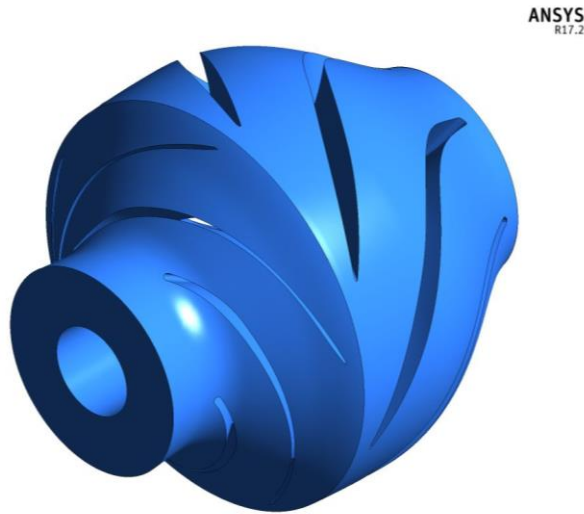


Figure 1 CAD model of electric submersible pump stage flow domain used for analysis

The ESP is simulated at two speeds, 3600 rpm and 6000 rpm, as these are the predicted speeds of operation for the end-user. Air in the form of bubbles is injected at the pump inlet, along with liquid water, and a constant pressure is held at the outlet. These

represent the boundary conditions for the flow. Mass flow rates of water are derived from pump affinity laws [1]. Gas Volume Fraction (GVF - ratio of volume of air to volume of water) at the inlet is varied from 0.13 to 0.40 for 3600 rpm and 0.13 to 0.35 for 6000 rpm. These values are chosen since they are representative of the GVFs encountered downhole by the end-user. GVFs are translated into air mass flow rates by using the corresponding phase densities and simple calculations included in Appendix B and C. Initially, Patil [1] extended the single-phase flow model mentioned in Section 1 to a multi-phase flow model for a fixed-bubble size of 2.5 mils. To establish a baseline for increasing bubble sizes using this data, fixed-size bubbles of 3 mils and 4 mils are chosen for further analysis. These would add to a database of possible equivalent bubble diameters for pressure heads that would be measured from experiments. The table below describes the simulation cases with increasing pump speed and air mass flow rates included in the numerical simulations. Each of these cases is run for bubble sizes 3 mils and 4 mils, which gives a total of 22 simulations.

Table 1 Simulation cases

Pump speed	Water mass flow	Air mass flow rate at	Bubble sizes
rpm	rate at inlet	inlet	μm (mils)
	kg/s	kg/s	
3600	5	0.05 – 0.15	76.2, 101.6 (3, 4)
6000	8	0.08 – 0.21	76.2, 101.6 (3, 4)

The outputs of these simulations are phase distribution inside the impeller based on air volume fraction, velocity distribution and pressure head at the inlet.

3. NUMERICAL MODEL

Multiphase flow through the pump is analyzed by CFD in ANSYS Fluent. This section describes how the simulations are set up and theoretical aspects of the models used. The pump model is meshed using hexahedral elements, as can be seen in the Figures 2 through 4. Hexahedral elements are a type of three-dimensional mesh elements, topologically equivalent to a cube. These reduce the number of nodes for the geometry as compared to tetrahedral elements [22]. The meshed model consists of 8.55 million nodes for a single stage. Patil [1] also conducted a grid independence study on two stages of this pump. Increasing the number of nodes to 8.8 million per stage resulted in a 0.13% decrease in the pressure head for single-phase flow, which was not a significant difference. Thus, the original mesh was chosen for further analysis. Figure 2 shows the mesh generated for the entire pump stage.

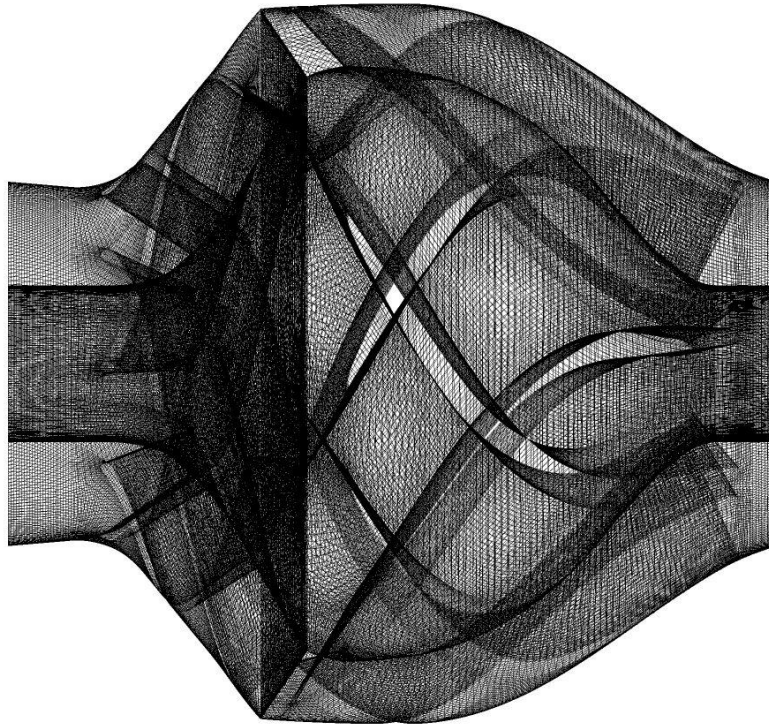


Figure 2 Meshed model of single stage of ESP

Figure 3 shows a zoomed-in view of mesh on the impeller vanes and hub. This is a critical step since impeller vanes influence air volume distribution and velocity.

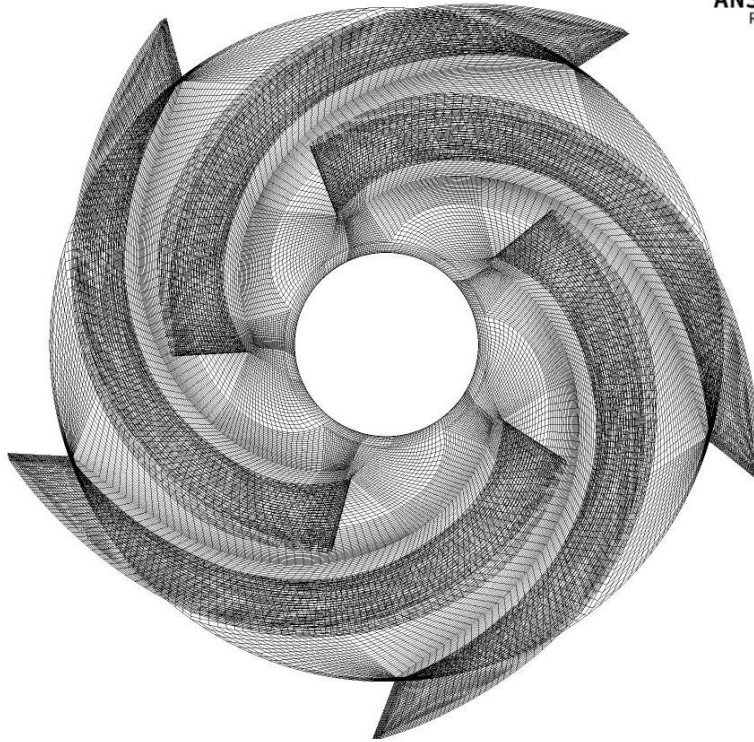


Figure 3 Side view of mesh on impeller vanes and hub as viewed from mass inlet end

Similarly, the diffuser vanes also influence fluid distribution and velocity. Figure 4 below shows an isolated view of the mesh on diffuser vanes and hub.

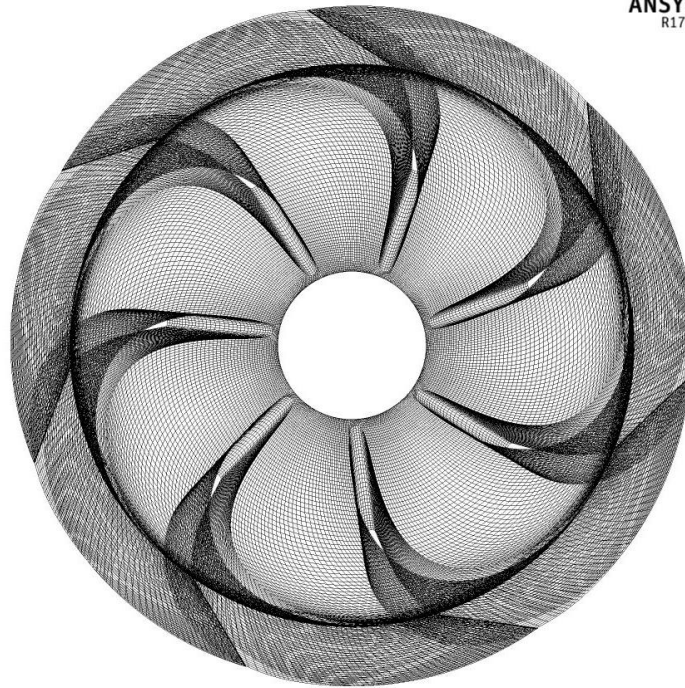


Figure 4 Side view of mesh on diffuser vanes and hub as viewed from pressure outlet end

The solver then generates and solves the transport equations using this meshed model, as described in the following sections.

3.1. Conservation Equations

Three dimensional Navier-Stokes equations are solved to obtain the output parameters, namely, velocity, pressure and phase distribution. A multiphase simulation is set up using the Eulerian multiphase model available in ANSYS Fluent. In this model, pressure for all the phases is the same, and momentum and continuity equations are solved for each phase individually. The primary phase is liquid water and the secondary phase is air with a fixed bubble size.

Initially, a volume fraction equation is solved by implicit formulation. Volume fraction of a phase denotes the physical space occupied by it, relative to the total volume of all phases. If α_q is the volume fraction of phase q , volume of that phase is found by the following equation [23].

$$V_q = \int \alpha_q dV \quad (7)$$

Also, from algebra, the summation of all volume fractions would be one [23].

$$\sum_{q=1}^n \alpha_q = 1 \quad (8)$$

Next, the conservation of mass, momentum and energy equations are solved. A general equation for conservation of mass of a phase q follows. It is a mass balance equation that considers change in mass with respect to time, transfer of mass between two phases and a source term. In this case, there is no mass transfer between phases and no source of mass [23].

$$\frac{1}{\rho_{rq}} \left(\frac{\partial}{\partial t} (\alpha_q \rho_q) + \nabla \cdot (\alpha_q \rho_q \vec{v}_q) = \sum_{p=1}^n (\dot{m}_{pq} - \dot{m}_{qp}) \right) \quad (14)$$

Further, the conservation of momentum equation is

$$\begin{aligned} & \frac{\partial}{\partial t} (\alpha_q \rho_q \vec{v}_q) + \nabla \cdot (\alpha_q \rho_q \vec{v}_q \vec{v}_q) \\ & = -\alpha_q \nabla p + \nabla \cdot \overline{\overline{\tau}}_q + \alpha_q \rho_q \vec{g} + \sum_{p=1}^n (K_{pq} (\vec{v}_p - \vec{v}_q) + \dot{m}_{pq} \vec{v}_{pq} \\ & - \dot{m}_{qp} \vec{v}_{qp}) + (\overline{F}_q + \vec{F}_{lift,q} + \vec{F}_{wl,q} + \vec{F}_{vm,q} + \vec{F}_{td,q}) \end{aligned} \quad (15)$$

In the equation above, $\overline{\overline{\tau}}_q$ is the q^{th} phase stress-strain tensor and is given by equation (11) [23].

$$\overline{\overline{\tau}}_q = \alpha_q \mu_q (\nabla \vec{v}_q + \vec{v}_q^T) + \alpha_q \left(\lambda_q - \frac{2}{3} \mu_q \right) \nabla \cdot \vec{v}_q \vec{I} \quad (11)$$

The equation for conservation of energy accounts for enthalpy change of the phases and is described as [23]

$$\begin{aligned} & \frac{\partial}{\partial t} (\alpha_q \rho_q h_q) + \nabla \cdot (\alpha_q \rho_q \vec{u}_q h_q) \\ & = \alpha_q \frac{dp_q}{dt} + \overline{\overline{\tau}}_q \cdot \nabla \vec{u}_q - \nabla \cdot \vec{q}_q + S_q + \sum_{p=1}^n (Q_{pq} + \dot{m}_{pq} h_{pq} \\ & \quad - \dot{m}_{qp} h_{qp}) \end{aligned} \quad (13)$$

3.2. Phase Interactions

Various interface interactions can be modeled between the continuous water phase and air bubbles. Each of the phenomena and the corresponding suitable model for this case are described below.

3.2.1. Interfacial area concentration

Interfacial area concentration is the interfacial area between two phases in one-unit volume of the mixture. Fluent offers four models that can be used to algebraically calculate this parameter. The default model – “Symmetric model” is used for this multiphase flow simulation. It calculates the interfacial area concentration as follows [23].

$$A_i = \frac{6\alpha_p(1 - \alpha_p)}{d_p} \quad (16)$$

This is based on the surface area to volume ratio for a spherical bubble.

3.2.2. Fluid-fluid exchange coefficient

The interphase momentum exchange coefficient is calculated using the following formula for bubbly flows [23].

$$K_{pq} = \frac{\rho_p f}{6\tau_p} d_p A_i \quad (17)$$

$$\tau_p = \frac{\rho_p d_p^2}{18\mu_q} \quad (18)$$

In these simulations, the Tomiyama et al. model [23] is employed since it is well suited to gas-liquid flows with bubbles. It defines the drag coefficient as follows [23].

$$f = \frac{C_D Re}{24} \quad (19)$$

$$Re = \frac{\rho_q |\vec{v}_p - \vec{v}_q| d_p}{\mu_q} \quad (20)$$

$$C_D = \max \left(\min \left(\frac{24}{Re} (1 + 0.15 Re^{0.687}), \frac{72}{Re} \right), \frac{8}{3} \frac{Eo}{Eo + 4} \right) \quad (21)$$

$$Eo = \frac{g(\rho_q - \rho_p) d_p^2}{\sigma} \quad (22)$$

From previous studies conducted, it is reported that the lift force for small particles can be neglected and drag force is the only dominant force [7, 8]. Hence, lift force is not modeled in the simulations.

3.2.3. Wall lubrication force

Wall lubrication force accounts for bubbles being pushed away from solid boundaries in the domain and is found from equation (23) [23].

$$\vec{F}_{wl} = C_{wl}\rho_q\alpha_p|\vec{v}_q - \vec{v}_p|^2\vec{n}_w \quad (23)$$

The wall lubrication coefficient is calculated using the Antal et al. model [23], which defines it as follows [23].

$$C_{wl} = \max\left(0, \frac{C_{w1}}{d_b} + \frac{C_{w2}}{y_w}\right) \quad (24)$$

3.3. Turbulence Modeling

Shi [24] conducted an analysis to evaluate different turbulence models using CFD simulations of a helicoaxial pump. No significant difference was observed in the models compared to experimental data. Hence, realizable k - ε model is selected for modeling turbulent flow [25]. It is seen to be more stable than the standard k - ε model [22]. Equations (25) - (29) describe this model [23].

$$\frac{\partial}{\partial t}(\rho k) + \frac{\partial}{\partial x_j}(\rho k u_j) = \frac{\partial}{\partial x_j}\left[\left(\mu + \frac{\mu_t}{\sigma_k}\right)\frac{\partial k}{\partial x_j}\right] + G_k + G_b - \rho\varepsilon - Y_M + S_k \quad (25)$$

$$\begin{aligned} & \frac{\partial}{\partial t}(\rho\varepsilon) + \frac{\partial}{\partial x_j}(\rho\varepsilon u_j) \\ & = \frac{\partial}{\partial x_j}\left[\left(\mu + \frac{\mu_t}{\sigma_\varepsilon}\right)\frac{\partial\varepsilon}{\partial x_j}\right] + \rho C_1 S\varepsilon - \frac{\rho C_2 \varepsilon^2}{k + \sqrt{\nu\varepsilon}} + C_{1\varepsilon}\frac{\varepsilon}{k}C_{3\varepsilon}G_b + S_\varepsilon \end{aligned} \quad (26)$$

Where

$$C_1 = \max\left[0.43, \frac{\eta}{\eta+5}\right], \eta = S\frac{k}{\varepsilon}, S = \sqrt{2S_{ij}S_{ij}}$$

$$\mu_t = \rho C_\mu \frac{k^2}{\varepsilon} \quad (27)$$

$$C_\mu = \frac{1}{A_0 + A_s \frac{kU^*}{\varepsilon}} \quad (28)$$

$$U^* \equiv \sqrt{S_{ij}S_{ij} + \tilde{\Omega}_{ij}\tilde{\Omega}_{ij}}$$

$$\tilde{\Omega}_{ij} = \Omega_{ij} - 2\varepsilon_{ijk}\omega_k, \Omega_{ij} = \bar{\Omega}_{ij} - \varepsilon_{ijk}\omega_k, A_0 = 4.04, A_S = \sqrt{6} \cos\phi \quad (29)$$

$$\phi = \frac{1}{3} \cos^{-1}(\sqrt{W}), W = \frac{S_{ij}S_{jk}S_{ki}}{\xi^3}, \tilde{S} = \sqrt{S_{ij}S_{ij}}, S_{ij} = \frac{1}{2} \left(\frac{\partial u_j}{\partial x_i} + \frac{\partial u_i}{\partial x_j} \right)$$

3.4. Boundary conditions

To be able to solve the preceding differential equations, boundary conditions need to be specified. The diffuser of the ESP is stationary, and the impeller rotates at the given speed. Hence, to translate this into boundary conditions, the impeller is specified as a moving wall with speeds 3600 rpm or 6000 rpm. Mass flow rates of water and air are specified at the inlet surface, with a fixed bubble size for the air phase. The values of these mass flow rates are calculated from affinity laws as used in previous simulations for single phase flow [25]. A constant value of pressure is specified at the outlet, as a reference.

Table 2 Boundary conditions imposed on ESP CFD model

Surface	Boundary Condition
Inlet	Water and air mass flow rates
	Air bubble diameter
Outlet	Pressure
Impeller	Moving wall
Diffuser	Stationary wall

3.5. Solution

Once all the input parameters and boundary conditions are indicated, solution parameters are set before running the calculations. First order upwind scheme is utilized for spatial discretization of momentum, volume fraction, turbulent kinetic energy, turbulent dissipation rate and energy equations. The time step for these transient solutions is chosen such that it corresponds to 1° rotation of the impeller. For 3600 rpm, 1 revolution takes $\frac{60}{3600} = 0.01667$ s. The impeller rotates 360° during this time. Hence, for 1° rotation, it takes $\frac{0.01667}{360} = 4.62 * 10^{-5}$ s.

Similarly, for 6000 rpm, 1 revolution takes $\frac{60}{6000} = 0.01$ s. The impeller rotates 360° during this time. Hence, for 1° rotation, it takes $\frac{0.01}{360} = 2.77 * 10^{-5}$ s.

The pressure-velocity coupled equations are solved using a pressure based coupled algorithm. Inlet pressures are periodically monitored, and the simulations are run until the residuals stabilize and their mean value is 10^{-3} .

4. RESULTS

Once all the simulations are complete, data files are imported into CFD-Post to generate plots of the output variables. Plots and results for the each of the three monitored output parameters – namely pressure head at inlet, air volume fraction and velocity - are shown below and inferences are drawn from the results. Results for bubble size 2.5 mils are available and are used for comparison.

4.1. Dimensionless pressure head

A constant pressure boundary condition is imposed at the pump outlet. Hence, the pressure head is calculated by measuring the pressure at the inlet and taking the difference of the two. Dimensionless pressure head is then calculated by taking the ratio of pressure head for the case of two-phase flow and that for single phase flow, at the same speed. The following table and graph give the values of dimensionless heads obtained for increasing air flow rates at 3600 rpm. The actual numerical values can be found in Appendix A.

Table 3 Dimensionless pressure head with increasing air flow rates for pump running at 3600 rpm

Mass flow rate of water (kg/s)	Mass flow rate of air (kg/s)	GVF	Dimensionless pressure head for bubble sizes -		
			63.5 μm (2.5 mils)	76.2 μm (3 mils)	101.6 μm (4 mils)
5	0.05	0.13	0.82	0.82	0.81
5	0.07	0.19	0.77	0.77	0.73

Table 3 Continued

Mass flow rate of water (kg/s)	Mass flow rate of air (kg/s)	GVF	Dimensionless pressure head for bubble sizes -		
			63.5 μm	76.2 μm	101.6 μm
			(2.5 mils)	(3 mils)	(4 mils)
5	0.09	0.24	0.72	0.72	0.69
5	0.11	0.29	0.67	0.67	0.65
5	0.13	0.35	0.62	0.62	0.60
5	0.15	0.40	0.62	0.59	0.58

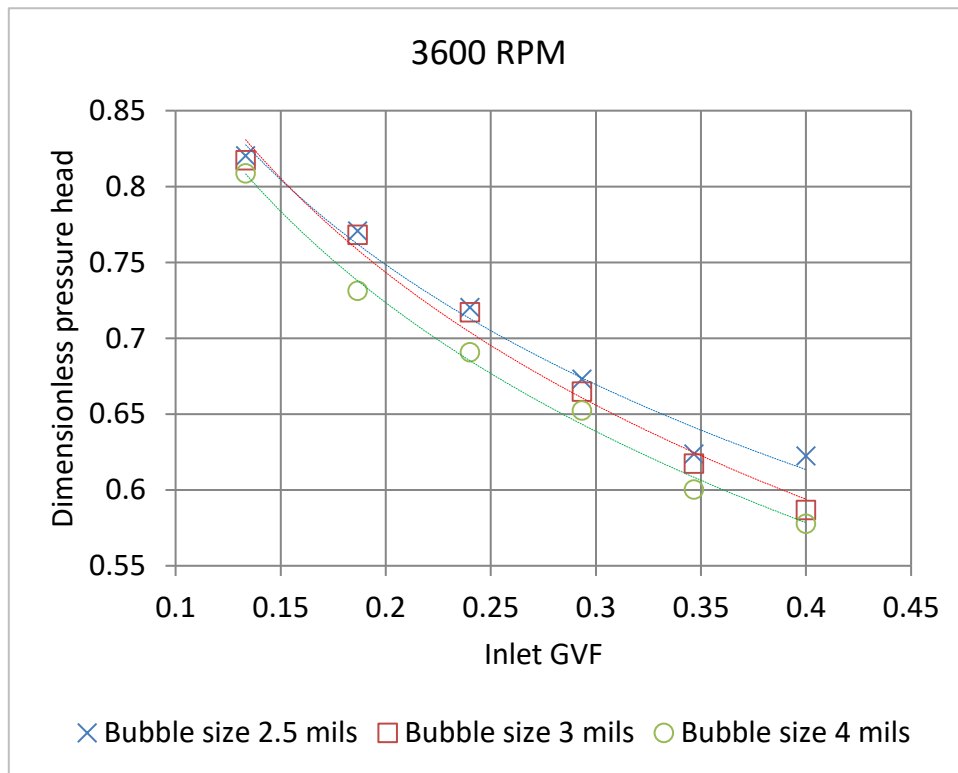


Figure 5 Dimensionless pressure head with increasing GVF for pump running at 3600 rpm for three cases of bubble sizes - 63.5 μm (2.5 mils), 76.2 μm (3 mils) and 101.6 μm (4 mils).

Similarly, Table 4 and Figure 6 provide the pressure head obtained for increasing air flow rates at 6000 rpm.

Table 4 Dimensionless pressure head with increasing air flow rates for pump running at 6000 rpm

Mass flow rate of water (kg/s)	Mass flow rate of air (kg/s)	GVF	Dimensionless pressure head for bubble sizes -		
			63.5 μm (2.5 mils)	76.2 μm (3 mils)	101.6 μm (4 mils)
			8	0.08	0.13
8	0.11	0.18	0.72	0.71	0.69
8	0.15	0.25	0.70	0.66	0.63
8	0.18	0.30	0.65	0.64	0.61
8	0.21	0.35	0.60	0.59	0.55

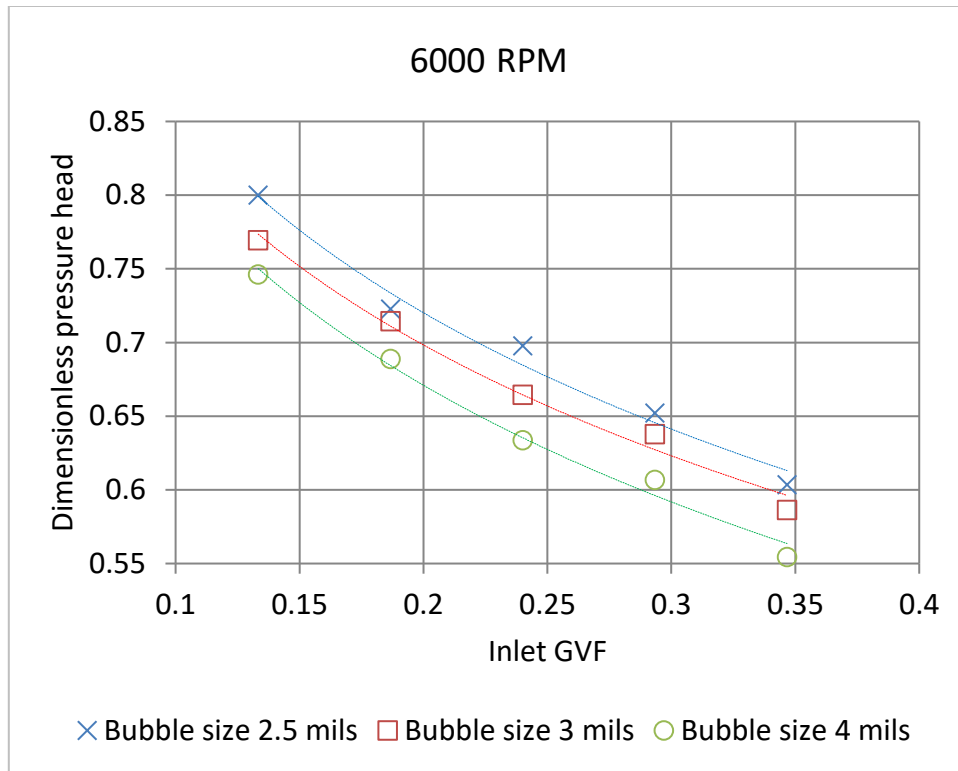


Figure 6 Dimensionless pressure head with increasing GVF for pump running at 6000 rpm with for three cases of bubble sizes - 63.5 μm (2.5 mils), 76.2 μm (3 mils) and 101.6 μm (4 mils).

Figure 6 shows that the dimensionless pressure head decreases approximately linearly with increasing air volume fraction. This is consistent with observations from literature [18]. With increasing bubble size, dimensionless head degradation is seen for a higher speed of 6000 rpm, while the values are very close for 3600 rpm. The physical mechanism leading to this phenomenon is that there is greater acceleration of the liquid water phase through the impeller, as compared to a single-phase flow. This is because of reduced area due to presence of air bubbles. This area is further reduced with increased bubble size and increased air mass flow rates, thus leading to increased water velocity. As a result, there is a reduction in pressure head as observed in the results [4, 5]. In this case,

since the bubble sizes are very small and numerically close to each other, the magnitudes of pressure head degradation are appreciably close to each other.

4.2. Effect of bubble size

Bubble size influences phase distribution inside the pump. Two cases, namely, 3600 rpm, 0.35 GVF and 6000 rpm, 0.35 GVF, are selected for reference, and the effect of bubble size is seen from the results for bubble sizes 2.5 mils, 3 mils and 4 mils. An iso-surface plot on the impeller vanes provides a visual representation of the phase distribution inside the pump. The blue geometry in the figures below depicts the impeller hub and vanes. Results for inlet gas volume fraction 0.35 at both the pump speeds and each of the bubble sizes are considered here for reference. The green portion in Figures 7 and 8 depicts the area where air bubbles are occupying 60% of the total fluid volume.

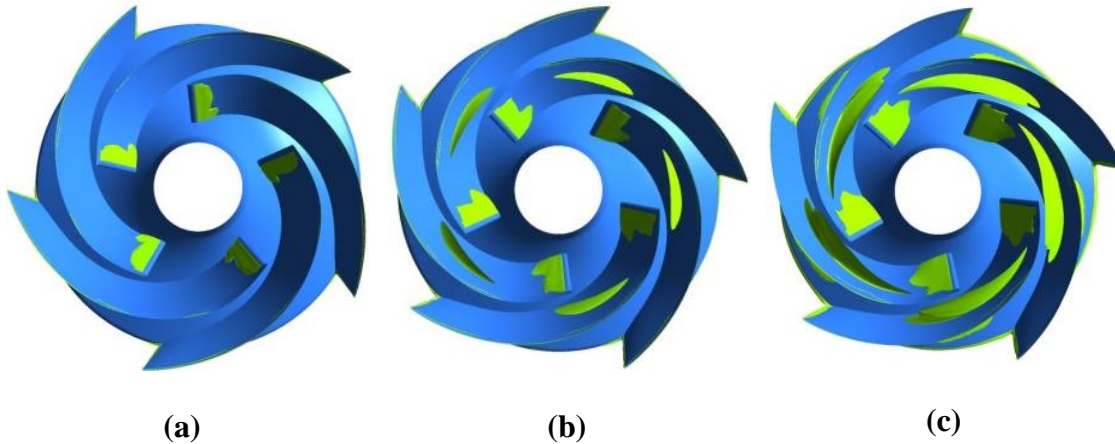


Figure 7 Iso-surface on impeller blades for GVF=60% for pump running at 3600 rpm with inlet GVF 35% and bubble sizes (a) 63.5 μm (2.5 mils) (b) 76.2 μm (3 mils) and (c) 101.6 μm (4 mils)

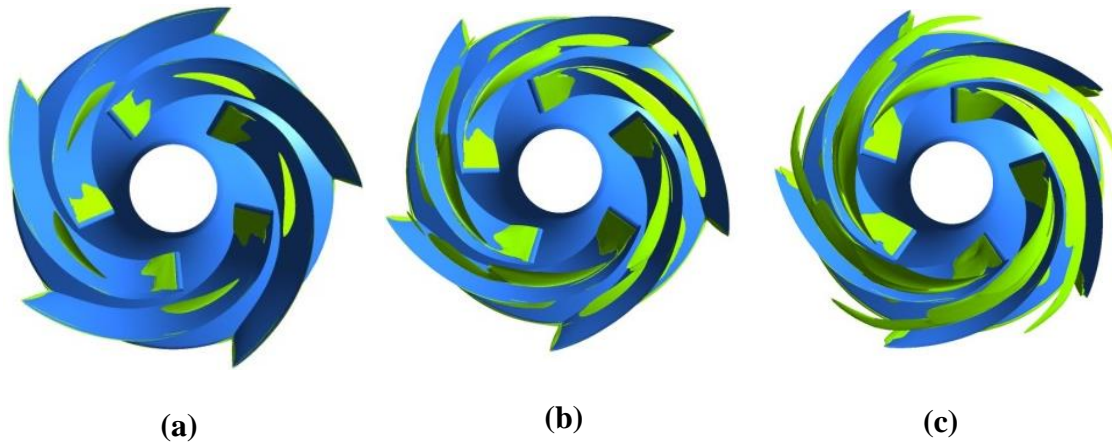
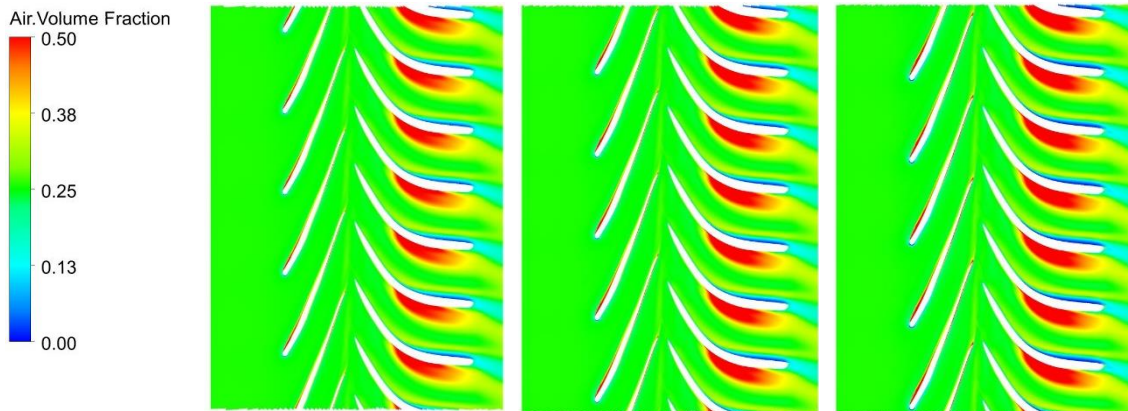


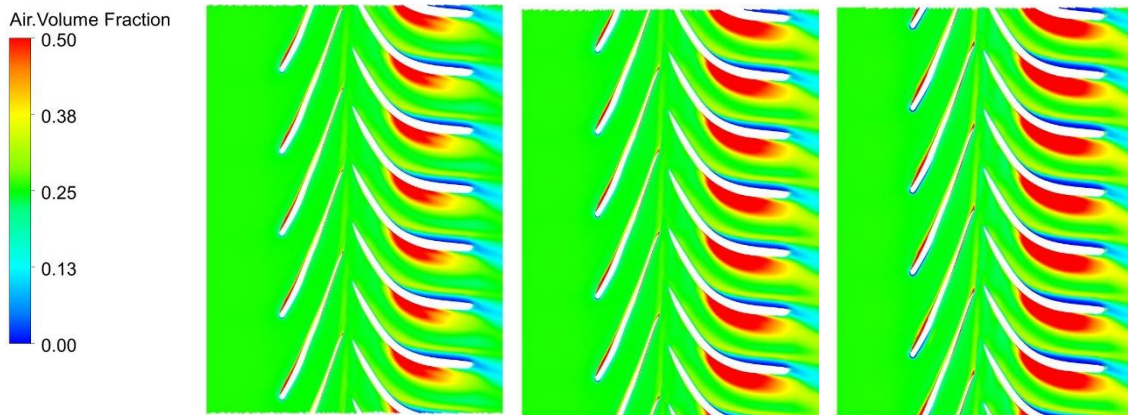
Figure 8 Iso-surface on impeller blades for GVF=60% for pump running at 6000 rpm with inlet GVF 35% and bubble sizes (a) 63.5 μm (2.5 mils) (b) 76.2 μm (3 mils) and (c) 101.6 μm (4 mils)

The areas on the impeller with 60% air volume fraction increase with an increase in bubble size, for the same inlet gas volume fraction. This is due to the simple fact that bigger bubbles will occupy a greater area once they aggregate. This will increase the area where 60% of the fluid is gas. Also, it is seen that the air bubbles tend to concentrate near the center of the blades and move further away as their size and volume increases, which was also observed by Poullikas [13]. This can be attributed to the increase in centrifugal force acting upon them. Figures 9 and 10 depict air volume fraction across the impeller and diffuser blades. The left half of the plots show the impeller, while the right half is the diffuser.



(a) (b) (c)

Figure 9 Air volume fraction along blade to blade surface for pump running at 3600 rpm with inlet GVF 35% and bubble sizes (a) 63.5 μm (2.5 mils) (b) 76.2 μm (3 mils) and (c) 101.6 μm (4 mils)



(a) (b) (c)

Figure 10 Air volume fraction along blade to blade surface for pump running at 6000 rpm with inlet GVF 35% and bubble sizes (a) 63.5 μm (2.5 mils) (b) 76.2 μm (3 mils) and (c) 101.6 μm (4 mils)

It is seen from the blade to blade plots that the concentration of gas phase increases slightly with an increase in bubble size. The gas phase is mainly concentrated near the diffuser and impeller blades, which is also due to the same reason mentioned above and the pump geometry.

Another parameter monitored is the water velocity, whose variation with bubble size is shown in Figures 11 and 12. Note that the scales are different for 3600 rpm and 6000 rpm.

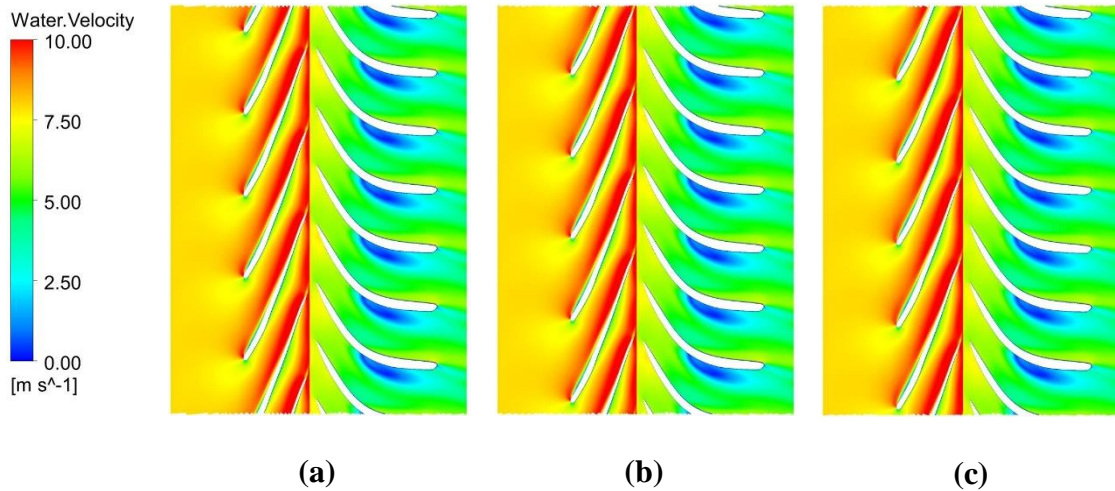


Figure 11 Water velocity along blade to blade surface for pump running at 3600 rpm with inlet GVF 35% and bubble sizes (a) 63.5 μm (2.5 mils) (b) 76.2 μm (3 mils) and (c) 101.6 μm (4 mils)

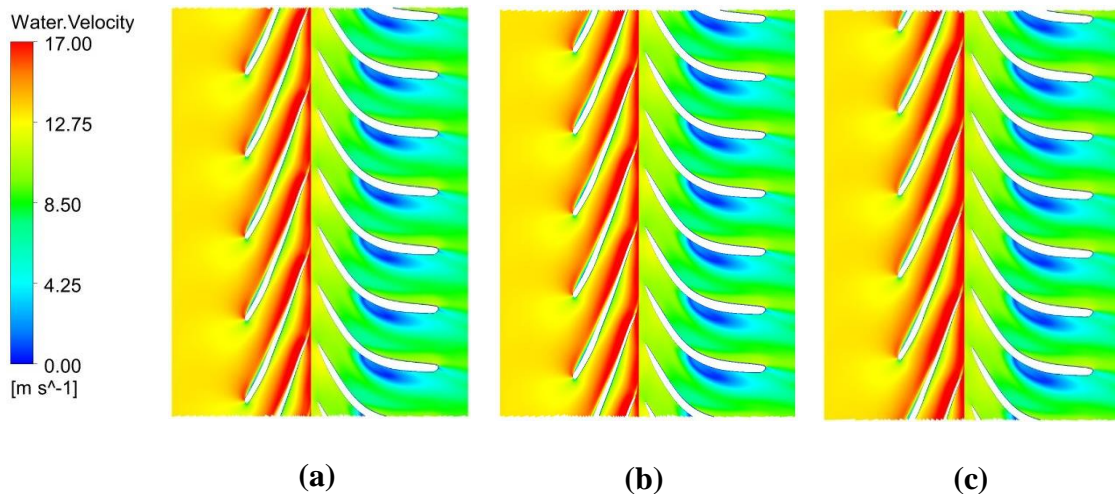


Figure 12 Water velocity along blade to blade surface for pump running at 6000 rpm with inlet GVF 35% and bubble sizes (a) 63.5 μm (2.5 mils) (b) 76.2 μm (3 mils) and (c) 101.6 μm (4 mils)

Velocities of air and water are specified at the inlet. Since the velocities are being imposed in the model, a considerable variation is not seen with an increase in bubble size at both speeds and cannot be generalized.

Plots for all cases of GVFs, bubble sizes and speeds are included in Appendix B for 3600 rpm and Appendix C for 6000 rpm. They also show the variation of GVF along a meridional plane.

4.3. Effect of rotational speed

To analyze the effect of rotational speed, results of cases with gas volume fraction 25% and bubble size 3 mils are presented here for the two speeds, 3600 rpm and 6000 rpm in Figures 13 to 15.

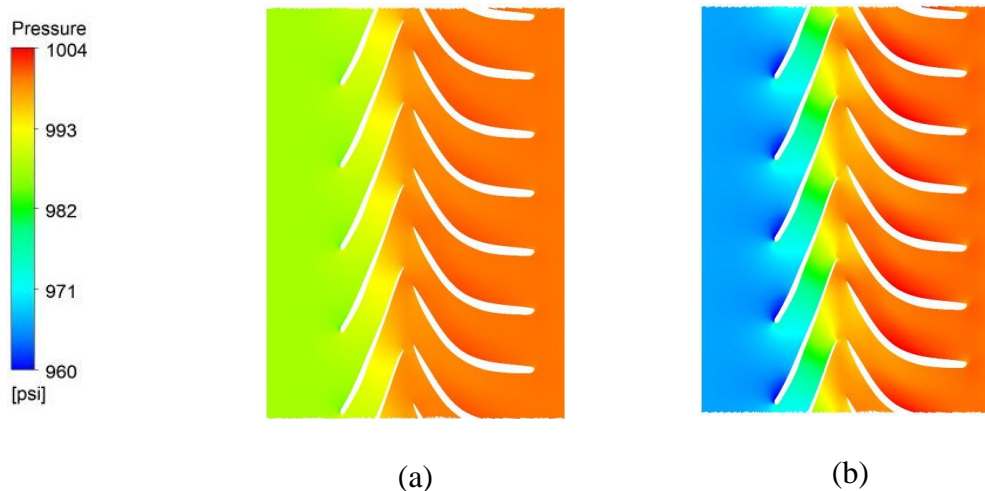


Figure 13 Pressure distribution along blade to blade surface for pump with inlet GVF 25% and bubble size 3 mils for running speeds (a) 3600 rpm and (b) 6000 rpm

Rotational speed has a significant impact on pressure distribution inside the pump. From Figure 13, a greater pressure drop is seen near the inlet for 6000 rpm as compared to 3600 rpm. This is expected since increasing the pump speed and flow rate generates a

higher head due to increased forces. Keeping a constant pressure at the outlet and measuring the inlet pressure, actual pressure heads for the speeds 3600 rpm and 6000 rpm are 12.77 psi and 33.80 psi respectively. However, considering the dimensionless heads which have single phase heads as reference, the values become 0.72 and 0.66, respectively. This leads to the conclusion that head degradation due to two-phase flow is aggravated at higher speeds. This may be due to increased drag and turbulence forces at higher speed.

The blade-blade plots in Figure 14 indicate the changes in phase distribution inside the impeller and diffuser.

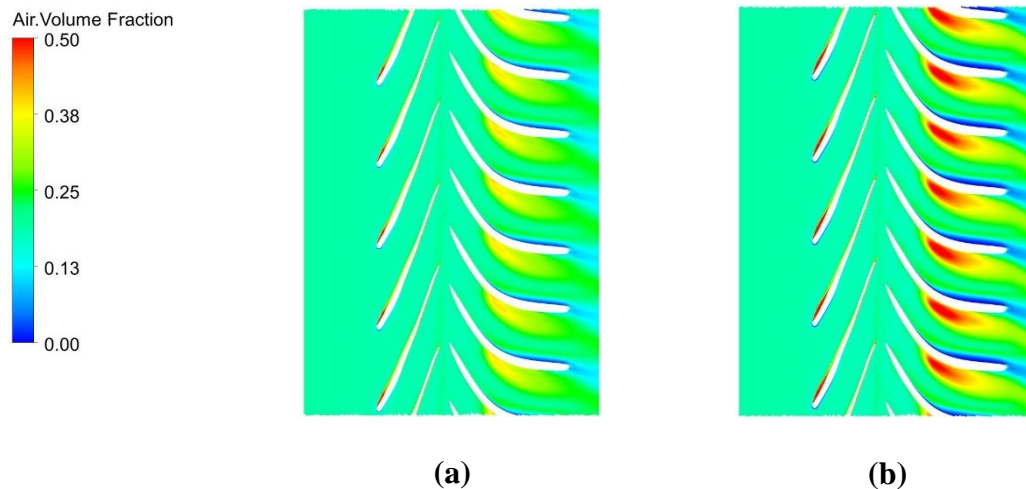


Figure 14 Air volume fraction distribution along blade to blade surface for pump with inlet GVF 25% and bubble size 3 mils for running speeds (a) 3600 rpm and (b) 6000 rpm

Greater concentration of bubbles is seen near the blades for 6000 rpm compared to 3600 rpm, as seen in Fig. 14. An increase in rotational speed is quadratically related to force due to pressure gradient and acts against the motion of bubbles. It is for this

reason that bubbles accumulate near the impeller channels more evenly for higher rotational speed [5]. Also, an increased pump speed increases turbulence in the liquid, thus adding to this effect.

Further, water velocities inside the pump are seen to vary as per the plots in Figure 15.

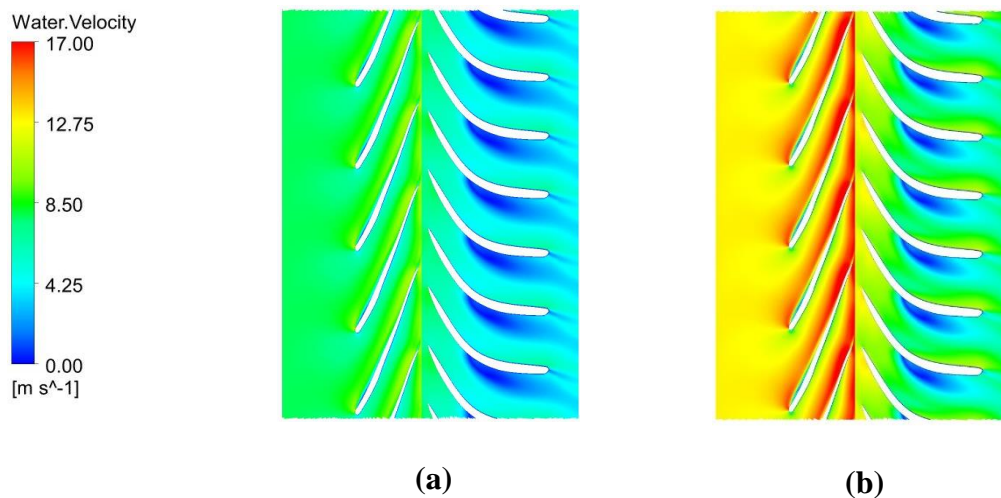


Figure 15 Water velocity distribution along blade to blade surface for pump with inlet GVF 25% and bubble size 3 mils for running speeds (a) 3600 rpm and (b) 6000 rpm

The velocity is imposed at the pump inlet through the mass flow rates of water, which were obtained from affinity laws for the two speeds, respectively [25]. Hence, the water velocity plots are driven by these input values of mass flow rates, which are 5 kg/s at 3600 rpm and 8 kg/s at 6000 rpm.

This completes the analysis for fixed-size bubbles flowing through the ESP single stage. To summarize, these CFD simulations predict the pump performance at increasing air flow rates and pump speeds. Further experimental data would validate the use of these bubble sizes for specific observed pressure head values.

Additionally, results from the fixed-size bubble models are compared with one case of Population Balance Model (PBM) that captures the formation of large gas pockets. This comparison is presented in the following section.

4.4. Comparison with population balance model

Bubbles tend to break or coalesce inside a pump instead of having the same size throughout. ANSYS offers the capability to simulate breakage and coalescence of bubbles with the 'Population Balance Model (PBM)'. It takes a list of discrete bubble sizes from the user. During the process of breakage and coalescence, the bubble diameters then increase or decrease as per these discrete sizes.

PBM is a solution to a partial differential equation that represents the balance on the number of particles of a specific state. Results of such a model applied to the ESP under study are available at 3600 rpm, 5 kg/s water flow rate and 0.05 kg/s air flow rate (GVF=0.13) where bubble size varies from 0.1 mils to 6.4 mils. They are compared with the corresponding cases of constant bubble size simulation of 3 and 4 mils in the following figures.

From Figure 16, it is seen that the non-dimensional value of pressure in the three cases is comparable, although population balance model shows a greater depreciation of pressure head. This is due to consideration of coalescence of bubbles which increases gas pocket size in the pump, thus leading to greater pressure loss.

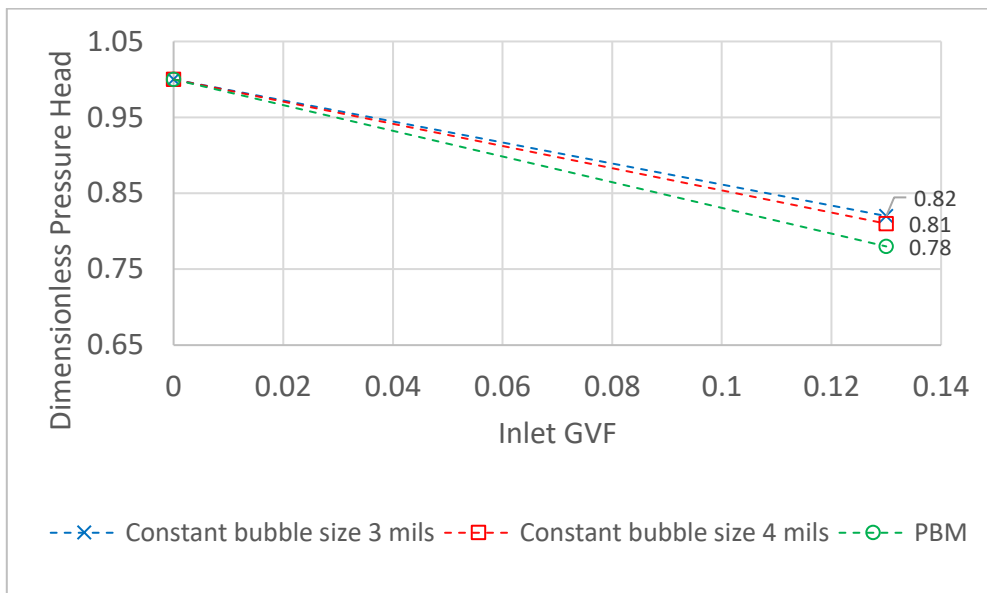


Figure 16 Comparison of dimensionless pressure head for pump running at 3600 rpm and 13% GVF for constant bubble size models and population balance model

Figures 17 through 19 compare the models based on the phase distribution inside the pump. Figure 19 is an iso-surface plot, where the blue geometry is the impeller hub and vanes, and the green portion of the plot is area where 60% of the total volume is occupied by air.

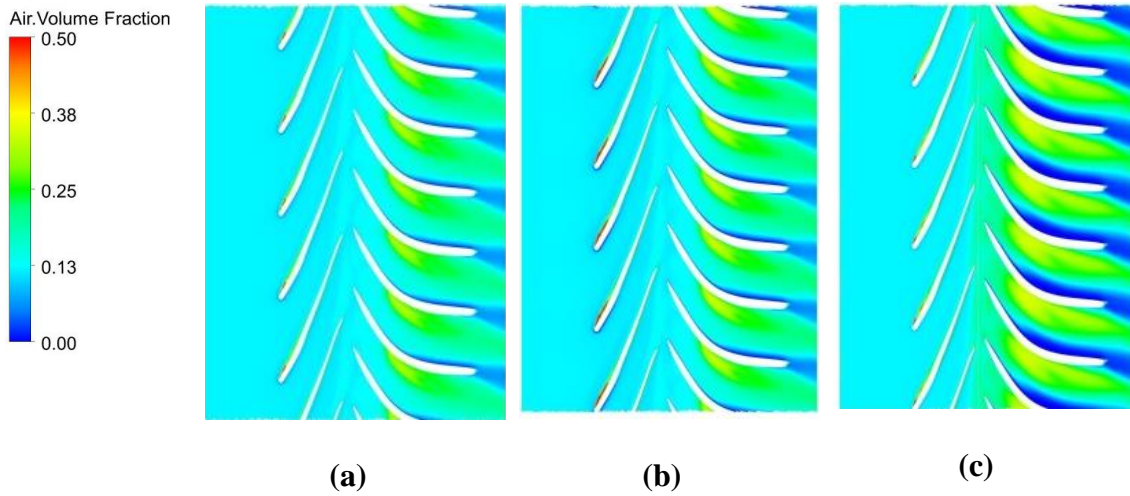


Figure 17 Air volume fraction distribution along blade to blade surface for pump running at 3600 rpm with inlet GVF 13% and (a) constant bubble size 3mils (b) constant bubble size 4mils (c) population balance model

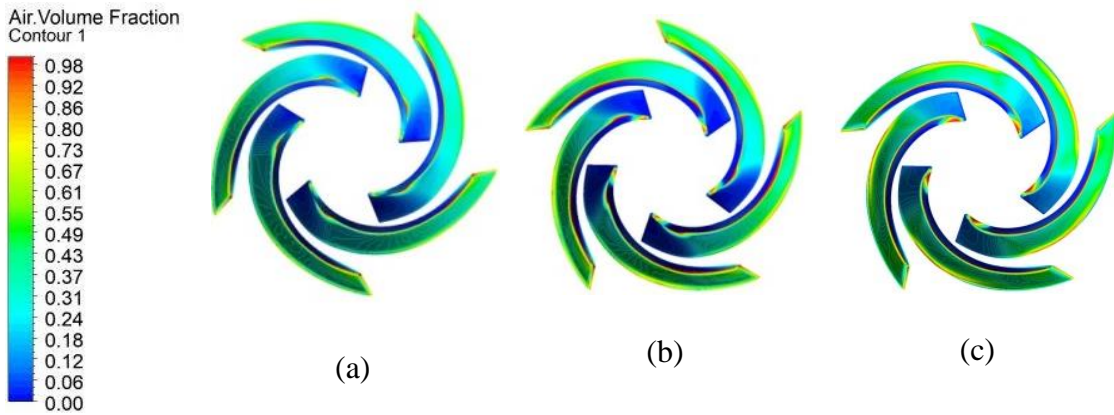


Figure 18 Air volume fraction distribution along impeller vanes for pump running at 3600 rpm with inlet GVF 13% and (a) constant bubble size 3mils (b) constant bubble size 4mils (c) population balance model

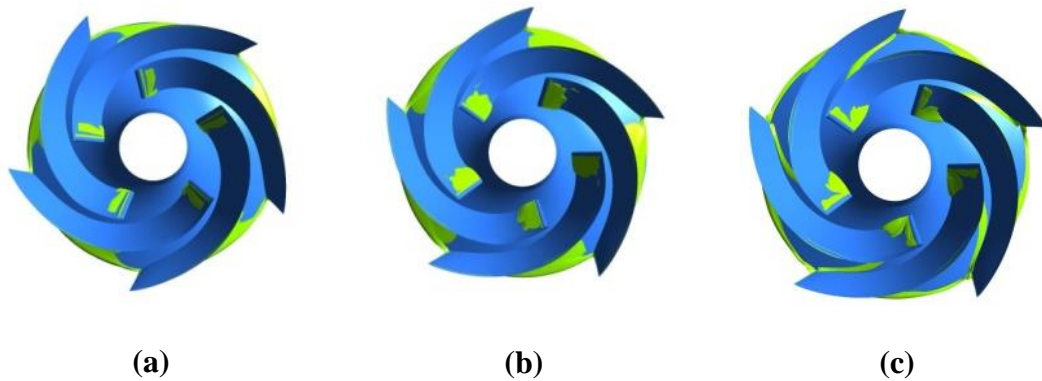


Figure 19 Iso-surface on impeller blades for GVF=60% for pump running at 3600 rpm with inlet GVF 13% and (a) constant bubble size 3mils (b) constant bubble size 4 mils (c) population balance model

From these three figures, bubbles of constant size are seen to aggregate near the diffuser blades and areas of low GVF are distinctly seen in PBM results. Coalescence of bubbles and their movement near the diffuser blades explains the observed low GVFs at the inner end of blades as seen in Figure 19.

Figure 20 shows the variation in water velocity in fixed bubble size model and PBM.

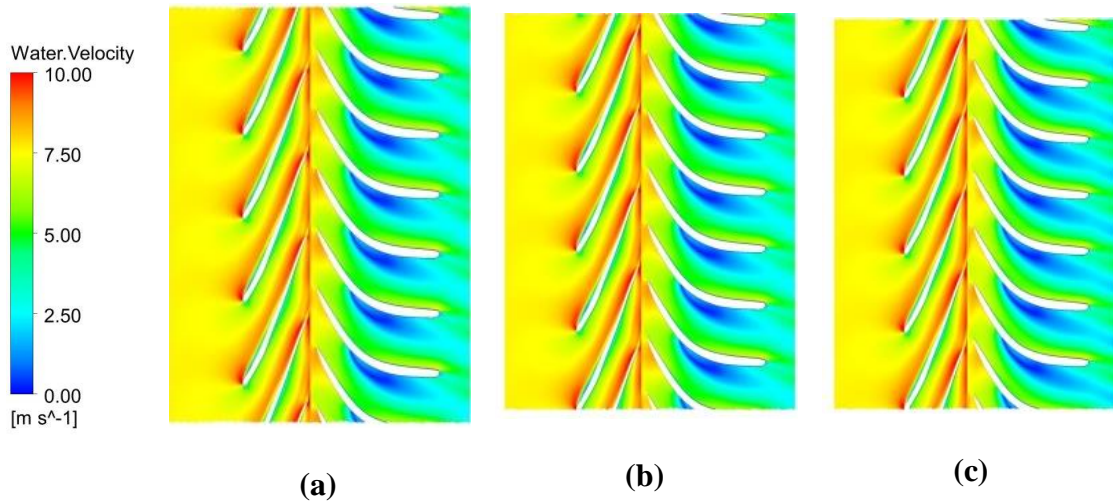


Figure 20 Water velocity distribution along impeller vanes for pump running at 3600 rpm with inlet GVF 13% and (a) constant bubble size 3mils (b) constant bubble size 4mils (c) population balance model

From the results above, it is concluded that bubbles are following the same motion in all three models. The trends of variation in parameters remain the same even after including breakage and coalescence. For higher inlet GVFs, there would be formation of larger gas pockets that would increase water velocity and decrease the pressure head. This would be captured by PBM. Hence it would show a greater degree of pressure head degradation than fixed size models and the air volume fraction and water velocity distribution would change accordingly.

Constant bubble size modeling is computationally less expensive as compared to PBM. The simulations with fixed-size bubbles take about 2 weeks to run using a dual Xeon® CPU E5-2660 v4, whereas the PBM takes approximately 3 weeks. PBM works well for flows with low GVF and high inlet pressures. At high downhole pressures, the compressibility of fluids is high and the separation between the phases does not become apparent. In highly turbulent flows, normally seen after first stage of an ESP, large bubbles

are less likely to exist as verified from experimental data. In such cases, constant bubble size modeling becomes suitable. Chen [26] compared fixed bubble size simulations with PBM for three stages of an ESP. While fixed bubble sizes did not give accurate results for the first stage, they were in good agreement with experimental data for the second and third stages. In the current cases run, the outlet pressure is held constant at 1000 psi and the bubble sizes are 3 and 4 mils, with GVFs less than or equal to 0.40. The assumption of consistent bubble size throughout the flow is justified by the high speed, and the given conditions of pressure, GVF and small bubble sizes.

PBM provides a better modeling of flows with high inlet gas volume fractions. In the first stage of a pump, pressure head degradation is severe, since this is where most of the gas pockets are formed. For such a case, PBM provides better results since it can emulate the large gas pockets. However, in PBM, the bubble sizes are not continuous and are limited to discrete values.

In summary, fixed bubble size simulations work well for flows with low inlet GVFs and high turbulence. These conditions do not lead to the formation of large gas pockets and large bubble sizes do not exist. Such circumstances are encountered in subsequent stages of an ESP. PBM on the other hand can explain gas pocket formation and ensuing pressure head loss at high GVFs. This mainly occurs in the first stage of an ESP, thus making PBM suitable for it.

5. RECOMMENDATIONS AND FUTURE WORK

The models and results in this study demonstrate the capability of CFD to be used as a reliable tool in multi-phase flow analysis through pumps. These simulations can be extended to higher gas volume fractions with varying bubble sizes. Experimental results for the exact same cases will aid in further substantiating the results. These models will provide a point of reference for studies in two-phase flow through ESPs.

6. CONCLUSIONS

A CFD analysis is performed to evaluate the performance of a single-stage electric submersible pump at two speeds, under two-phase flow conditions. Flow parameters such as pressure head and water velocity are investigated with changing air volume fractions and pump speeds. The results obtained are consistent with trends observed in previous experimental studies on centrifugal pumps.

On a broad level, effects of different parameters can be qualitatively summarized as follows:

1. A considerable reduction in actual pressure head is seen with increased bubble size and flow rate, whereas only a small variation in dimensionless head is seen. This gives a comparison of two-phase flow with single-phase flow and predicts a greater head degradation at higher speeds.
2. With the increase in mass flow rate of air bubbles, they tend to concentrate further away from the center of impeller blades. This is attributed to centrifugal force acting on them and the increased force at higher speeds.
3. Presence of a second phase accelerates the liquid flow through the pump, thus increasing the water velocity and reducing the pressure head. Presence of a significant amount of air leads to the formation of gas pockets, leading to even greater pump head degradation.

The results of constant bubble size simulations are compared with one case of Population Balance Model, which models the breakage and coalescence of bubbles. From

this comparison, it is seen that fixed bubble size model is suitable for use at low gas volume fractions. PBM gives better results for flows with high GVF and flow separation, typically encountered in the first stage of a multi-stage pump when the inlet air mass flow rate is high.

Hence, fixed-size bubble models provide a fast method of modeling multi-phase flow through pumps. These enable visualization of bubble aggregation and bubble motion trends through the impeller and diffuser. These models would be effective in predicting flows through further stages of a typical ESP. Thus, this work contributes to a database of results for the theoretical condition of bubbles of fixed size flowing through an ESP.

REFERENCES

- [1] Patil, A., Sundar, S., Delgado, A., and Gamboa, J., 2019, "CFD based evaluation of conventional electrical submersible pump for high-speed application," *Journal of Petroleum Science and Engineering*, 182, p. 106287.
- [2] Izturiz, D., and Kenyery, F., "Effect of Bubble Size on an ESP Performance Handling Two-Phase Flow Conditions," *Proc. UBS-LABCCEM*, pp. 931-939.
- [3] Murakami, M., Minemura, K., 1977, "Flow of Air Bubbles in Centrifugal Impellers and Its Effect on the Pump Performance," 6th Australasian Hydraulics and Fluid Mechanics Conference Adelaide, Australia, pp. 382-385.
- [4] Noghrehkar, G. R., Kawaji, M., Chan, A. M. C., Nakamura, H., and Kukita, Y., 1995, "Investigation of Centrifugal Pump Performance Under Two-Phase Flow Conditions," *Journal of Fluids Engineering*, 117(1), pp. 129-137.
- [5] Furuya, O., 1985, "An Analytical Model for Prediction of Two-Phase (Noncondensable) Flow Pump Performance," *Journal of Fluids Engineering*, 107(1), pp. 139-147.
- [6] Amoresano, A., Langella, G., and Noviello, C., 2001, "Experimental analysis of air bubble inside a centrifugal pump," *WIT Transactions on Modelling and Simulation*, 30, pp. 23-32.
- [7] Zhu, J., and Zhang, H., 2017, "Numerical Study on Electrical-Submersible-Pump Two-Phase Performance and Bubble-Size Modeling," *SPE Production & Operations*, 32.
- [8] Zhu, J., and Zhang, H., 2014, "CFD Simulation of ESP Performance and Bubble Size Estimation under Gassy Conditions," *SPE Annual Technical Conference and Exhibition*, Society of Petroleum Engineers, Amsterdam, The Netherlands, p. 15.
- [9] Minemura, K., Murakami, M., and Katagiri, H., 1985, "Characteristics of Centrifugal Pumps Handling Air-water Mixtures and Size of Air Bubbles in Pump Impellers," *Bulletin of JSME*, 28(244), pp. 2310-2318.
- [10] Murakami, M., and Minemura, K., 1974, "Effects of Entrained Air on the Performance of a Centrifugal Pump : 1st Report, Performance and Flow Conditions," *Bulletin of JSME*, 17(110), pp. 1047-1055.
- [11] Verde, W. M., Biazussi, J. L., Sassim, N. A., and Bannwart, A. C., 2017, "Experimental study of gas-liquid two-phase flow patterns within centrifugal pumps impellers," *Experimental Thermal and Fluid Science*, 85, pp. 37-51.

- [12] Cubas, J. M., Stel, H., Ofuchi, E. M., Neto, M. A. M., and Morales, R. E., 2019, "Visualization of two-phase gas-liquid flow in a radial centrifugal pump with a vaned diffuser," *Journal of Petroleum Science and Engineering*, p. 106848.
- [13] Poullikkas, A., 2003, "Effects of two-phase liquid-gas flow on the performance of nuclear reactor cooling pumps," *Progress in Nuclear Energy*, 42(1), pp. 3-10.
- [14] Zhang, W., Yu, Z., and Li, Y., 2018, "Application of a non-uniform bubble model in a multiphase rotodynamic pump," *Journal of Petroleum Science and Engineering*, 173.
- [15] Pineda, H., Biazussi, J., López, F., Oliveira, B., Carvalho, R. D. M., Bannwart, A. C., and Ratkovich, N., 2016, "Phase distribution analysis in an Electrical Submersible Pump (ESP) inlet handling water-air two-phase flow using Computational Fluid Dynamics (CFD)," *Journal of Petroleum Science and Engineering*, 139, pp. 49-61.
- [16] Chen, Y., 2017, "Numerical Simulation and Erosion Prediction for an Electrical Submersible Pump," Ph.D. Dissertation, Texas A&M University, College Station, TX.
- [17] Murakami, M., and Minemura, K., 1974, "Effects of Entrained Air on the Performance of Centrifugal Pumps : 2nd Report, Effects of number of blades," *Bulletin of JSME*, 17(112), pp. 1286-1295.
- [18] Zhu, J., and Zhang, H., 2018, "A Review of Experiments and Modeling of Gas-Liquid Flow in Electrical Submersible Pumps," *Energies*, 11, p. 180.
- [19] Estevam, V., 2002, "A Phenomenological Analysis about centrifugal pump in two-phase flow operation," Ph.D. Dissertation, Universidade Estadual de Campinas, Campinas, Brazil.
- [20] Barrios, L. J., 2007, "Visualization and modeling of multiphase performance inside an electrical submersible pump," Ph.D. Dissertation, The University of Tulsa, Tulsa, OK.
- [21] Gamboa, J., 2008, "Prediction of the transition in two-phase performance of an electrical submersible pump," Ph.D. Dissertation, The University of Tulsa, Tulsa, OK.
- [22] Marsis, E., Pirouzpanah, S., and Morrison, G., "CFD-based design improvement for single-phase and two-phase flows inside an electrical submersible pump," *Proc. ASME 2013 Fluids Engineering Division Summer Meeting, FEDSM 2013*, July 7, 2013 - July 11, 2013, American Society of Mechanical Engineers (ASME), p. Fluids Engineering Division.
- [23] ANSYS Documentation, "Fluent Theory Guide, Multiphase Flows, Eulerian Model Theory," Release 17.2.

[24] Shi, Y., Zhu, H., Zhang, J., Zhang, J., and Zhao, J., 2018, "Experiment and numerical study of a new generation three-stage multiphase pump," *Journal of Petroleum Science and Engineering*, 169, pp. 471-484.

[25] Patil, A., Sundar, S., Delgado, A., and Gamboa, J., 2019, "CFD based evaluation of conventional electrical submersible pump for high-speed application," *Journal of Petroleum Science and Engineering*, 182.

[26] Chen, Y., Patil, A., Chen, Y., Bai, C., Wang, Y., and Morrison, G., 2019, "Numerical Study on the First Stage Head Degradation in an Electrical Submersible Pump with Population Balance Model," *Journal of Energy Resources Technology, Transactions of the ASME*, 141(2).

APPENDIX A

PRESSURE HEAD DEGRADATION AS A FUNCTION OF GVF AND BUBBLE
SIZE

Table A1 lists the actual values of pressure heads measured from simulations for increasing GVFs. The reference pressure for calculating dimensionless pressure head is 0.12 MPa (17.8 psi) corresponding to single-phase flow at 3600 rpm.

Table A1 Pressure head values at increasing GVF for pump running at 3600 rpm

Mass flow rate of water kg/s	Mass flow rate of air kg/s	GVF	Pressure head		
			MPa (psi)		
			Bubble sizes		
			63.5 μm (2.5 mils)	76.2 μm (3 mils)	101.6 μm (4 mils)
5	0.05	0.13	0.1006 (14.60)	0.1003 (14.55)	0.0992 (14.39)
5	0.07	0.19	0.0946 (13.72)	0.0943 (13.68)	0.0898 (13.02)
5	0.09	0.24	0.0884 (12.82)	0.0880 (12.77)	0.0848 (12.30)
5	0.11	0.29	0.0826 (11.98)	0.0816 (11.84)	0.0800 (11.61)
5	0.13	0.35	0.0765	0.0758	0.0737

			(11.10)	(10.99)	(10.69)
5	0.15	0.40	0.0764	0.0720	0.0709
			(11.08)	(10.45)	(10.28)

Similarly, table A2 shows the actual pressure head values for pump at 6000 rpm. For finding the dimensionless pressure head, the reference value is 0.3507 MPa (50.86 psi) corresponding to single-phase flow at 6000 rpm.

Table A2 Pressure head values at increasing GVF for pump running at 6000 rpm

Mass flow rate of water kg/s	Mass flow rate of air kg/s	GVF	Pressure head		
			MPa (psi)		
			Bubble sizes		
			63.5 μm (2.5 mils)	76.2 μm (3 mils)	101.6 μm (4 mils)
8	0.08	0.13	0.2805 (40.69)	0.2699 (39.14)	0.2616 (37.95)
8	0.11	0.18	0.2534 (36.76)	0.2505 (36.34)	0.2415 (35.03)
8	0.15	0.25	0.2447 (35.49)	0.2330 (33.80)	0.2221 (32.22)
8	0.18	0.30	0.2287 (33.17)	0.2237 (32.44)	0.2128 (30.86)
8	0.21	0.35	0.2116	0.2057	0.1944

(30.69)

(29.83)

(28.20)

APPENDIX B

AIR VOLUME FRACTION DISTRIBUTION AT 3600 RPM

Inlet mass flow rates for air are calculated as shown below. Note here that the density of air is taken as 75 kg/m^3 which is corresponding to the outlet pressure of 6.89 MPa (1000 psi) and an assumed temperature of $54.44 \text{ }^\circ\text{C}$ ($130 \text{ }^\circ\text{F}$). Density of water is assumed 1000 kg/m^3 . From affinity laws, the mass flow rate of water is 5 kg/s at 3600 rpm.

$$\dot{m}_{air} = \rho_{air} \dot{V}_{air}$$

$$\dot{m}_{air} = \rho_{air} (\dot{V}_{water} * GVF)$$

$$\dot{m}_{air} = \rho_{air} \left(\frac{\dot{m}_{water}}{\rho_{water}} * GVF \right)$$

Table B1 Calculation of air mass flow rates from GVF for pump speed 3600 rpm

Mass flow rate of water kg/s	GVF	Mass flow rate of air kg/s
5	0.13	0.05
5	0.19	0.07
5	0.24	0.09
5	0.29	0.11
5	0.35	0.13
5	0.40	0.15

Figures B1 to B6 depict the variation of air volume fraction along a blade to blade surface for increasing GVFs and increasing bubble sizes for a pump speed of 3600 rpm.

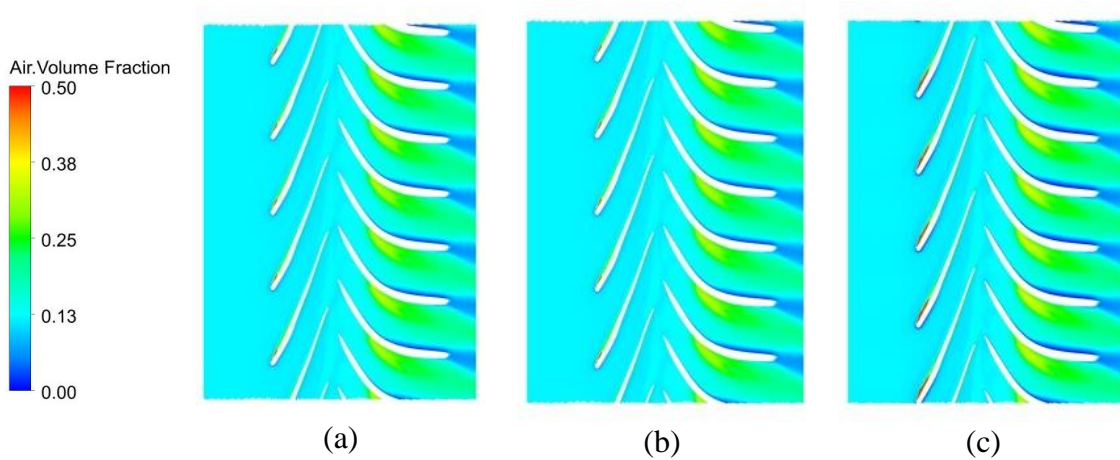


Figure B1 Air volume fraction along blade to blade surface for pump running at 3600 rpm with inlet GVF 13% and bubble sizes (a) 63.5 μm (2.5 mils) (b) 76.2 μm (3 mils) and (c) 101.6 μm (4 mils)

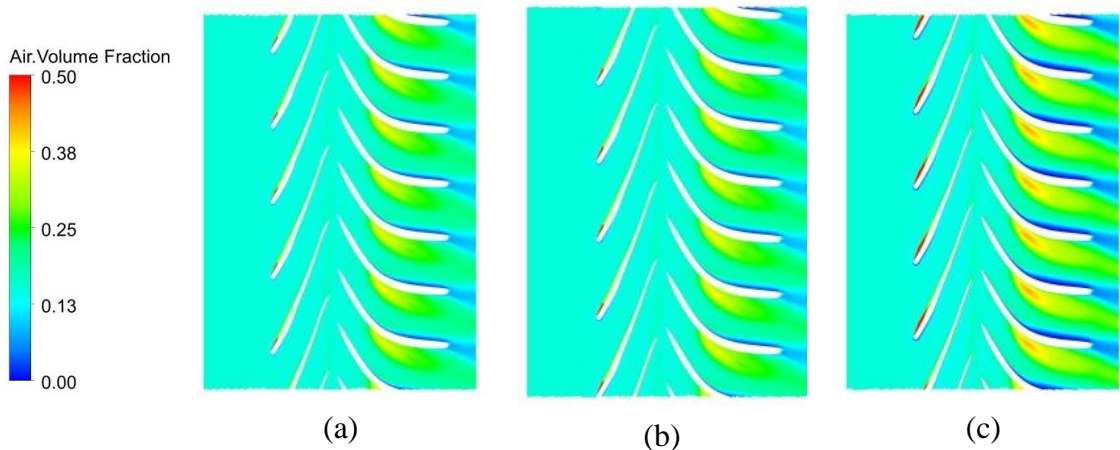


Figure B2 Air volume fraction along blade to blade surface for pump running at 3600 rpm with inlet GVF 19% and bubble sizes (a) 63.5 μm (2.5 mils) (b) 76.2 μm (3 mils) and (c) 101.6 μm (4 mils)

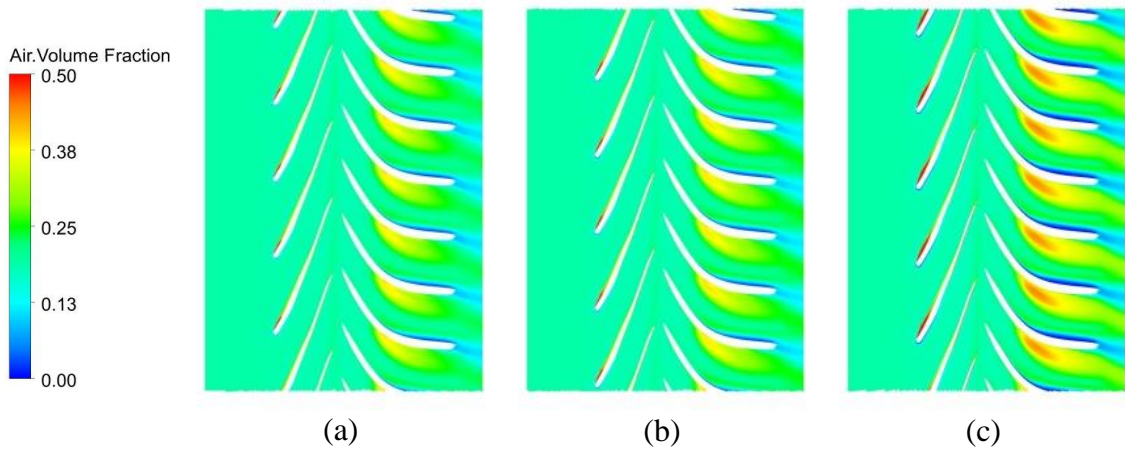


Figure B3 Air volume fraction along blade to blade surface for pump running at 3600 rpm with inlet GVF 24% and bubble sizes (a) 63.5 μm (2.5 mils) (b) 76.2 μm (3 mils) and (c) 101.6 μm (4 mils)

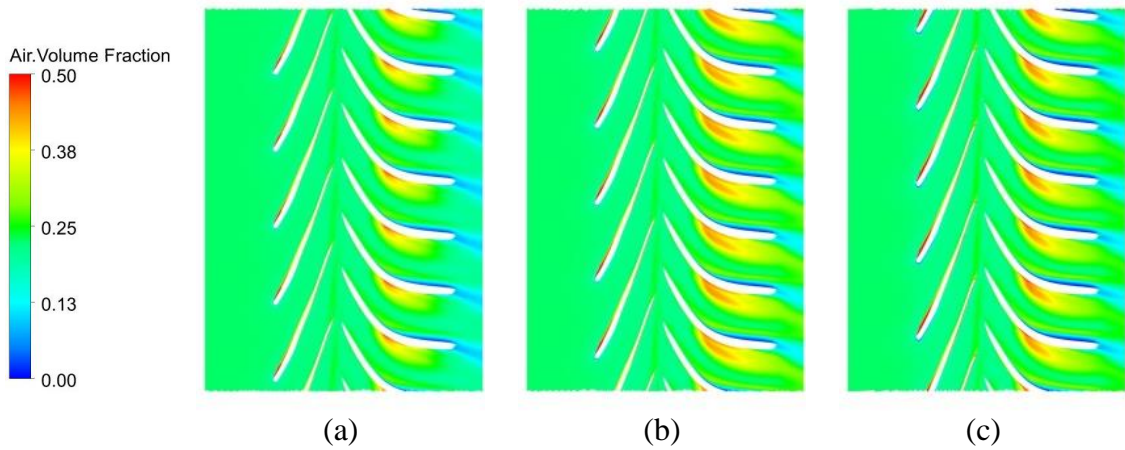


Figure B4 Air volume fraction along blade to blade surface for pump running at 3600 rpm with inlet GVF 29% and bubble sizes (a) 63.5 μm (2.5 mils) (b) 76.2 μm (3 mils) and (c) 101.6 μm (4 mils)

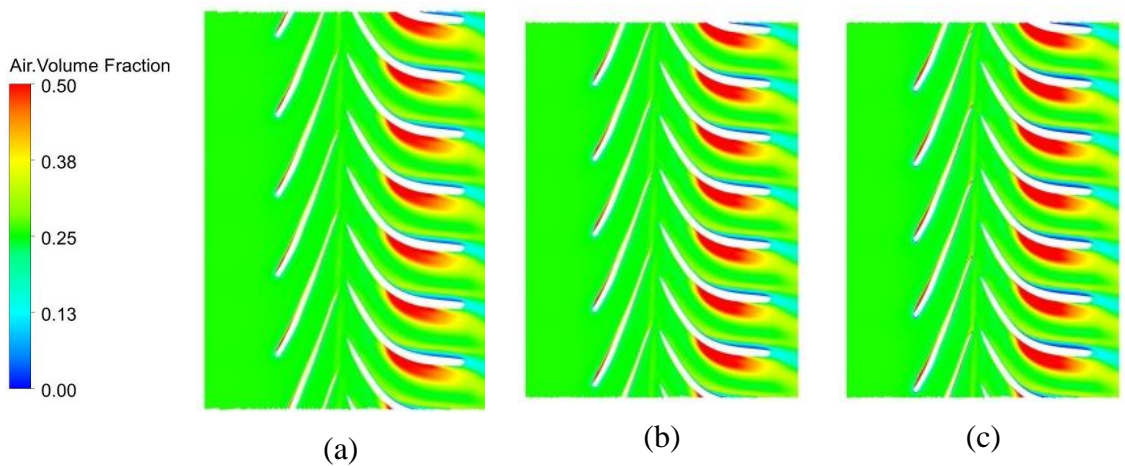


Figure B5 Air volume fraction along blade to blade surface for pump running at 3600 rpm with inlet GVF 35% and bubble sizes (a) 63.5 μm (2.5 mils) (b) 76.2 μm (3 mils) and (c) 101.6 μm (4 mils)

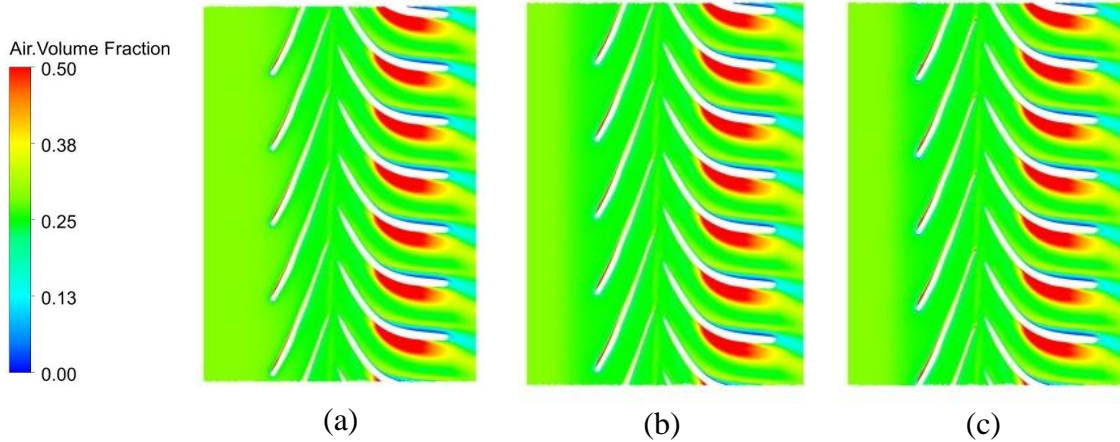


Figure B6 Air volume fraction along blade to blade surface for pump running at 3600 rpm with inlet GVF 40% and bubble sizes (a) 63.5 μm (2.5 mils) (b) 76.2 μm (3 mils) and (c) 101.6 μm (4 mils)

Figures B7 to B12 show the variation of air volume fraction along impeller vanes for a pump speed 3600 rpm with increasing GVFs and bubble sizes.

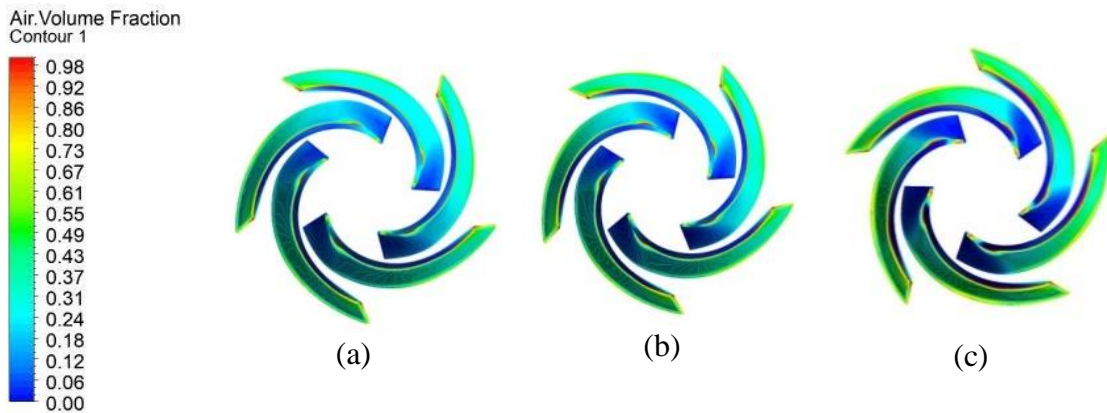
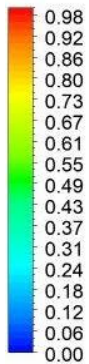


Figure B7 Air volume fraction along impeller vanes for pump running at 3600 rpm with inlet GVF 13% and bubble sizes (a) 63.5 μm (2.5 mils) (b) 76.2 μm (3 mils) and (c) 101.6 μm (4 mils)

Air Volume Fraction
Contour 1



(a)



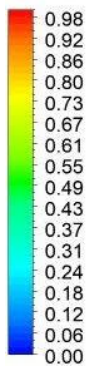
(b)



(c)

Figure B8 Air volume fraction along blade to blade surface for pump running at 3600 rpm with inlet GVF 19% and bubble sizes (a) 63.5 μm (2.5 mils) (b) 76.2 μm (3 mils) and (c) 101.6 μm (4 mils)

Air Volume Fraction
Contour 1



(a)



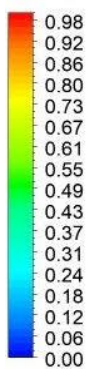
(b)



(c)

Figure B9 Air volume fraction along blade to blade surface for pump running at 3600 rpm with inlet GVF 24% and bubble sizes (a) 63.5 μm (2.5 mils) (b) 76.2 μm (3 mils) and (c) 101.6 μm (4 mils)

Air Volume Fraction
Contour 1



(a)



(b)



(c)

Figure B10 Air volume fraction along blade to blade surface for pump running at 3600 rpm with inlet GVF 29% and bubble sizes (a) 63.5 μm (2.5 mils) (b) 76.2 μm (3 mils) and (c) 101.6 μm (4 mils)

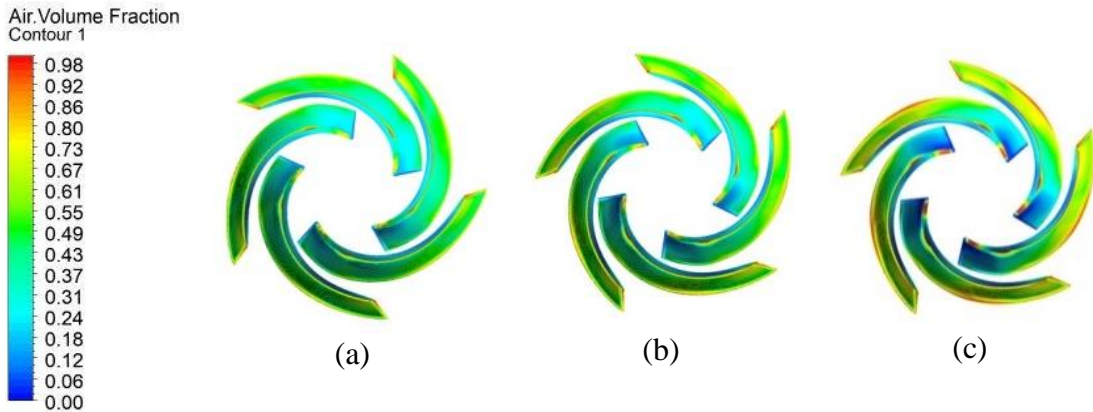


Figure B11 Air volume fraction along blade to blade surface for pump running at 3600 rpm with inlet GVF 35% and bubble sizes (a) 63.5 μm (2.5 mils) (b) 76.2 μm (3 mils) and (c) 101.6 μm (4 mils)

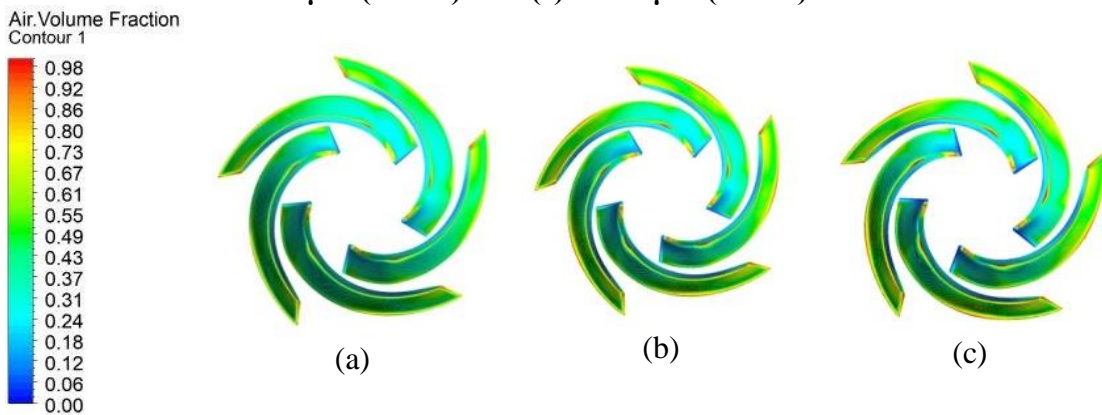


Figure B12 Air volume fraction along blade to blade surface for pump running at 3600 rpm with inlet GVF 40% and bubble sizes (a) 63.5 μm (2.5 mils) (b) 76.2 μm (3 mils) and (c) 101.6 μm (4 mils)

Figures B13 to B18 depict an iso-surface of 60% GVF on the impeller vanes. The blue areas are surfaces of the impeller and the green surface represents areas where 60% of the total volume is occupied by air.

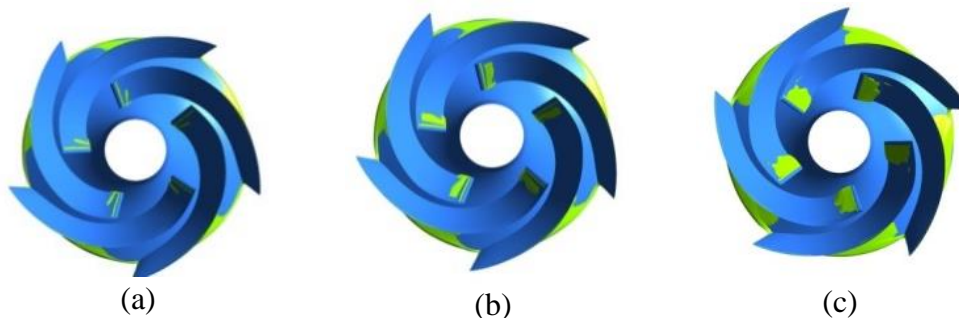


Figure B13 Iso-surface on impeller blades for GVF=60% for pump running at 3600 rpm with inlet GVF 13% and bubble sizes (a) 63.5 μm (2.5 mils) (b) 76.2 μm (3 mils) and (c) 101.6 μm (4 mils)

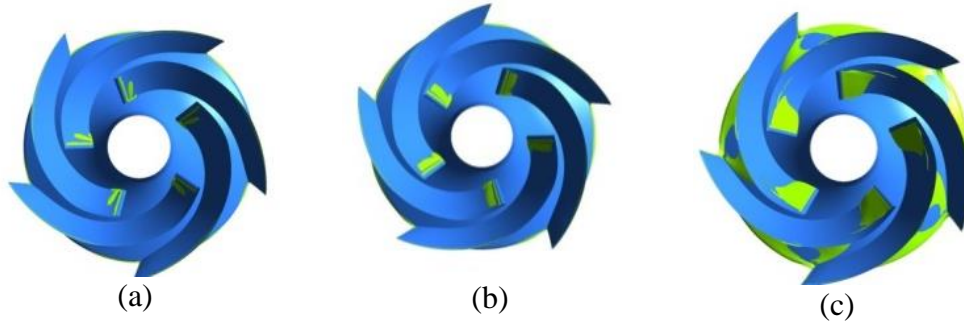


Figure B14 Iso-surface on impeller blades for GVF=60% for pump running at 3600 rpm with inlet GVF 19% and bubble sizes (a) 63.5 μm (2.5 mils) (b) 76.2 μm (3 mils) and (c) 101.6 μm (4 mils)

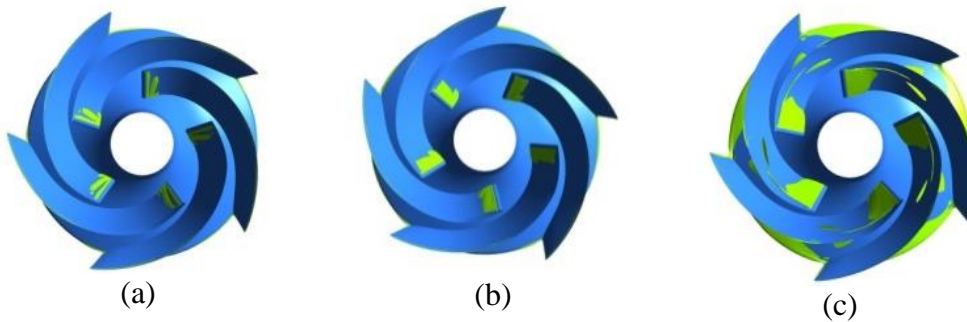


Figure B15 Iso-surface on impeller blades for GVF=60% for pump running at 3600 rpm with inlet GVF 24% and bubble sizes (a) 63.5 μm (2.5 mils) (b) 76.2 μm (3 mils) and (c) 101.6 μm (4 mils)

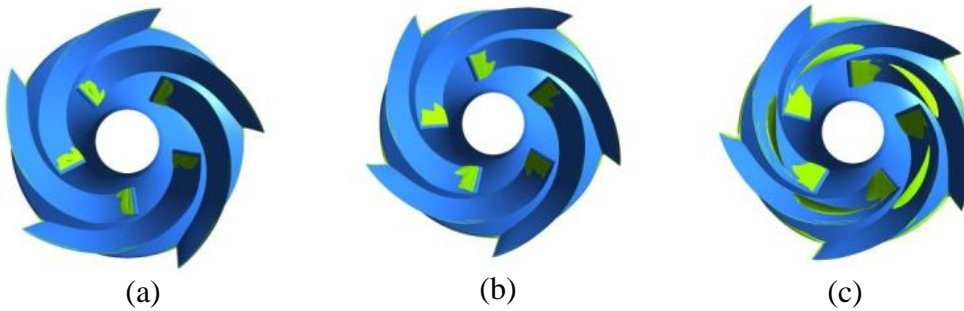


Figure B16 Iso-surface on impeller blades for GVF=60% for pump running at 3600 rpm with inlet GVF 29% and bubble sizes (a) 63.5 μm (2.5 mils) (b) 76.2 μm (3 mils) and (c) 101.6 μm (4 mils)

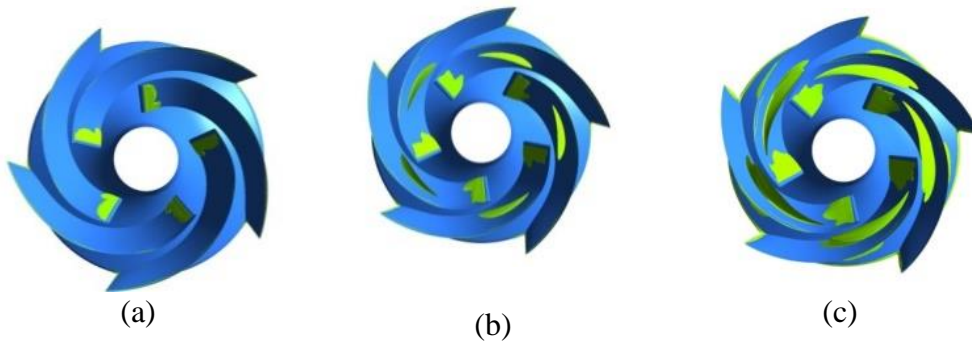


Figure B17 Iso-surface on impeller blades for GVF=60% for pump running at 3600 rpm with inlet GVF 35% and bubble sizes (a) 63.5 μm (2.5 mils) (b) 76.2 μm (3 mils) and (c) 101.6 μm (4 mils)

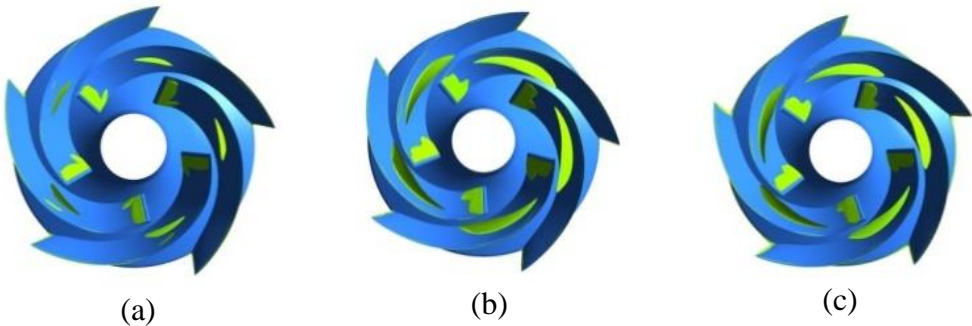


Figure B18 Iso-surface on impeller blades for GVF=60% for pump running at 3600 rpm with inlet GVF 40% and bubble sizes (a) 63.5 μm (2.5 mils) (b) 76.2 μm (3 mils) and (c) 101.6 μm (4 mils)

Figures B19 to B24 show the air volume fraction along a meridional plane for pump speed 3600 rpm with increasing GVFs and increasing bubble sizes.

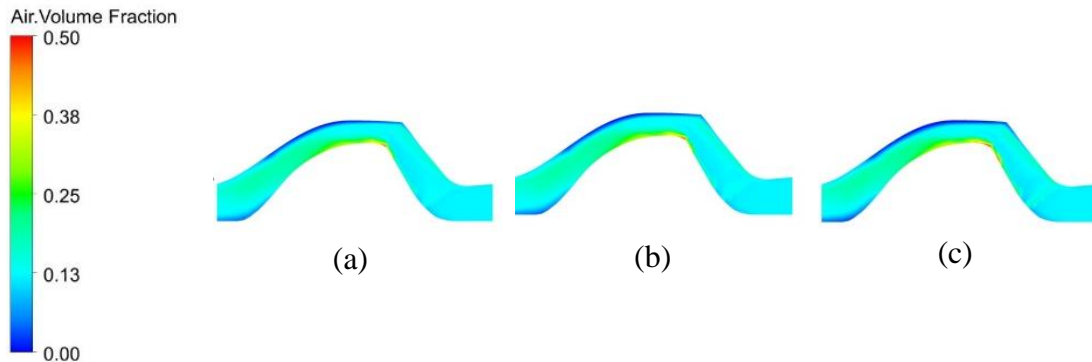


Figure B19 Air volume fraction along meridional surface for pump running at 3600 rpm with inlet GVF 13% and bubble sizes (a) 63.5 μm (2.5 mils) (b) 76.2 μm (3 mils) and (c) 101.6 μm (4 mils)

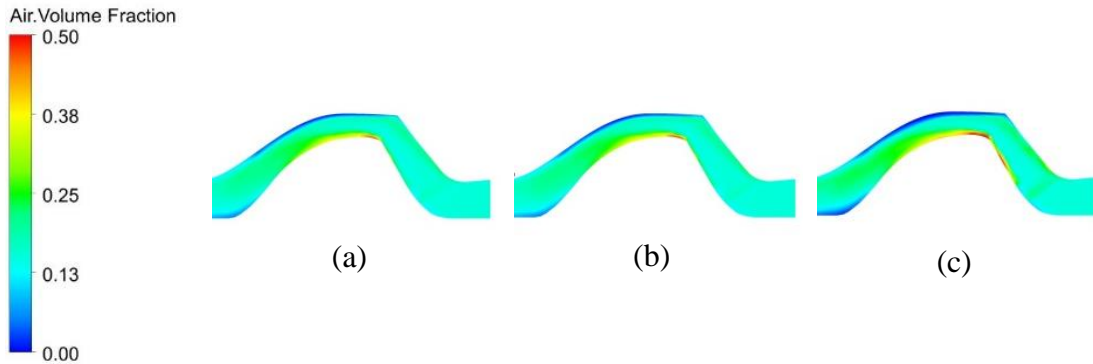


Figure B20 Air volume fraction along meridional surface for pump running at 3600 rpm with inlet GVF 19% and bubble sizes (a) 63.5 μm (2.5 mils) (b) 76.2 μm (3 mils) and (c) 101.6 μm (4 mils)

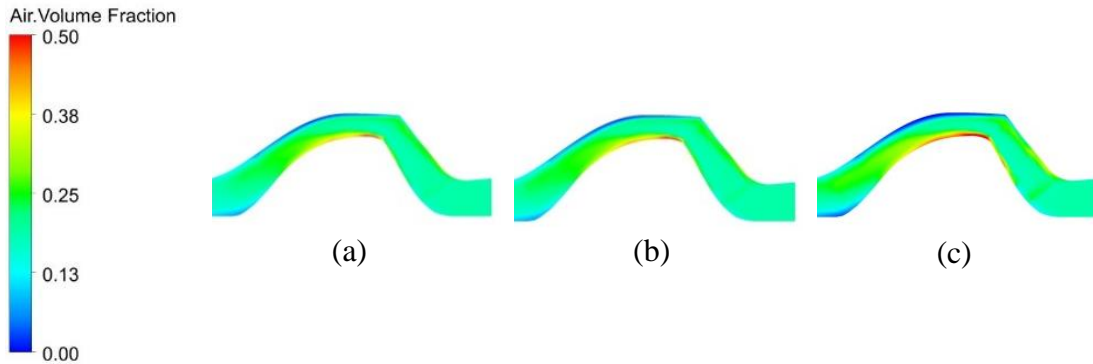


Figure B21 Air volume fraction along meridional surface for pump running at 3600 rpm with inlet GVF 24% and bubble sizes (a) 63.5 μm (2.5 mils) (b) 76.2 μm (3 mils) and (c) 101.6 μm (4 mils)

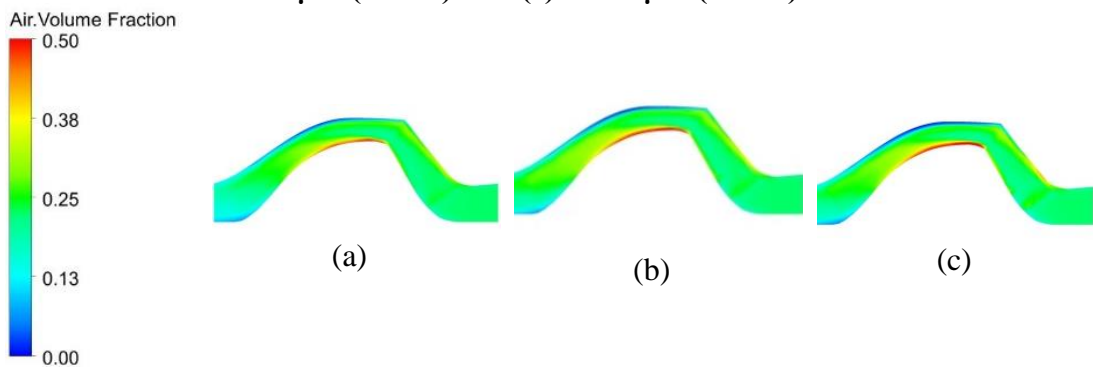


Figure B22 Air volume fraction along meridional surface for pump running at 3600 rpm with inlet GVF 29% and bubble sizes (a) 63.5 μm (2.5 mils) (b) 76.2 μm (3 mils) and (c) 101.6 μm (4 mils)

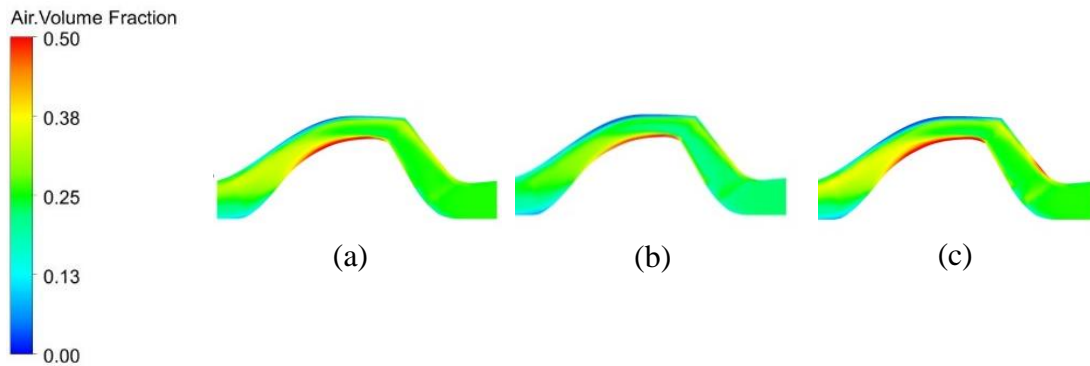


Figure B23 Air volume fraction along meridional surface for pump running at 3600 rpm with inlet GVF 35% and bubble sizes (a) 63.5 μm (2.5 mils) (b) 76.2 μm (3 mils) and (c) 101.6 μm (4 mils)

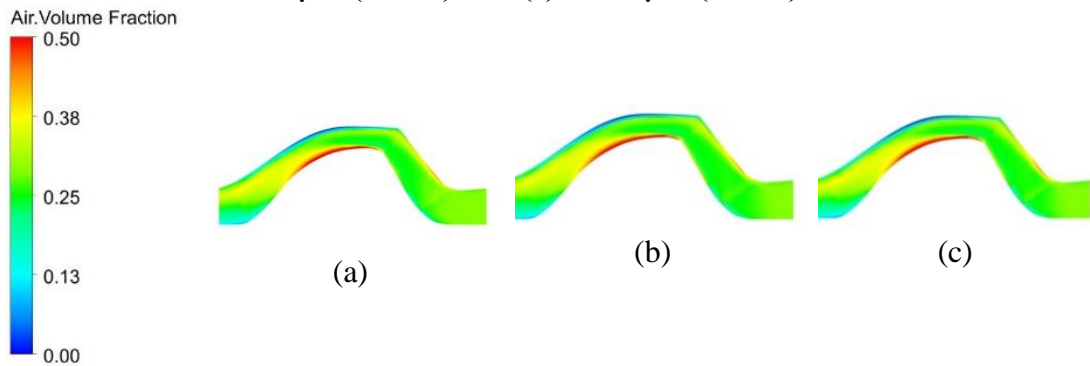


Figure B24 Air volume fraction along meridional surface for pump running at 3600 rpm with inlet GVF 40% and bubble sizes (a) 63.5 μm (2.5 mils) (b) 76.2 μm (3 mils) and (c) 101.6 μm (4 mils)

APPENDIX C

AIR VOLUME FRACTION DISTRIBUTION AT 6000 RPM

Like 3600 rpm, inlet mass flow rates for air are calculated for 6000 rpm using the equations in Appendix B.

Table C1 Calculation of air mass flow rates from GVF for pump speed 6000 rpm

Mass flow rate of water kg/s	GVF	Mass flow rate of air kg/s
8	0.13	0.08
8	0.18	0.11
8	0.25	0.15
8	0.30	0.18
8	0.35	0.21

Figures C1 to C5 show the air volume fraction along a blade to blade surface for pump running at 6000 rpm, with increasing GVFs and bubble sizes.

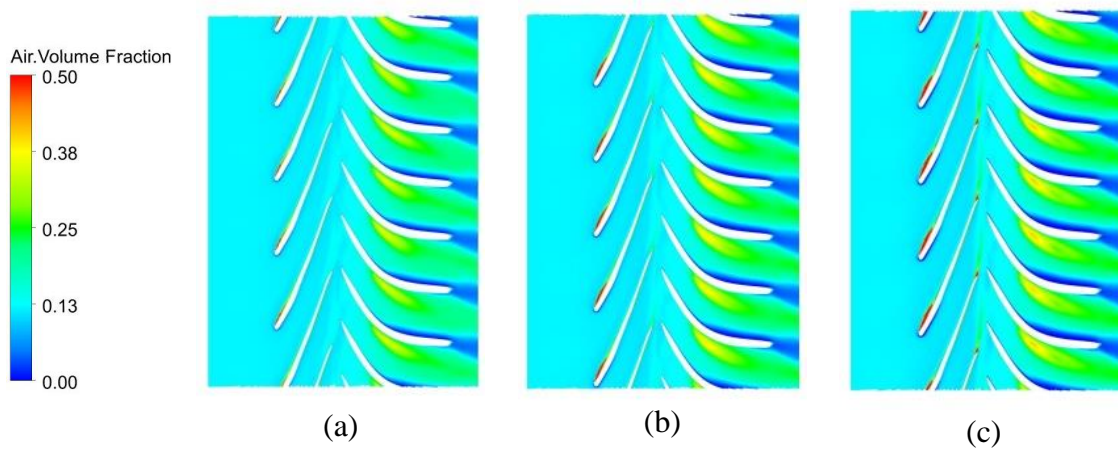


Figure C1 Air volume fraction along blade to blade surface for pump running at 6000 rpm with inlet GVF 13% and bubble sizes (a) 63.5 μm (2.5 mils) (b) 76.2 μm (3 mils) and (c) 101.6 μm (4 mils)

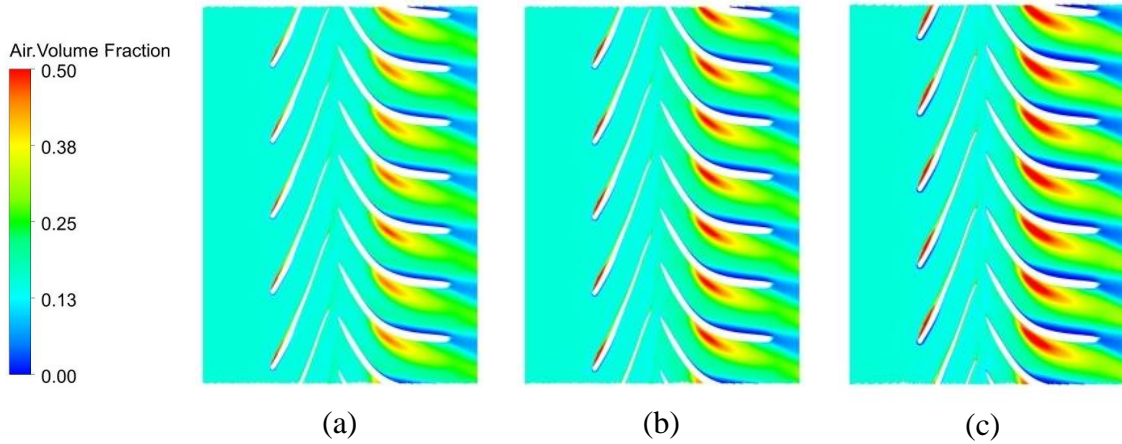


Figure C2 Air volume fraction along blade to blade surface for pump running at 6000 rpm with inlet GVF 18% and bubble sizes (a) 63.5 μm (2.5 mils) (b) 76.2 μm (3 mils) and (c) 101.6 μm (4 mils)

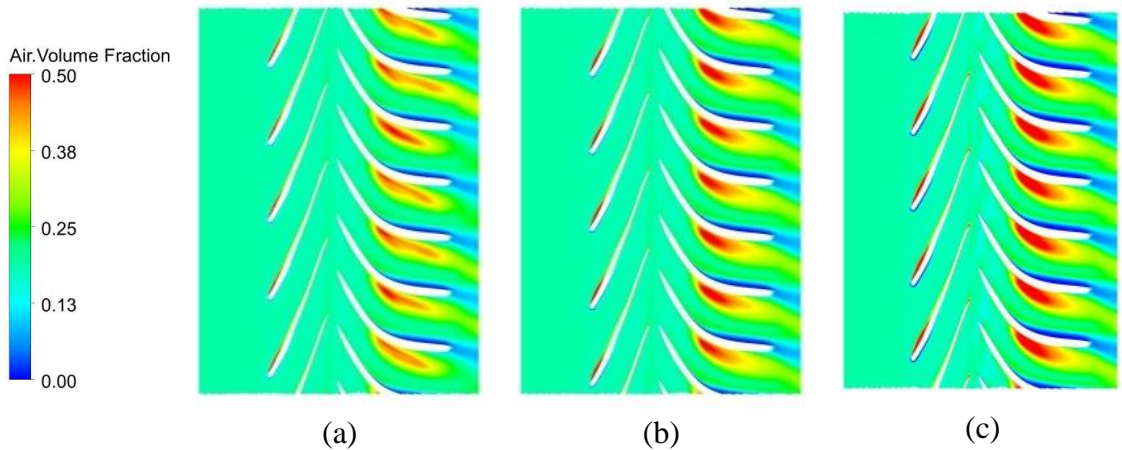


Figure C3 Air volume fraction along blade to blade surface for pump running at 6000 rpm with inlet GVF 25% and bubble sizes (a) 63.5 μm (2.5 mils) (b) 76.2 μm (3 mils) and (c) 101.6 μm (4 mils)

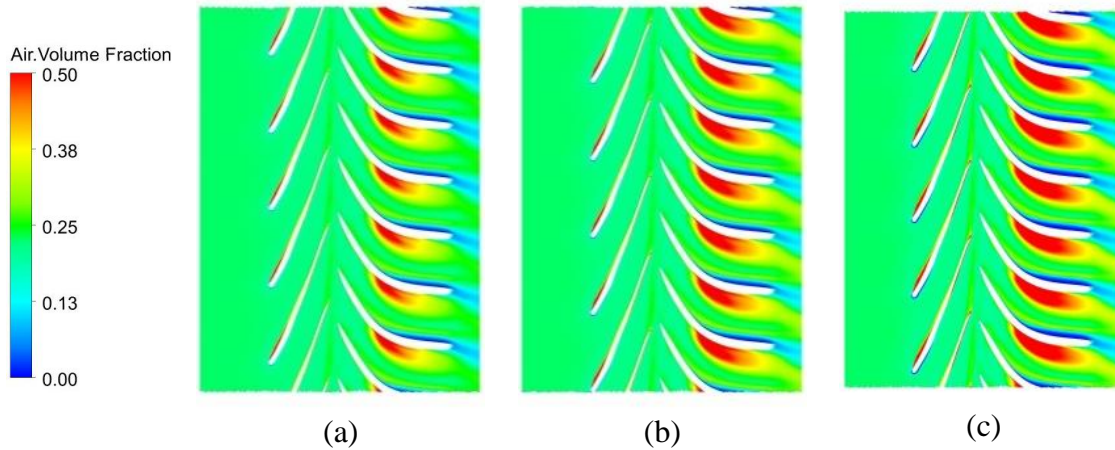


Figure C4 Air volume fraction along blade to blade surface for pump running at 6000 rpm with inlet GVF 30% and bubble sizes (a) 63.5 μm (2.5 mils) (b) 76.2 μm (3 mils) and (c) 101.6 μm (4 mils)

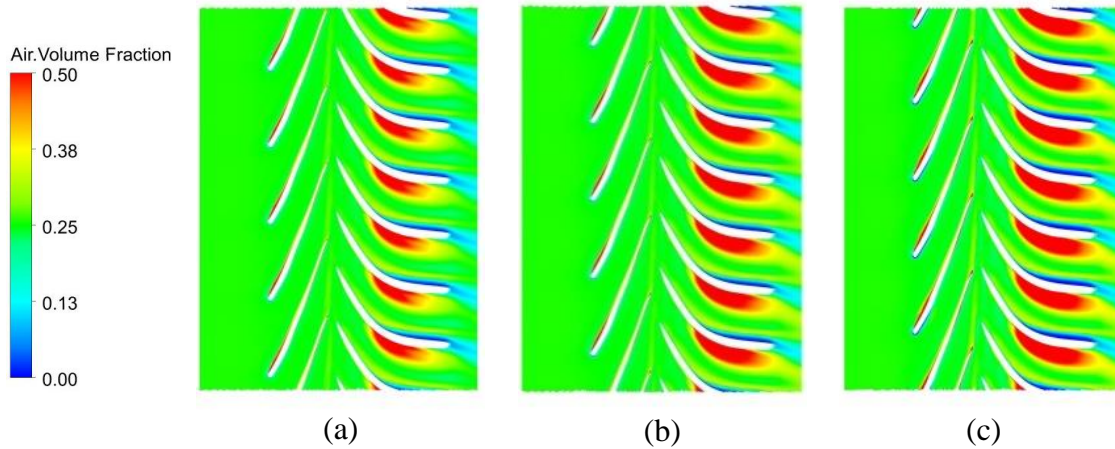


Figure C5 Air volume fraction along blade to blade surface for pump running at 6000 rpm with inlet GVF 35% and bubble sizes (a) 63.5 μm (2.5 mils) (b) 76.2 μm (3 mils) and (c) 101.6 μm (4 mils)

Figures C6 to C10 show the air volume fraction distribution along the impeller vanes for pump running at 6000 rpm with increasing GVFs and bubble sizes.

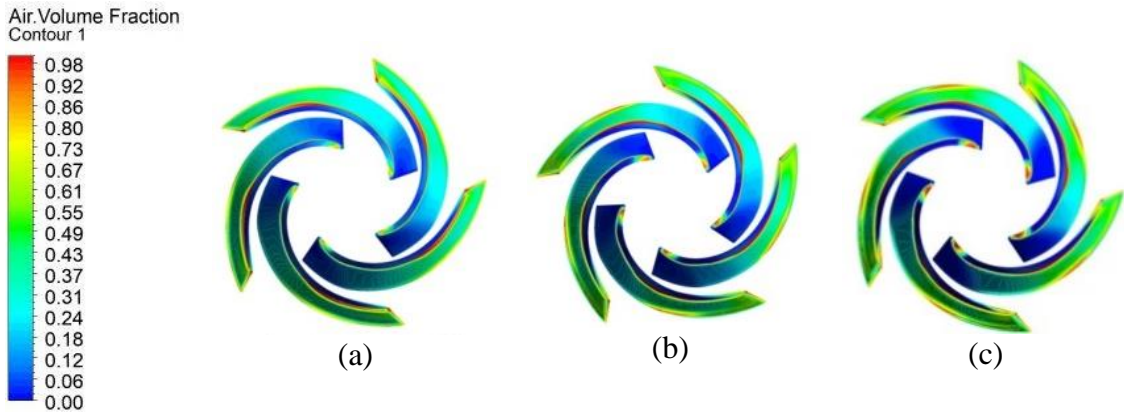


Figure C6 Air volume fraction along impeller vanes for pump running at 6000 rpm with inlet GVF 13% and bubble sizes (a) 63.5 μm (2.5 mils) (b) 76.2 μm (3 mils) and (c) 101.6 μm (4 mils)

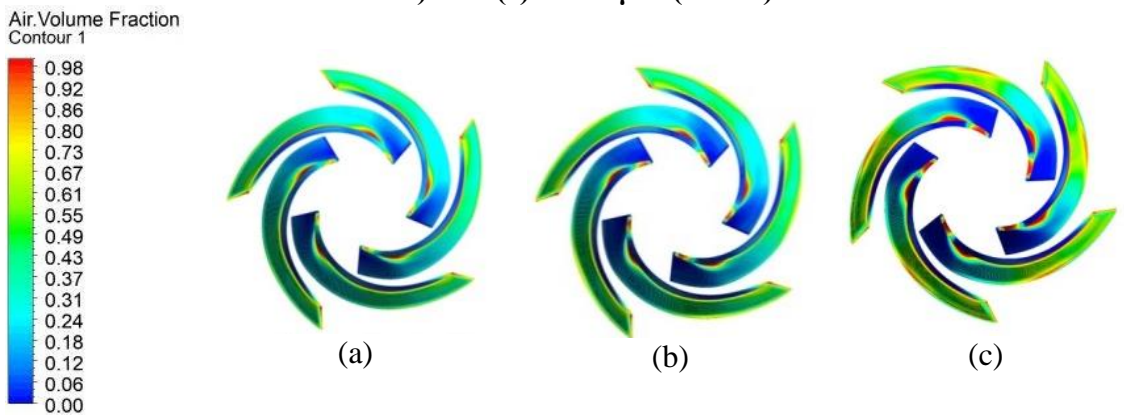


Figure C7 Air volume fraction along impeller vanes for pump running at 6000 rpm with inlet GVF 13% and bubble sizes (a) 63.5 μm (2.5 mils) (b) 76.2 μm (3 mils) and (c) 101.6 μm (4 mils)

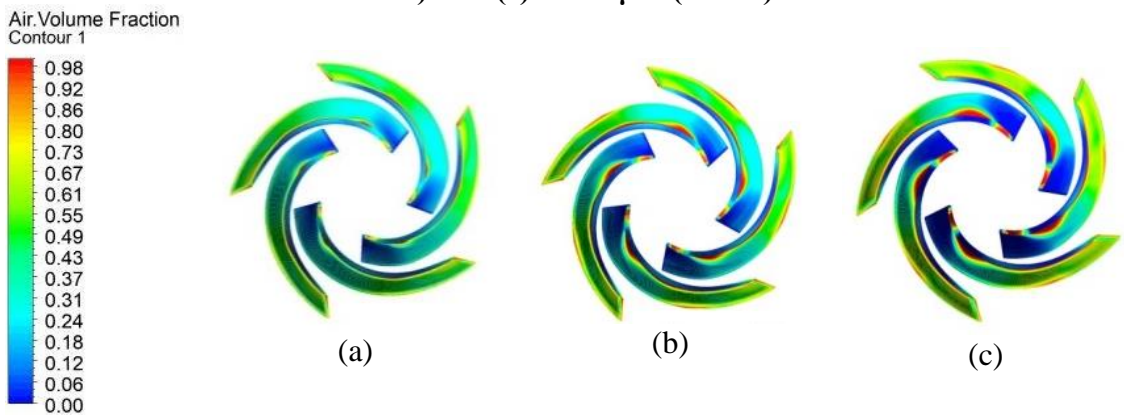


Figure C8 Air volume fraction along impeller vanes for pump running at 6000 rpm with inlet GVF 13% and bubble sizes (a) 63.5 μm (2.5 mils) (b) 76.2 μm (3 mils) and (c) 101.6 μm (4 mils)

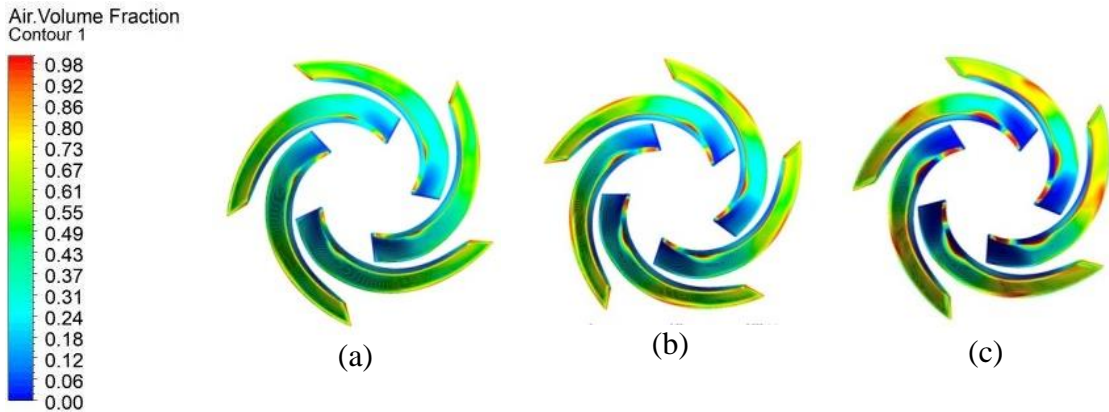


Figure C9 Air volume fraction along impeller vanes for pump running at 6000 rpm with inlet GVF 13% and bubble sizes (a) 63.5 μm (2.5 mils) (b) 76.2 μm (3 mils) and (c) 101.6 μm (4 mils)

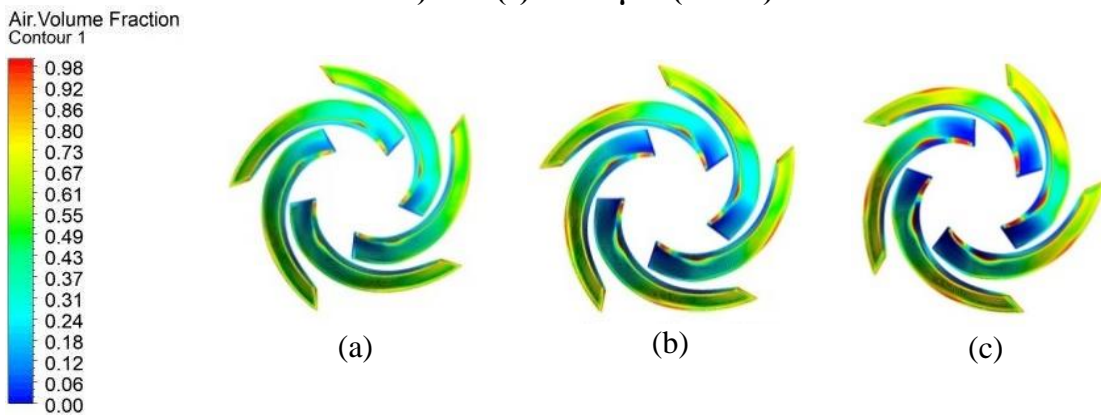


Figure C10 Air volume fraction along impeller vanes for pump running at 6000 rpm with inlet GVF 13% and bubble sizes (a) 63.5 μm (2.5 mils) (b) 76.2 μm (3 mils) and (c) 101.6 μm (4 mils)

Figures C11 to C15 show an iso-surface of constant GVF 0.6 along impeller vanes for pump speed 6000 rpm with increasing bubble sizes and increasing inlet GVFs.

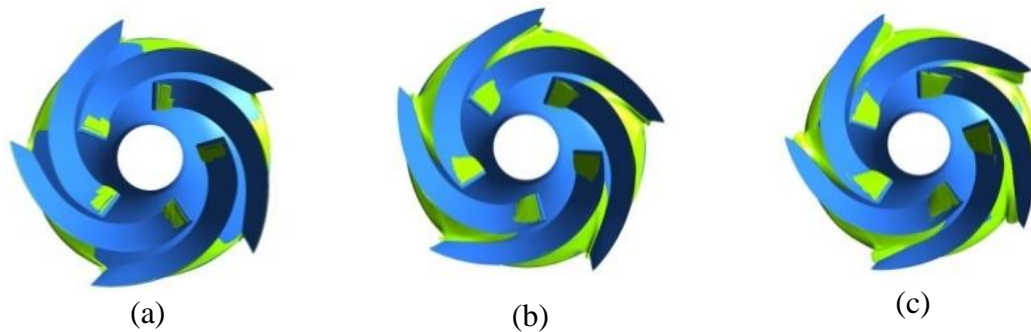


Figure C11 Iso-surface on impeller blades for GVF=60% for pump running at 6000 rpm with inlet GVF 13% and bubble sizes (a) 63.5 μm (2.5 mils) (b) 76.2 μm (3 mils) and (c) 101.6 μm (4 mils)

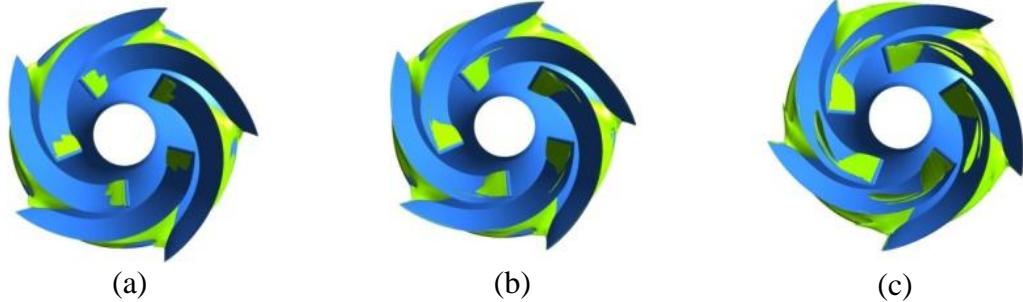


Figure C12 Iso-surface on impeller blades for GVF=60% for pump running at 6000 rpm with inlet GVF 18% and bubble sizes (a) 63.5 μm (2.5 mils) (b) 76.2 μm (3 mils) and (c) 101.6 μm (4 mils)

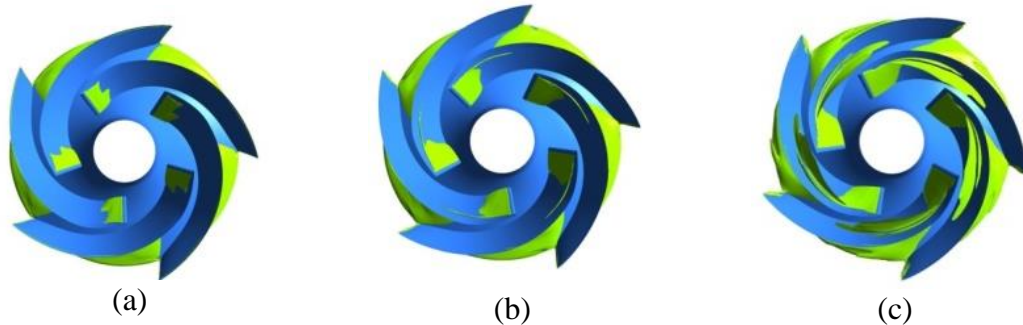


Figure C13 Iso-surface on impeller blades for GVF=60% for pump running at 6000 rpm with inlet GVF 25% and bubble sizes (a) 63.5 μm (2.5 mils) (b) 76.2 μm (3 mils) and (c) 101.6 μm (4 mils)

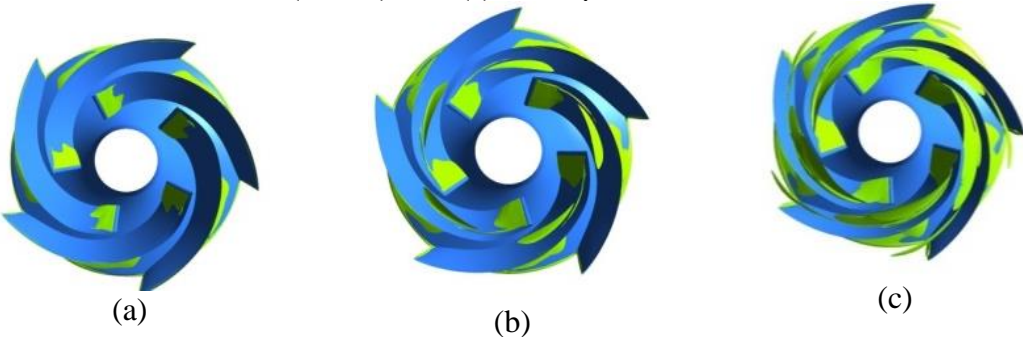


Figure C14 Iso-surface on impeller blades for GVF=60% for pump running at 6000 rpm with inlet GVF 30% and bubble sizes (a) 63.5 μm (2.5 mils) (b) 76.2 μm (3 mils) and (c) 101.6 μm (4 mils)

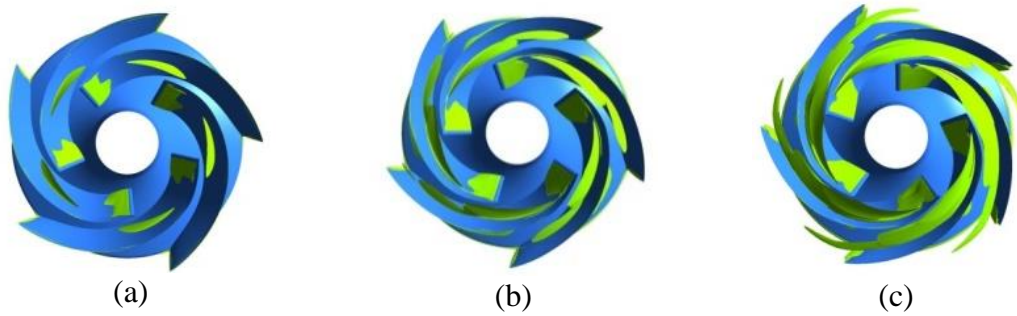


Figure C15 Iso-surface on impeller blades for GVF=60% for pump running at 6000 rpm with inlet GVF 35% and bubble sizes (a) 63.5 μm (2.5 mils) (b) 76.2 μm (3 mils) and (c) 101.6 μm (4 mils)

Figures C16 to C20 show the meridional variation of air volume fraction for pump speed 6000 rpm with increasing inlet GVFs and bubble sizes.

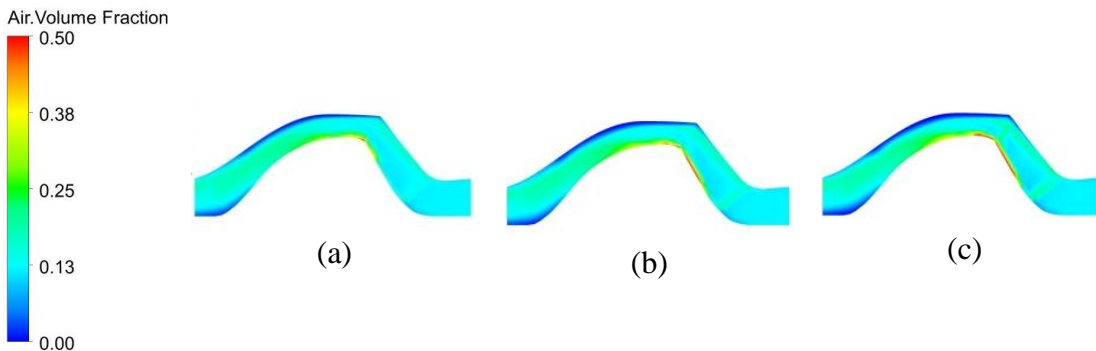


Figure C16 Air volume fraction along meridional surface for pump running at 6000 rpm with inlet GVF 13% and bubble sizes (a) 63.5 μm (2.5 mils) (b) 76.2 μm (3 mils) and (c) 101.6 μm (4 mils)

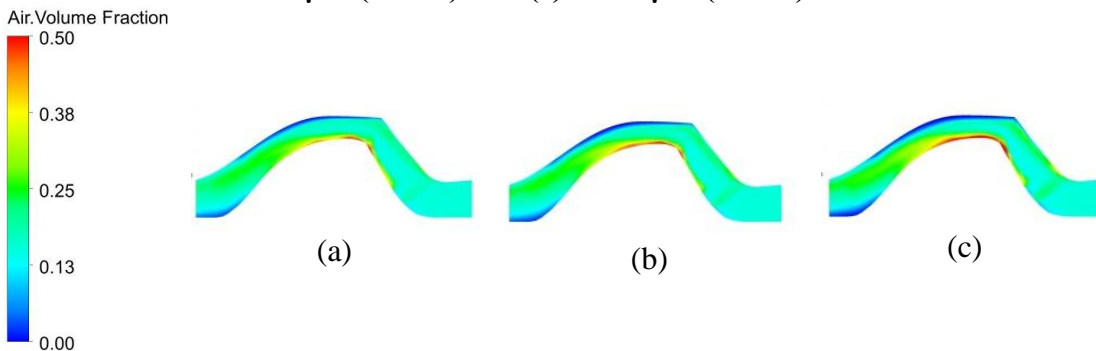


Figure C17 Air volume fraction along meridional surface for pump running at 6000 rpm with inlet GVF 18% and bubble sizes (a) 63.5 μm (2.5 mils) (b) 76.2 μm (3 mils) and (c) 101.6 μm (4 mils)

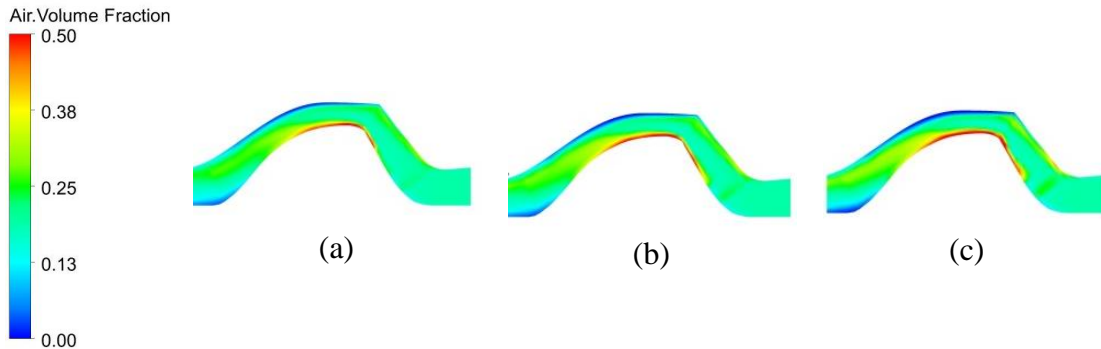


Figure C18 Air volume fraction along meridional surface for pump running at 6000 rpm with inlet GVF 25% and bubble sizes (a) 63.5 μm (2.5 mils) (b) 76.2 μm (3 mils) and (c) 101.6 μm (4 mils)

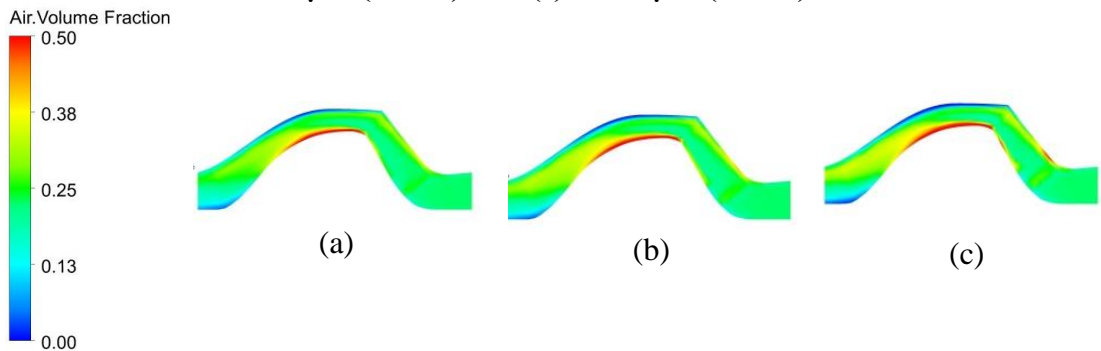


Figure C19 Air volume fraction along meridional surface for pump running at 6000 rpm with inlet GVF 30% and bubble sizes (a) 63.5 μm (2.5 mils) (b) 76.2 μm (3 mils) and (c) 101.6 μm (4 mils)

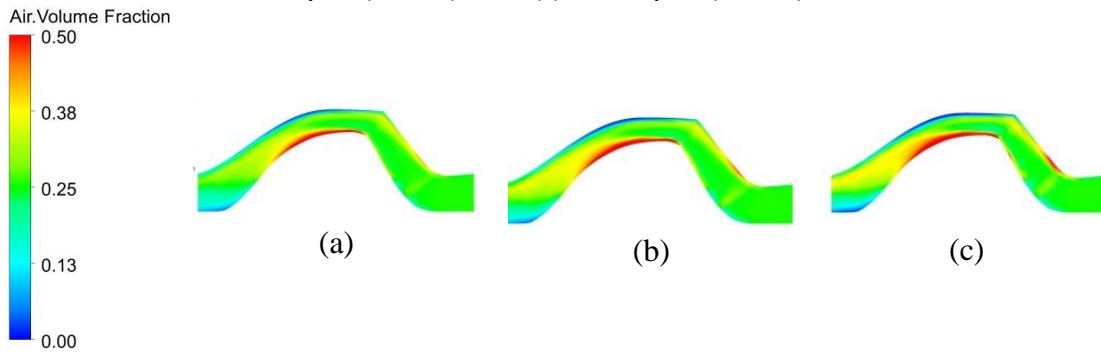


Figure C20 Air volume fraction along meridional surface for pump running at 6000 rpm with inlet GVF 35% and bubble sizes (a) 63.5 μm (2.5 mils) (b) 76.2 μm (3 mils) and (c) 101.6 μm (4 mils)

APPENDIX D

WATER VELOCITY DISTRIBUTION

Figures D1 to D6 contain plots of water velocity along a blade to blade surface with increasing GVFs and bubble sizes at a pump speed of 3600 rpm.

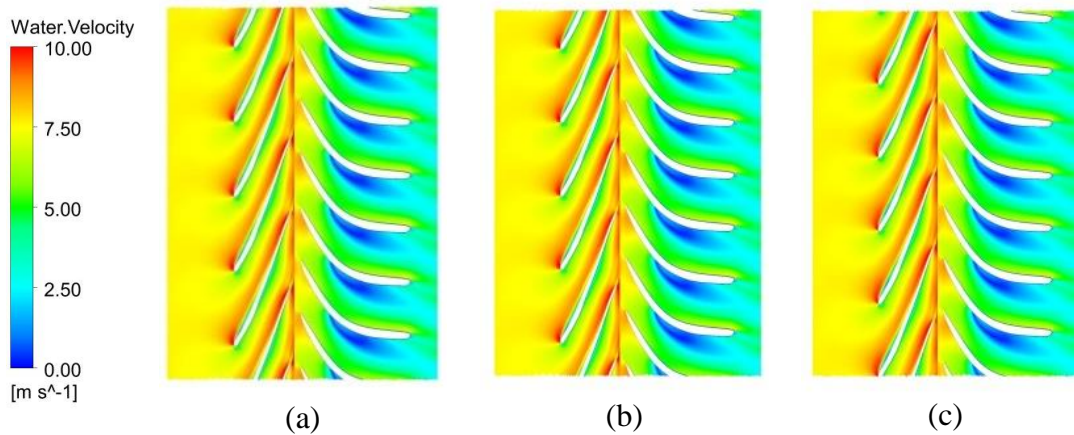


Figure D1 Water velocity along blade to blade surface for pump running at 3600 rpm with inlet GVF 13% and bubble sizes (a) $63.5 \mu\text{m}$ (2.5 mils) (b) $76.2 \mu\text{m}$ (3 mils) and (c) $101.6 \mu\text{m}$ (4 mils)

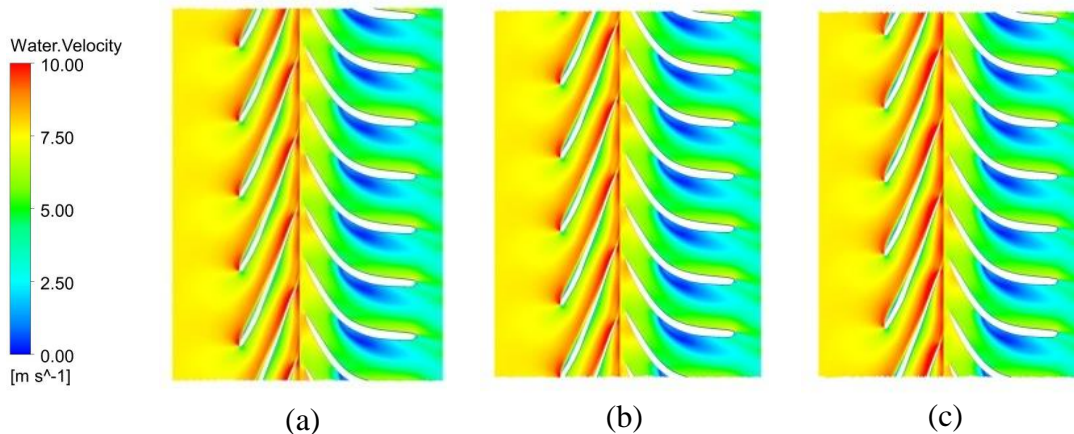


Figure D2 Water velocity along blade to blade surface for pump running at 3600 rpm with inlet GVF 19% and bubble sizes (a) $63.5 \mu\text{m}$ (2.5 mils) (b) $76.2 \mu\text{m}$ (3 mils) and (c) $101.6 \mu\text{m}$ (4 mils)

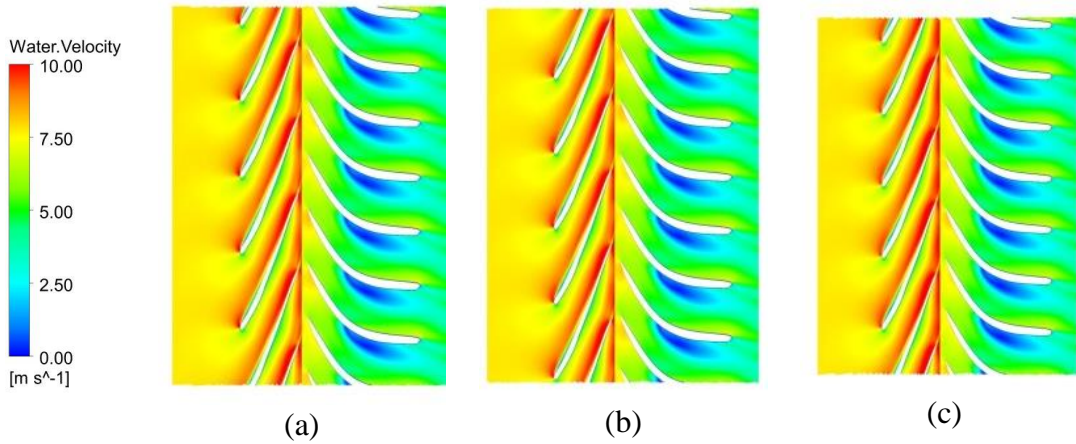


Figure D3 Water velocity along blade to blade surface for pump running at 3600 rpm with inlet GVF 24% and bubble sizes (a) 63.5 μm (2.5 mils) (b) 76.2 μm (3 mils) and (c) 101.6 μm (4 mils)

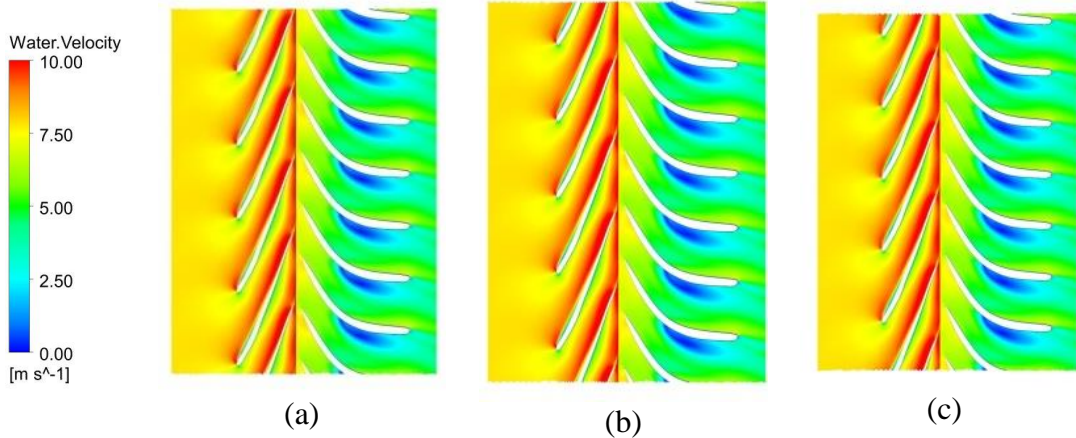


Figure D4 Water velocity along blade to blade surface for pump running at 3600 rpm with inlet GVF 29% and bubble sizes (a) 63.5 μm (2.5 mils) (b) 76.2 μm (3 mils) and (c) 101.6 μm (4 mils)

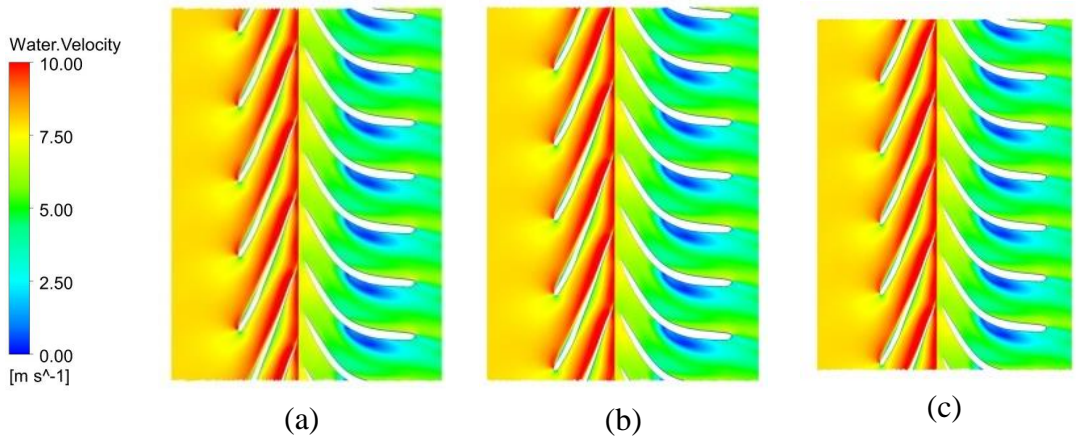


Figure D5 Water velocity along blade to blade surface for pump running at 3600 rpm with inlet GVF 35% and bubble sizes (a) 63.5 μm (2.5 mils) (b) 76.2 μm (3 mils) and (c) 101.6 μm (4 mils)

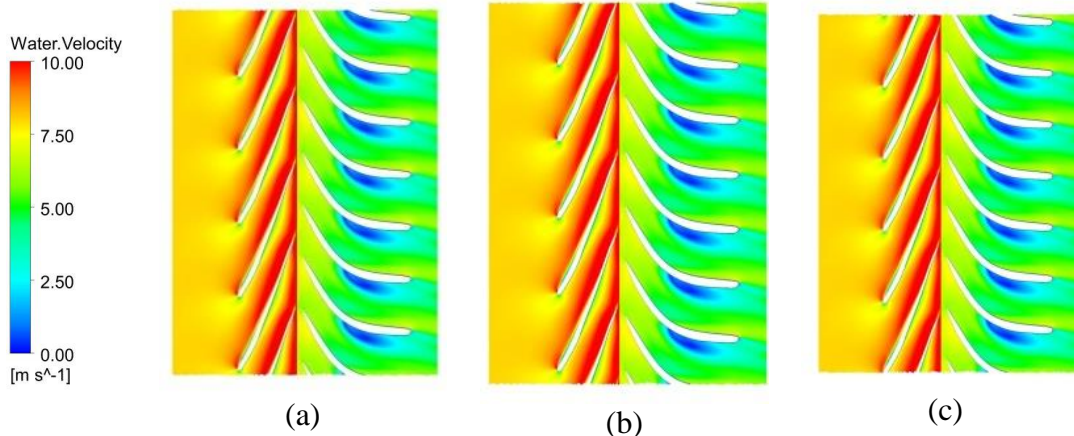


Figure D6 Water velocity along blade to blade surface for pump running at 3600 rpm with inlet GVF 40% and bubble sizes (a) 63.5 μm (2.5 mils) (b) 76.2 μm (3 mils) and (c) 101.6 μm (4 mils)

Figures D7 to D12 are plots of water velocity along a meridional surface for pump running at 3600 rpm with increasing GVFs and bubble sizes.

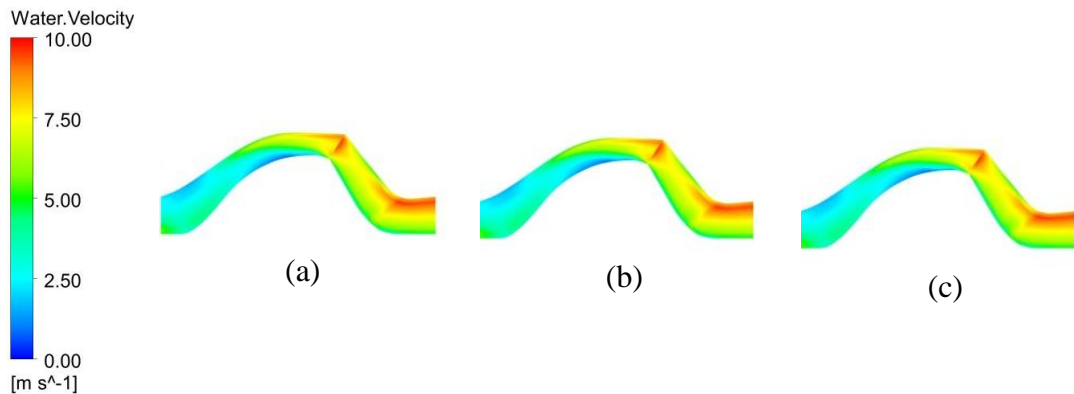


Figure D7 Water velocity along meridional surface for pump running at 3600 rpm with inlet GVF 13% and bubble sizes (a) 63.5 μm (2.5 mils) (b) 76.2 μm (3 mils) and (c) 101.6 μm (4 mils)

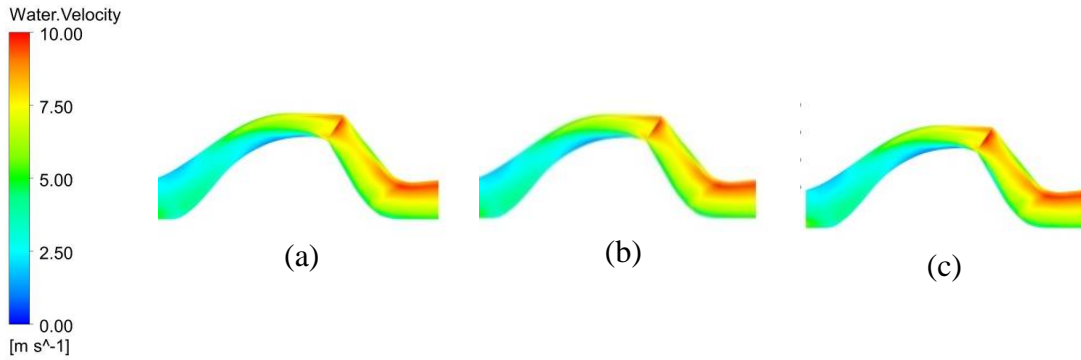


Figure D8 Water velocity along meridional surface for pump running at 3600 rpm with inlet GVF 19% and bubble sizes (a) 63.5 μm (2.5 mils) (b) 76.2 μm (3 mils) and (c) 101.6 μm (4 mils)

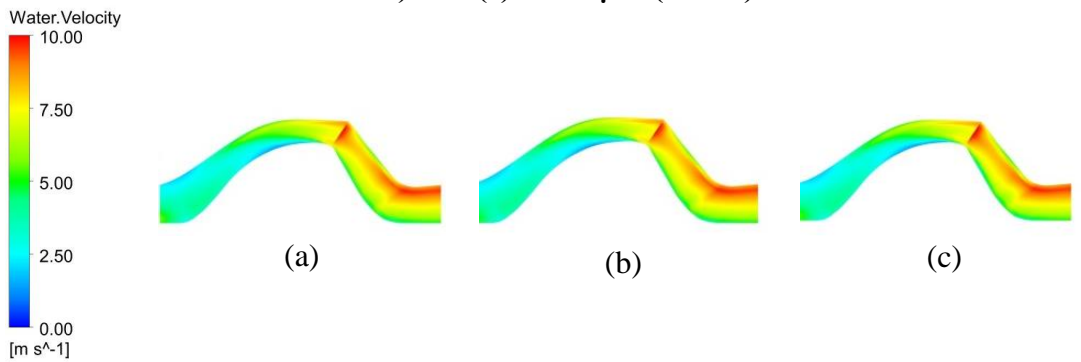


Figure D9 Water velocity along meridional surface for pump running at 3600 rpm with inlet GVF 24% and bubble sizes (a) 63.5 μm (2.5 mils) (b) 76.2 μm (3 mils) and (c) 101.6 μm (4 mils)

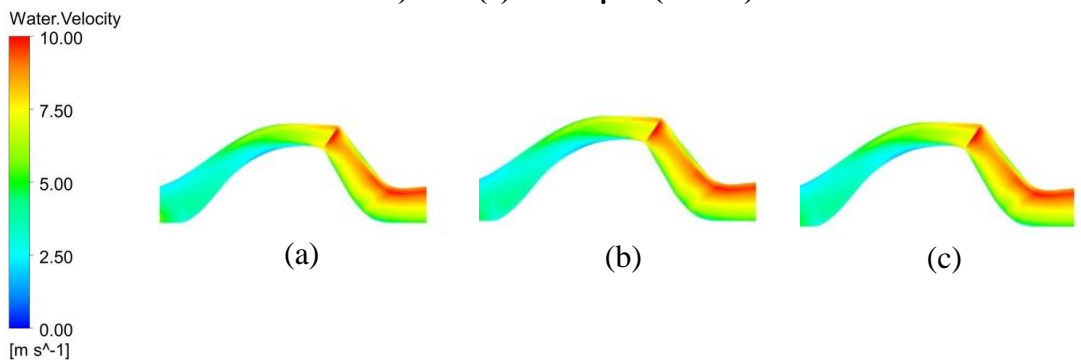


Figure D10 Water velocity along meridional surface for pump running at 3600 rpm with inlet GVF 29% and bubble sizes (a) 63.5 μm (2.5 mils) (b) 76.2 μm (3 mils) and (c) 101.6 μm (4 mils)

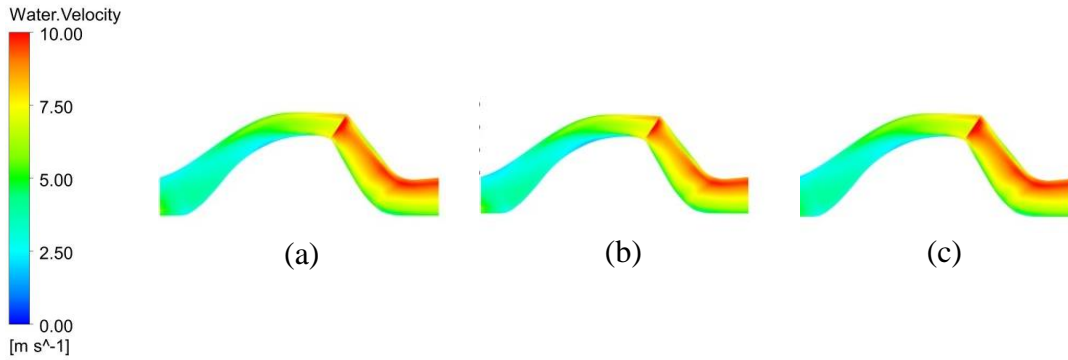


Figure D11 Water velocity along meridional surface for pump running at 3600 rpm with inlet GVF 35% and bubble sizes (a) 63.5 μm (2.5 mils) (b) 76.2 μm (3 mils) and (c) 101.6 μm (4 mils)

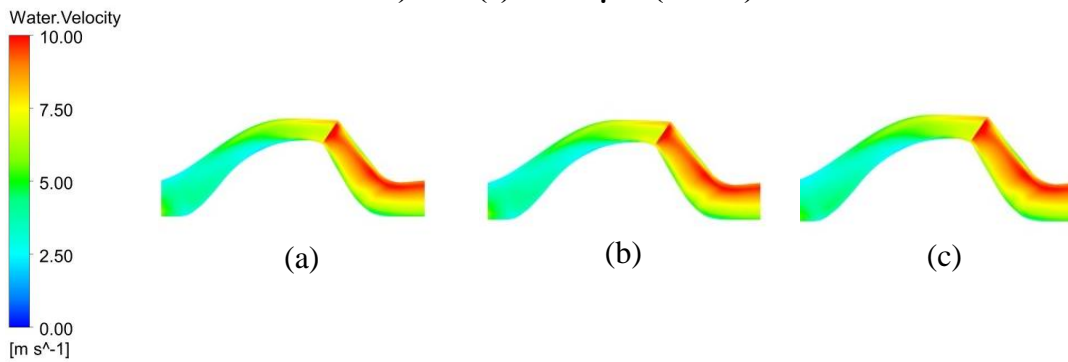


Figure D12 Water velocity along meridional surface for pump running at 3600 rpm with inlet GVF 40% and bubble sizes (a) 63.5 μm (2.5 mils) (b) 76.2 μm (3 mils) and (c) 101.6 μm (4 mils)

Figures D13 to D17 show the variation of water velocity along a blade to blade surface for pump speed 6000 rpm with increasing GVFs and bubble sizes.

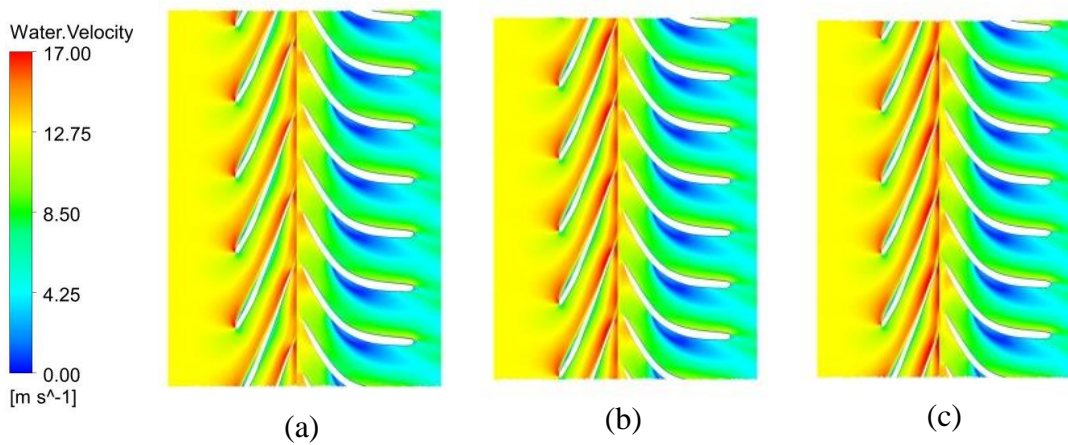


Figure D13 Water velocity along blade to blade surface for pump running at 6000 rpm with inlet GVF 13% and bubble sizes (a) 63.5 μm (2.5 mils) (b) 76.2 μm (3 mils) and (c) 101.6 μm (4 mils)

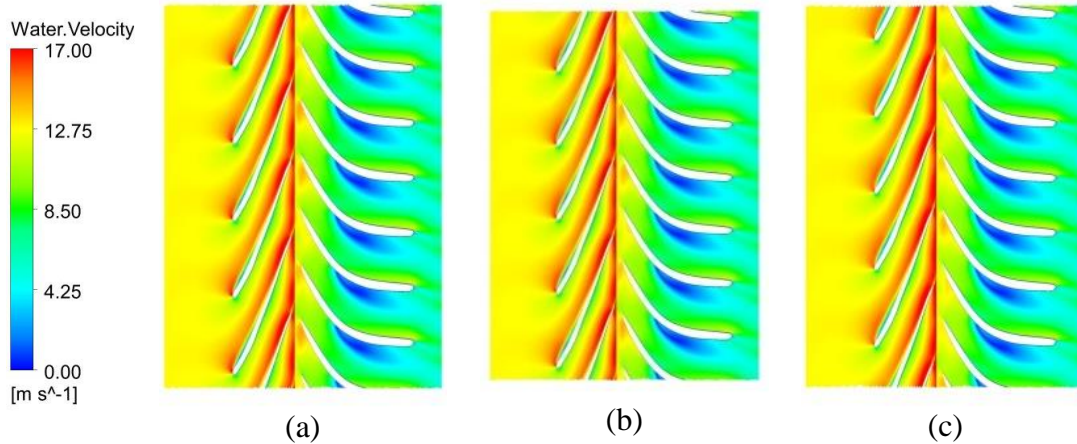


Figure D14 Water velocity along blade to blade surface for pump running at 6000 rpm with inlet GVF 18% and bubble sizes (a) 63.5 μm (2.5 mils) (b) 76.2 μm (3 mils) and (c) 101.6 μm (4 mils)

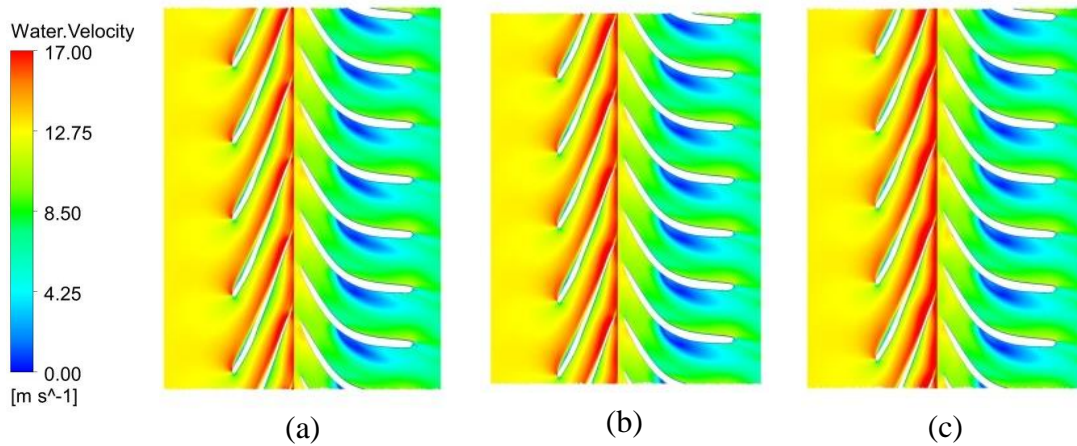


Figure D15 Water velocity along blade to blade surface for pump running at 6000 rpm with inlet GVF 25% and bubble sizes (a) 63.5 μm (2.5 mils) (b) 76.2 μm (3 mils) and (c) 101.6 μm (4 mils)

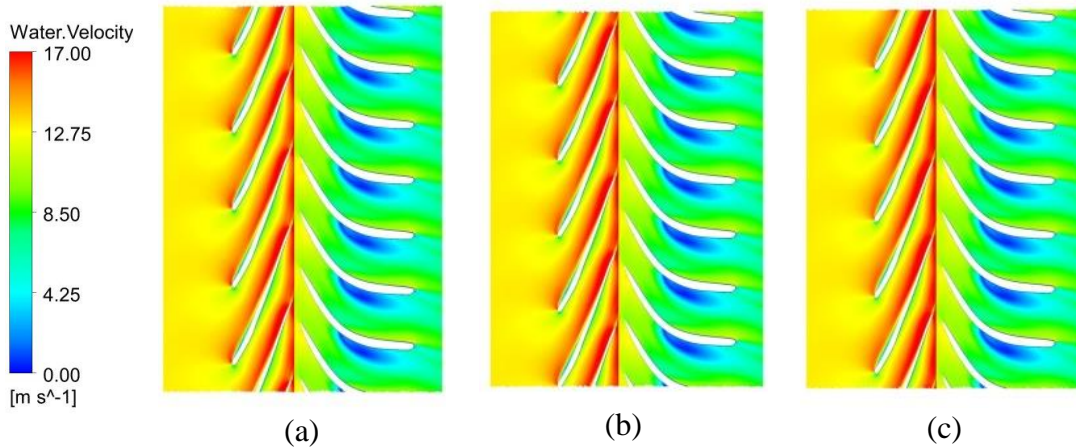


Figure D16 Water velocity along blade to blade surface for pump running at 6000 rpm with inlet GVF 30% and bubble sizes (a) 63.5 μm (2.5 mils) (b) 76.2 μm (3 mils) and (c) 101.6 μm (4 mils)

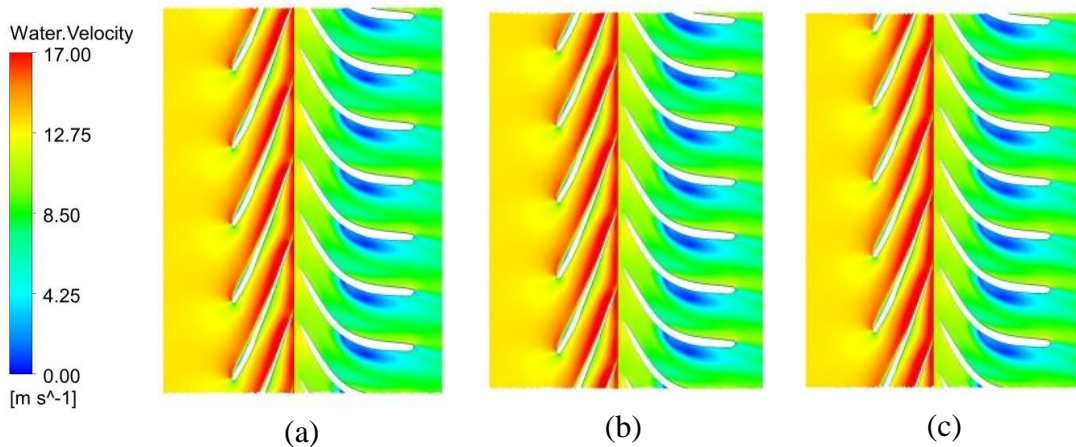


Figure D17 Water velocity along blade to blade surface for pump running at 6000 rpm with inlet GVF 35% and bubble sizes (a) 63.5 μm (2.5 mils) (b) 76.2 μm (3 mils) and (c) 101.6 μm (4 mils)

Figures D18 to D22 are plots of water velocity along a meridional plane for pump speed 6000 rpm with increasing GVFs and bubble sizes.

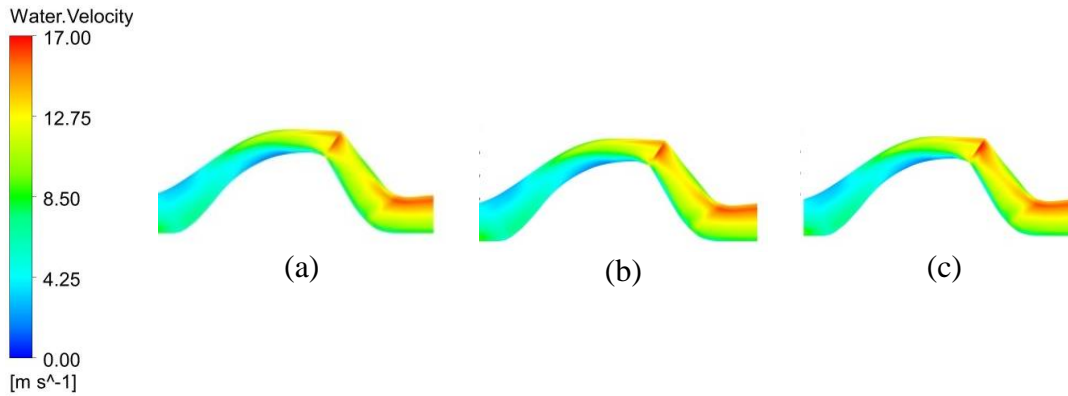


Figure D18 Water velocity along meridional surface for pump running at 6000 rpm with inlet GVF 13% and bubble sizes (a) $63.5 \mu\text{m}$ (2.5 mils) (b) $76.2 \mu\text{m}$ (3 mils) and (c) $101.6 \mu\text{m}$ (4 mils)

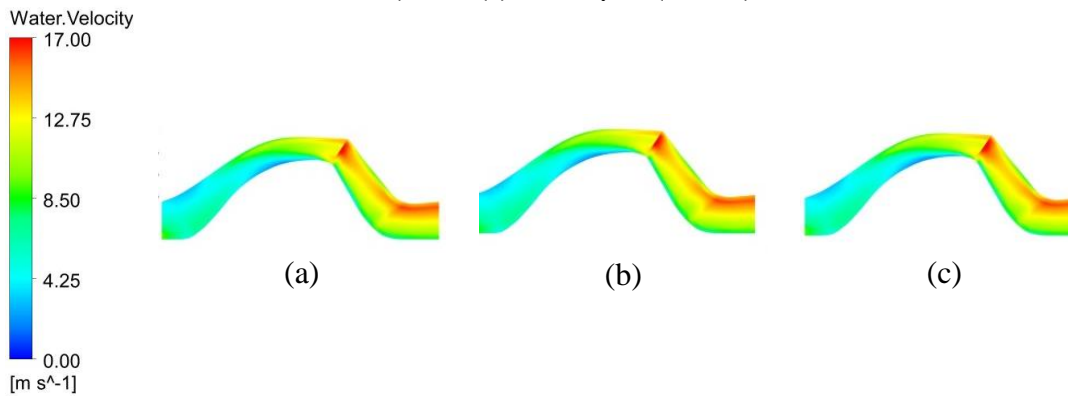


Figure D19 Water velocity along meridional surface for pump running at 6000 rpm with inlet GVF 18% and bubble sizes (a) $63.5 \mu\text{m}$ (2.5 mils) (b) $76.2 \mu\text{m}$ (3 mils) and (c) $101.6 \mu\text{m}$ (4 mils)

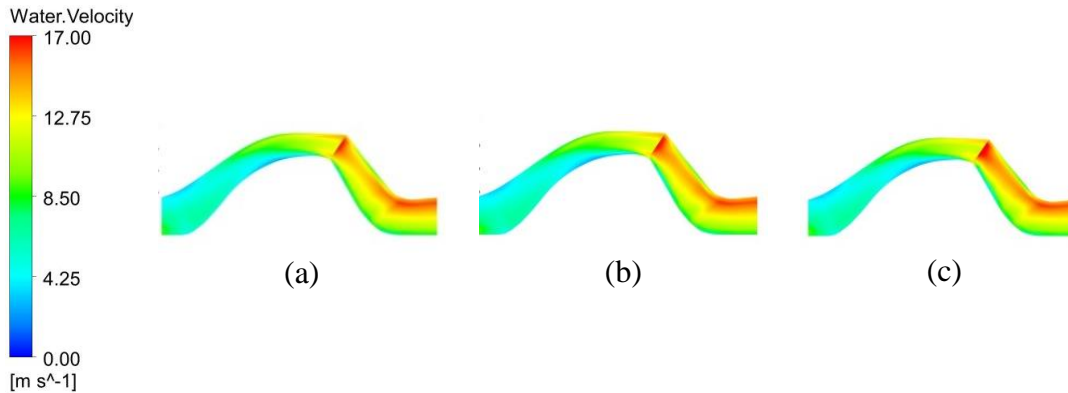


Figure D20 Water velocity along meridional surface for pump running at 6000 rpm with inlet GVF 25% and bubble sizes (a) $63.5 \mu\text{m}$ (2.5 mils) (b) $76.2 \mu\text{m}$ (3 mils) and (c) $101.6 \mu\text{m}$ (4 mils)

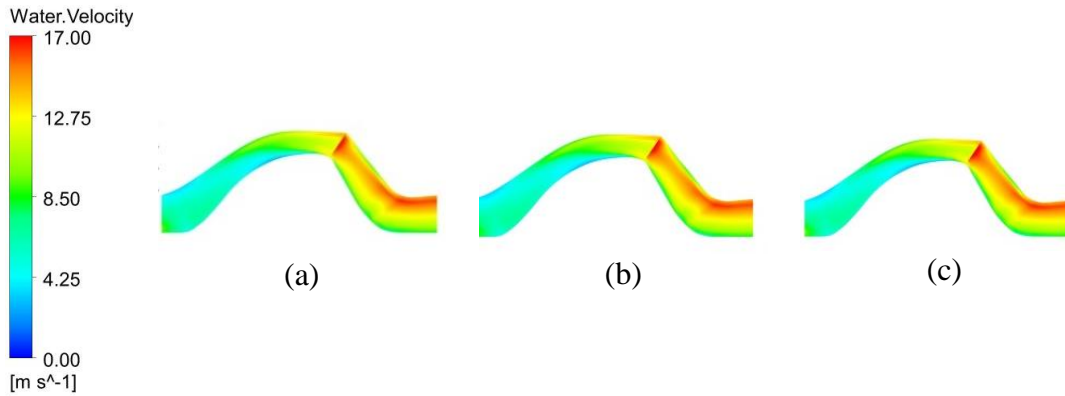


Figure D21 Water velocity along meridional surface for pump running at 6000 rpm with inlet GVF 30% and bubble sizes (a) $63.5 \mu\text{m}$ (2.5 mils) (b) $76.2 \mu\text{m}$ (3 mils) and (c) $101.6 \mu\text{m}$ (4 mils)

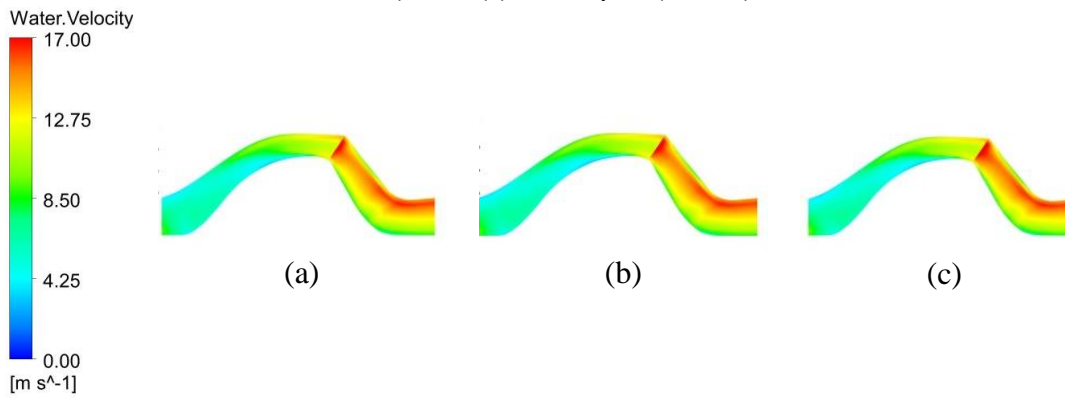


Figure D22 Water velocity along meridional surface for pump running at 6000 rpm with inlet GVF 35% and bubble sizes (a) $63.5 \mu\text{m}$ (2.5 mils) (b) $76.2 \mu\text{m}$ (3 mils) and (c) $101.6 \mu\text{m}$ (4 mils)